



UCTEA Turkish Chamber of Civil Engineers
TMMOB İnşaat Mühendisleri Odası

Turkish Journal of Civil Engineering

formerly
Teknik Dergi

Volume 35
Issue 5
September 2024



Turkish Journal of Civil Engineering (formerly Teknik Dergi) Publication Principles

Turkish Journal of Civil Engineering (TJCE), a non-profit, open access scientific and technical periodical of UCTEA Chamber of Civil Engineers, publishes papers reporting original research work and major projects of interest in the area of civil engineering. TJCE annually publishes six issues and is open to papers in English and Turkish. It should be noted that TJCE (formerly, Teknik Dergi/ Technical Journal of Turkish Chamber of Civil Engineers) is being published regularly for more than 30 years since 1990. Main publication principles of TJCE are summarized below:

1. Articles reporting original scientific research and those reflecting interesting engineering applications are accepted for publication. To be classified as original, the work should either produce new scientific knowledge or add a genuinely new dimension to the existing knowledge or develop a totally new method or substantially improve an existing method.
2. Articles reporting preliminary results of scientific studies and those which do not qualify as full articles but provide useful information for the reader can be considered for publication as technical notes.
3. Discussions received from the readers of the published articles within three months from publication are reviewed by the Editorial Board and then published together with the closing remarks of the author.
4. Manuscripts submitted for publication are evaluated by two or three reviewers unknown to the authors. In the light of their reports, final decision to accept or decline is taken by the Editorial Board. General policy of the Board is to get the insufficient manuscripts improved in line with the reviewers' proposals. Articles that fail to reach the desired level are declined. Reasons behind decisions are not declared.
5. A signed statement is taken from the authors, declaring that the article has not been published as a "journal article or book chapter". In case the Editorial Board is in the opinion that the article has already been published elsewhere with minor changes or suspects plagiarism or a similar violation of ethics, then not only that article, but none of the articles of the same authors are published.
6. Papers reporting works presented as conference papers and developed further may be considered for publication. The conference it was presented to is given as a footnote in the first page.
7. Additionally, a document signed by all authors, transferring the copyright to UCTEA Chamber of Civil Engineers is submitted together with the manuscript.



UCTEA Turkish Chamber of Civil Engineers
TMMOB İnşaat Mühendisleri Odası

Turkish Journal of Civil Engineering

formerly
Teknik Dergi

Volume 35
Issue 5
September 2024



UCTEA Turkish Chamber of Civil Engineers
TMMOB İnşaat Mühendisleri Odası

Necatibey St. No: 57, Kızılay 06440 Ankara, Turkey

Tel: +90.312.294 30 00 - Faks: +90.312.294 30 88

E-mail: imo@imo.org.tr - www.imo.org.tr

Publisher (Sahibi):

Nusret SUNA

On behalf of UCTEA Turkish Chamber of Civil Engineers

Administrative Officer (Yazı İşleri Müdürü):

Bülent TATLI

Volume 35 - Issue 5 - September 2024 (*Cilt 35 - Sayı 5 - Eylül 2024*)

Published bi-monthly. Local periodical. (*İki ayda bir yayınlanır, yerel süreli yayın*)

Date of Print: September 1, 2024 (*Baskı Tarihi: 1 Eylül 2024*)

Number of copies: 800 (*800 adet basılmıştır*)

Quotations require written approval of the Editorial Board.

(*Yayın Kurulunun yazılı onayı olmaksızın alıntı yapılamaz.*)

ISSN: 2822-6836

Turkish Journal of Civil Engineering (formerly Teknik Dergi) is indexed by

- Science Citation Index Expanded
- Scopus
- Journal Citation Reports / Science Edition
- Engineering Index
- Concrete Abstracts (American Concrete Institute)
- National Technical Information Service (US NTIS)
- CITIS
- Ulrich's International Periodical's Directory
- Google Scholar
- TR Index

Turkish Journal of Civil Engineering (formerly Teknik Dergi) is a peer reviewed open access periodical publishing papers of original research and interesting practice cases. It addresses both the research community and the practicing engineers.

Printed by (Baskı):

Ankamat Matbaacılık San.

İvedik OSB. 1344. Sok. Yenimahalle / Ankara - Tel: 0.312.394 54 64

Sertifika No: 46700

Turkish Journal of Civil Engineering (formerly Teknik Dergi)

Editor-in-Chief:

Alper İLKİ

Editors:

İsmail AYDIN

Özer ÇİNİCİOĞLU

Metin GER

Gürkan Emre GÜRCANLI

Kutay ORAKÇAL

İsmail ŞAHİN

Özkan ŞENGÜL

Tuğrul TANKUT

Kağan TUNCAY

Ufuk YAZGAN

Emine Beyhan YEĞEN

Drafting Language Check:

İsmail AYDIN

Özer ÇİNİCİOĞLU

Metin GER

Polat GÜLKAN

Gürkan Emre GÜRCANLI

İsmail ŞAHİN

Özkan ŞENGÜL

Mehmet UTKU

Emine Beyhan YEĞEN

Editorial Assistant:

Çağlar GÖKSU AKKAYA

Secretary:

Cemal ÇİMEN

Advisory Board:

Prof. M. Aral, USA

Prof. D. Arditi, USA

Prof. A. Aydilek, USA

Prof. K. Beyer, Switzerland

Prof. N. Çatbaş, USA

Prof. M. Çetin, USA

Prof. M. Dewoolkar, USA

Prof. T. Edil, USA

Prof. K. Elwood, New Zealand

Prof. M. Fardis, Greece

Prof. G. Gazetas, Greece

Prof. P. Gülkan, Türkiye

Prof. J. Han, USA

Prof. I. Hansen, Netherlands

Prof. T. Hartmann, Germany

Prof. F. Imamura, Japan

Prof. T. Kang, Korea

Prof. K. Kusunoki, Japan

Prof. S. Lacasse, Norway

Prof. R. Al-Mahaidi, Australia

Prof. K. Özbay, USA

Prof. H. Özer, USA

Prof. S. Pampanin, Italy

Prof. A. J. Puppala, USA

Prof. M. Saatçioğlu, Canada

Prof. C. Santamarina, Saudi Arabia

Prof. S. Sheikh, Canada

Prof. E. C. Shin, South Korea

Prof. J. Smallwood, South Africa

Prof. M. Sümer, Türkiye

Dr. H. A. Şentürk, Türkiye

Dr. S. S. Torisu, Japan

Prof. E. Tutumluer, USA

Prof. M. Tümay, USA

Reviewers:

This list is renewed each year and includes reviewers who served in the last two years of publication.

Şükran AÇIKEL	Ali Fırat ÇABALAR	Saadet Gökçe GÖK	Özgür KURÇ	Haluk SUCUOĞLU
Kamil Bekir AFACAN	Barlas Özden	Tansu GÖKÇE	Hasan KURTARAN	Erol ŞADOĞLU
Bülent AKBAŞ	ÇAĞLAYAN	Serdar GÖKTEPE	Murat KURUOĞLU	Yuşa ŞAHİN
Sami Oğuzhan AKBAŞ	Ferit ÇAKIR	Semih GÖNEN	Akif KUTLU	Zekai ŞEN
Zühal AKBAY ARAMA	Melih ÇALAMAK	Rahmi GÜÇLÜ	Merih KÜÇÜKLER	Burak SENGÖZ
Rıfat AKBİYİKLİ	Gülben ÇALIŞ	Ali GÜL	Abdullah KÜRKCÜ	Gülüm TANIRCAN
Sarven AKCELYAN	Umut ÇALIŞKAN	Fazlı Erol GÜLER	Todd LİTMAN	Serhan TANYEL
Burcu AKÇAY	Süheyla Pelin	İlgin GÜLER	Fağih MAARİF	Mucip TAPAN
ALDANMAZ	ÇALIŞKANELLİ	M. Fethi GÜLLÜ	Müslüm Murat MARAŞ	Ergin TARI
Cihan Taylan AKDAĞ	Mehmet Alper ÇANKAYA	Adil GÜLTEKİN	Halit Cenani MERTOL	Yüksel TAŞDEMİR
Bekir AKGÖZ	Serdar ÇARBAŞ	Fırat GÜMGÜM	Mahmoud MIARI	Ali Şahin TAŞLIGEDİK
Cem AKGÜNER	Dilay ÇELEBİ	Gürkan GÜNAY	Mehmet Murat MONKUL	Hasan TATLI
Fevziye AKÖZ	Tevfik Kutay	Taylan GÜNAY	Nihat MOROVA	Gökmen TAYFUR
Erkan AKPINAR	ÇELEBİOĞLU	Murat GÜNAYDIN	Yetiş Şazi MURAT	Serdal TERZİ
Muhammet Vefa	Ahmet Ozan ÇELİK	Samet GÜNER	Sepanta NAİMİ	Berrak TEYMUR
AKPINAR	Oğuz Cem ÇELİK	Burcu GÜNEŞ	Salih OFLUOĞLU	Hüseyin Onur TEZCAN
Atakan AKSOY	Ozan Cem ÇELİK	Oğuz GÜNEŞ	Fuad OKAY	Mesut TİGDEMİR
Hafzullah AKSOY	Hilmi Berk ÇELİKOĞLU	Mehmet Şükri GÜNEY	Didem OKTAY	Salih TİLEYLİOĞLU
Tülay AKSU ÖZKUL	Kemal Önder ÇETİN	Tuba GÜRBÜZ	Derviş Volkan OKUR	Onur Behzat TOKDEMİR
Uğurhan AKYÜZ	Mecit ÇETİN	BÜYÜKKAYIKÇI	Sezan ORAK	Nabi Kartal TOKER
Alper ALDEMİR	Elif ÇİÇEK	Aslı Pelin GÜRGÜN	Engin ORAKDÖĞEN	Ali TOPAL
Cenk ALHAN	Emin ÇİFTÇİ	Tefarruk HAKTANIR	Şeref ORUÇ	Cem TOPKAYA
Gülşay ALTAY	Hüseyin ÇİLSALAR	Soner HALDENBİLEN	Okan ÖNAL	Kamil TOSUN
Sinan ALTIN	Erdal ÇOKÇA	Murat HAMDERİ	Akin ÖNALP	FELEKOĞLU
Adlen ALTUNBAŞ	Semra ÇOMU	Ingo A. HANSEN	Bihra ÖNÖZ	Gökçe TÖNÜK
Yalçın ALVER	Turgay ÇOŞGUN	Umut HASGÜL	Cihan ÖSER	Erkan TÖRE
Mustafa M. ARAL	Atilla DAMCI	Emre HASPOLAT	Yiğit ÖZÇELİK	Kemal Dirgen TÖZER
Davut ARDITI	Yakup DARAMA	Mustafa HATİPOĞLU	Gökhan ÖZDEMİR	Nursu TUNALIOĞLU
Yalın ARICI	Kutlu DARILMAZ	Lucas HOGAN	Zuhal ÖZDEMİR	Gürsoy TURAN
Deniz ARTAN İLTER	Tayfun DEDE	Zeynep İŞİK	Murat ÖZEN	Hasan Nuri
Deepankar Kumar	Cem DEMİR	Sabriye Banu İKİZLER	Pelin ÖZENER	TÜRKMEÑOĞLU
ASHISH	Selçuk DEMİR	Okan İLHAN	Ekin ÖZER	Cüneyt TÜZÜN
Ayşegül ASKAN	Uğur DEMİR	Erol İSKENDER	Hasan ÖZER	Eren UÇKAN
GÜNDOĞAN	Ender DEMİREL	Medine İSPİR ARSLAN	Hakkı Oral ÖZHAN	Latif Onur UĞUR
Ali Osman ATAHAN	Mehmet Cüneyd	Recep İYİŞAN	Mehmet Fatih ÖZKAL	Mehmet Baran ULAK
Hakan Nuri ATAHAN	DEMİREL	Nuray Işık KABDAŞLI	Zeynep Huri ÖZKUL	Dilay UNCÜ
Güzide ATASOY ÖZCAN	Murat DİCLELİ	Volkan KALPAKÇI	BİRGÖREN	Berna UNUTMAZ
Ali Osman ATEŞ	Seyyit Ümit DİKMEN	Muhammet KAMAL	Aşkın ÖZOCAK	Mehmet UTKU
Özgür AVŞAR	Ahmet Anıl DINDAR	Reza KAMGAR	Sadık ÖZTOPRAK	Volkan Emre UZ
Cem AYDEMİR	Mustafa DOĞAN	Hakan Alper	Turan ÖZTURAN	İbrahim Mert UZUN
Metin AYDOĞDU	Marco DOMANESCHİ	KAMİLOĞLU	Gözde Başak ÖZTÜRK	Deniz ÜLGEN
Ülker Güner BACANLI	Gökhan DÖK	Elif Çağda KANDEMİR	Mustafa ÖZUYSAK	Mehmet Barış Can
Selim BARADAN	Cemalettin DÖNMEZ	Tanay KARADEMİR	Tolga Yılmaz	ÜLKER
Eray BARAN	İsmail DURANYILDIZ	Hüseyin Faruk	ÖZÜDOĞRU	Yurdanur ÜNAL
Özgür Uğraş BARAN	Cengiz DÜNDAR	KARADOĞAN	Atilla ÖZÜTOK	Ali ÜNAY
Türkey BARAN	Nurhan ECEMİŞ ZEREN	Ümit KARADOĞAN	Nilüfer ÖZYURT	Cüneyt VATANSEVER
Efe BARBAROS	Özgür EKİNCİOĞLU	Mustafa Erkan	ZİHNİOĞLU	Ahmet YAKUT
Bekir Oğuz BARTIN	Serkan ENGİN	KARAGÜLER	Erhan Burak PANCAR	Erkut YALÇIN
Zeynep BAŞARAN	Murat Altuğ ERBERİK	Halil KARAHAAN	Seval PINARBAŞI	Aslı YALÇIN
BUNDUR	Ali ERCAN	Oğuz KAYABAŞI	ÇUHADAROĞLU	Mustafa Sinan YARDIM
Mustafa Gökçe	Barış ERDİL	İlker KAZAZ	Elişan Filiz PİROĞLU	Anıl YAZICI
BAYDOĞAN	Sinan Turhan ERDOĞAN	Saeid KAZENZADEH	Bora POLATSU	Shehata E. Abdel
Cüneyt BAYKAL	Şakir ERDOĞDU	AZAD	RAHEEM	Gökhan YAZICI
Mehmet BERİLGEN	Esin ERGEN PEHLEVAN	Mustafa Kubilay	KELEŞOĞLU	Halit YAZICI
Katrin BEYER	Yusuf Çağatay ERŞAN	Elçin KENTEL	Selçuk SAATÇI	Cem YENİDOĞAN
Niyazi Özgür BEZGİN	Kağan ERYÜRÜK	Hadi	Selman SAĞLAM	Mehmet YETMEZ
Ozan BİLAL	Esra Ece ESELLER	KHANBAZADEH	Mehmet SALTAN	İrem Zeynep YILDIRIM
Senem BİLİR	BAYAT	Ufuk KIRBAŞ	Altuğ SAYGILI	Berivan YILMAZER
MAHÇİÇEK	Tuğba ESKİŞAR TEFÇİ	Serdar SELAMET	Nuri SERTESER	POLAT
İlknur BOZBEY	Burak FELEKOĞLU	Veyssel Şadan Özgür	KIRCA	Ercan YÜKSEL
Ali BOZER	Mahmut FIRAT	Mehmet Amil	KIZILASLAN	Yeliz YÜKSELEN
Mehmet Bakır BOZKURT	Onur GEDİK	Esat Selim KOCAMAN	Salih KOÇAK	AKSOY
Zafer BOZKUŞ	Abdullah GEDİKLİ	Mete KÖKEN	Baha Vural KÖK	Ahmet Şahin ZAİMOĞLU
Zekai CELEP	Ergun GEDİZLİOĞLU		Serdar SOYÖZ	Abdullah Can ZÜLFİKAR
Cihan CENGİZ	Ahmet Talha GEZGİN		Rifat SÖNMEZ	
Halim CEYLAN	Sadık Can GİRGIN		Tayfun Altuğ SÖYLEV	
Joao Ramoa CORREIA	Zehra Canan GİRGIN			

Turkish Journal of Civil Engineering (formerly Teknik Dergi)

Volume 35 Issue 5 September 2024

CONTENTS

RESEARCH ARTICLE

Rainwater Harvesting System Analysis for Semi-Arid Climate: A Daily Linear Programming Model 1
Mustafa RUSO, Bertuğ AKINTUĞ, Elcin KENTEL

Spatial Prediction of Groundwater Potential of Upper Tigris Basin Mapping in Türkiye with GIS-Based Multicriteria Decision Making (MCDM) Method..... 29
Recep ÇELİK

Design and Tests of Structural Post-Tensioned Glass T-Beams..... 51
Emrullah KOCA, Ahmet TÜNER

6 Şubat 2023 Depremleri ve Saha Gözlemlerine Dayalı Bina Hasarları Hakkında Ön Değerlendirme..... 75
Cem YENİDOĞAN

A Receding Contact Problem of Two Layers one of Functionally Graded, Loaded by Circular Rigid Block and Resting on a Pasternak Foundation..... 115
Aleyna YAZICIOĞLU, Ahmet BİRİNCİ, Gökhan ADIYAMAN

TECHNICAL NOTE

Flexural Experiments on B58 Type Railway Sleepers with Different Dosages of Steel Fibers..... 133
Ercan KASAPOĞLU, Tefaruk HAKTANIR

Rainwater Harvesting System Analysis for Semi-Arid Climate: A Daily Linear Programming Model

Mustafa RUSO¹
Bertuğ AKINTUĞ^{2*}
Elcin KENTEL³



ABSTRACT

Rainwater harvesting has proven to be an alternative water supply scheme for sustainable water management of regions with limited water resources. In this paper, a linear programming (LP) model with daily time steps, which minimizes a rooftop rainwater harvesting system (RWHS) cost, is developed and used to calculate the optimum RWH tank size. The developed LP model is applied to the semi-arid Northern Cyprus in the Eastern Mediterranean. The analysis is carried out for 33 sites which receive average annual rainfall ranging from 292 mm to 548 mm to evaluate the spatial effect of rainfall characteristic and the water cost on the financial feasibility and performance of the RWHS. At 29 out of 33 sites, RWHS investments are found to be financially feasible with discounted payback periods ranging from 12 to 28 years. The optimum RWH tank sizes are determined to be between 2 m³ and 6 m³ resulting in up to 20 % reliability with more than 50 m³ of average annual water savings per house. It is observed that the cost of water is a critical factor that affects the financial feasibility and water savings of a RWHS, especially in regions with limited rainfall. The comparison of the developed daily LP model with an LP model with monthly time steps demonstrates that the financial feasibility and the optimum tank size can only be assessed realistically when daily time steps are used. Finally, the sensitivity analysis shows that the discounted payback period is highly sensitive to the collector area.

Keywords: Sustainable water use, rainwater harvesting, optimum tank size, spatial analysis, semi-arid climate, Northern Cyprus.

Note:

- This paper was received on July 14, 2023 and accepted for publication by the Editorial Board on April 5, 2024.
- Discussions on this paper will be accepted by November 30, 2024.
- <https://doi.org/10.18400/tjce.1326198>

1 Middle East Technical University, Northern Cyprus Campus, Sustainable Environment and Energy Systems Graduate Program, Turkish Republic of Northern Cyprus
mustafaruso.metu@gmail.com - <https://orcid.org/0000-0002-7694-3131>

2 Middle East Technical University, Northern Cyprus Campus, Civil Engineering Program, Turkish Republic of Northern Cyprus
bertug@metu.edu.tr - <https://orcid.org/0000-0001-6206-4315>

3 Middle East Technical University, Department of Civil Engineering, Ankara, Türkiye
ekentel@metu.edu.tr - <https://orcid.org/0000-0002-7477-0345>

* Corresponding author

1. INTRODUCTION

Water, intertwined with sustainable development, is vital to the continuity of healthy life and ecosystems [1]. However, water resources are finite and need to be sustainably managed. Rainwater harvesting is an old and sustainable water resources management technique employed to collect and use rainwater to improve the accessibility of water where it is scarce. Systems that harvest, store, and bring rainwater into the service are called rainwater harvesting systems (RWHSs). Harvested rainwater is stored in a tank or a cistern. Some of the water demand can be supplied using RWHSs, especially at water-stressed islands [2-8]. Moreover, RWH is expected to reduce damages related to urban floods [9], can mitigate the effects of urbanization and climate change on water resources and is necessary for sustainable urban water management [10].

Tank size is one of the main concerns in designing RWHSs since it directly affects the financial feasibility of the system and performance indicators such as reliability, resilience, and vulnerability [11-15]. Generally, approaches based on a water balance model are used to identify the best tank size. A set of alternative tank sizes are selected and the water balance model is executed for each alternative tank size to evaluate the corresponding financial feasibility [16-24] and the performance of the systems [25-29]. However, in the analysis of a high number of sites, water balance models are time-consuming since they require solving the model once for each tank size in a trial and error approach. On the other hand, when linear programming (LP) models are used the whole domain is searched and the optimum tank size is identified in a single run.

Mixed-integer, linear and non-linear optimization models have recently been used for optimal RWHS design. Bocanegra-Martínez et al. [30] and [31] developed multi-objective non-linear optimization models to design water supply networks in a residential complex for reusing reclaimed water and harvested rainwater. Their models aimed to minimize total cost and freshwater consumption. Sample, D. J., & Liu, J. [32] investigated minimizing costs of RWHSs for supplying water and capturing runoff. Emami Javanmard et al. [33] developed a multi-objective mixed-integer LP model to optimize energy and water use of dwellings and to decrease CO₂ emissions. Their results showed that the amount of water provided from the local water grid was reduced at least 20% through RWH and greywater recycling. Zhang, L. et al. [34] proposed a mixed-integer LP model to optimize water tank size and operation of pumps for the minimum potable water consumption and electricity cost. Their results indicated that electricity price, discount rate, rainfall intensity, and water demand all impact the size of the water tank but only water demand has a significant impact on the cost-effectiveness of the system. LP models are simpler in comparison with other optimization models and guarantees to find the optimum tank size if there exists one. To the best of the authors' knowledge, work of Okoye, C. O. et al. [35] is the first study in which LP is used to identify the optimum tank size. Then, Ruso, M. et al. [36] identified optimum tank sizes by minimizing total costs using the LP approach with monthly time steps. Both studies concluded that utilization of monthly time steps affects the optimum tank size and the financial benefit of the system considerably. Furthermore, in studies where the effect of hourly, daily and yearly time steps are compared, the use of smaller time steps is recommended to evaluate the performance more accurately [37-41]. Large time steps (e.g. monthly) caused oversized tank designs and misleading reliability evaluations [39]. Zhang, S. et al. [41] showed that monthly time steps ended in inaccurate results, while hourly and

daily time steps resulted in similar performances and water savings. Thus, in this study, the LP model in [36] is modified to run with daily time steps (LP-Daily Model) and inflation rates are used to estimate future costs for a more realistic cost-benefit analysis.

A spatial performance assessment of RWHSs was conducted in various studies [25, 42- 47] and dependence of the performance on the climatic characteristics of the site were highlighted. [25] investigated the potable water savings potential of the residential areas in 62 cities in Brazil. Equations were developed to correlate the potential for water savings with rainfall and water demand. Potable water savings ranged from 34% to 92% for the 62 cities. Campisano, A., & Modica, C. [42] introduced a dimensionless methodology to determine the optimum tank size for 17 rainfall gauging stations on the island of Sicily, Italy. Water saving and overflow discharges were evaluated using simulation results of the daily time step water balance model. The optimum tank size was selected based on cost efficiency. It was reported that the net revenue decreases when tank size increases and rainfall decreases. Ali, S., et al. [47] developed a daily water balance model and applied it to five climatic regions of Pakistan. Water saving, stormwater capture efficiency and financial feasibility of RWHSs were assessed for different tank sizes up to 100 m³. They founded financially feasible systems could be achieved in a warm, semi-arid climate with 667 mm of average annual rainfall, while RWHS investments were found to be financially infeasible in a cold, semi-arid climate with 238 mm of average annual rainfall. Preeti, P., & Rahman, A. [48] investigated the reliability of RWHSs for eight cities in Australia with average annual rainwater ranging from 510 mm to 1176 mm using a daily water balance modelling approach. Reliability was found to range from 88% to 99% for toilet and laundry uses for tank sizes ranging from 10 m³ to 100 m³. They concluded that RWHS investments were not economically viable in most of the investigated cities.

This study aims (i) to introduce a single-objective *LP model with daily time steps* to optimize tank sizes by minimizing costs and (ii) to investigate the *spatial effect of rainfall characteristics and water costs* on the financial feasibility and performance of RWHSs. The developed LP-Daily Model determines optimum RWH tank sizes for 33 case study sites selected from the semi-arid Northern Cyprus, located in the Eastern Mediterranean Sea.

2. METHOD

In this study, a single-objective *LP model with daily time steps* is developed to identify the best RWH tank size by minimizing municipal water, wastewater, and tank costs. Optimum supply strategy of daily water demand of a single residential unit is determined using historical daily rainfall data. Musayev, S. et al. [46] showed that climate change will have a negligible impact on the feasibility of RWHSs in semi-arid regions. Thus, it is assumed that the rainfall pattern in the near future will be similar to that of the simulation period and the optimum RWH tank size will be efficient in the near future as well.

2.1. LP-Daily Model

The developed LP-Daily model uses the yield-before-spillage algorithm. First, the daily water demand is supplied, and then the current day's rainfall is harvested. The excess rainwater is spilled if the capacity of the tank is exceeded. Our model allows the use of water from the RWH tank or the municipal water supply network (MWSN) in supplying the daily

water demand of a residential unit according to the region's water tariff scheme to ensure maximum financial benefits. The mathematical formulation of the proposed LP-Daily model is given below:

$$\text{Min. } Z = a \times T_{cap} + \sum_{t=1}^T \sum_{j=1}^J \frac{(b_{tj} \times P_{tj} + (P_t - U_t) \times c_{wt})}{(1+im)^t} \quad (1)$$

s.t.

$$Id_i^t = Id_{i-1}^t + rd_i^t - Ud_i^t \quad \forall t, i \in t \quad (2)$$

$$Id_0^1 = 0 \quad (3)$$

$$Id_0^t = Id_i^{t-1} \quad t = 1, 2, \dots, T \quad (4)$$

$$Id_i^t \leq T_{cap} \quad \forall t, \forall i \quad (5)$$

$$Ud_i^t \leq T_{cap} \quad \forall t, \forall i \quad (6)$$

$$rd_i^t \leq \min\{Rd_i^t, T_{cap}\} \quad \forall t, \forall i \quad (7)$$

$$T_{cap} \leq S_{max} \quad (8)$$

$$Pd_i^t + Ud_i^t = D_{daily} \quad \forall t, \forall i \quad (9)$$

$$T_{cap}, Id_i^t, rd_i^t, Ud_i^t, Pd_i^t \geq 0 \quad \forall t, \forall i \quad (10)$$

where Z is the objective function in Turkish Lira (TL), a is the unit cost of the RWH tank (TL/m³), T_{cap} is the optimum RWH tank size (m³), t is the index for months of the simulation period, T is the total number of months in the simulation period, j is the index for the price level, J is the total number of the price levels in the water tariff scheme, i is the index for the days of a month, b_{tj} is the unit municipal water cost supplied from the MWSN in month t at price level j (TL/m³), P_{tj} is the municipal water volume that is purchased in month t from the MWSN at price level j (m³), P_t is the total municipal water volume supplied from the MWSN in month t (m³), U_t is the total rainwater volume used from the RWH tank in month t (m³), c_{wt} is the unit wastewater cost in month t (TL/m³), and im is the monthly discount rate. The unit municipal water costs incurred due to the water supply from the MWSN and unit wastewater costs throughout the simulation period are estimated assuming that their current unit costs will increase with the inflation rate.

The constraints of the LP-Daily are given in Eqs. (2) to (10) where Id_i^t is the inventory level of the RWH tank at the end of day i of month t (m³), Ud_i^t is the amount of rainwater used from the RWH tank on day i of month t (m³), rd_i^t is the amount of harvested rainwater on day i of month t (m³), $i \in t$ states that index i is for all the days in month t , Rd_i^t is the maximum amount of rainwater that could be harvested on day i of month t (m³), S_{max} is the

maximum allowable RWH tank size (m^3), D_{daily} is the daily water demand (m^3), and Pd_i^t is the municipal water volume purchased from the MWSN on day i of month t (m^3).

Eq. (1) is the objective function that is composed of the summation of the net present value of the total municipal water and wastewater costs and the RWH tank cost. The simulation period is chosen as the lifetime of the RWHS. The amount of rainfall that will be collected and stored in the RWH tank is calculated using historical daily rainfall data. Eq. (2) is the daily water balance equation of the RWH tank. Eq. (3) states that the inventory level of the RWH tank is zero at the beginning of the first day of the simulation period. Eq. (4) ensures that the inventory level of the last day of month $(t - 1)$ in the RWH tank is equal to the inventory level of the RWH tank at the beginning of the first day of month t . Constraints (5) and (6) ensure that the inventory level of the RWH tank on day i of month t and the amount of rainwater used from the RWH tank on day i of month t cannot be greater than the volume of the RWH tank. Constraint (7) guarantees that the amount of harvested rainwater on day i of month t cannot exceed both the maximum amount of rainwater that could be harvested on day i of month t and the volume of the RWH tank. Constraint (8) confirms that the optimum tank size cannot be higher than the maximum allowable RWH tank size (m^3). Eq. (9) states that the daily water demand is supplied from the RWH tank or the MWSN or both. Finally, Eq. (10) is the sign restrictions and ensures that all the decision variables are positive.

The total municipal water volume supplied from the MWSN in month t , P_t , is calculated by summing the municipal water volume purchased from the MWSN in each day of month t :

$$P_t = \sum_{i \in t} Pd_i^t \quad \forall t \quad (11)$$

Assuming the total amount of water purchased from the MWSN in month m^* is P_{m^*} and three price levels are used, (i.e., the first V_1 m^3 is purchased from b_1 TL/ m^3 , the amount between V_1 and V_2 m^3 is purchased from b_2 TL/ m^3 and the remaining is purchased from b_3 TL/ m^3), the water cost that should be paid to the municipality, C , is calculated as follows:

$$\text{If } P_{m^*} \leq V_1 \text{ then } C = b_1 P_{m^*}$$

$$\text{If } V_1 \leq P_{m^*} \leq V_2 \text{ then } C = b_1 V_1 + (P_{m^*} - V_1) b_2 \quad (12)$$

$$\text{If } V_2 \leq P_{m^*} \text{ then } C = b_1 V_1 + b_2 V_2 + (P_{m^*} - V_1 - V_2) b_3$$

The maximum amount of rainwater that could be harvested on day i of month t , Rd_i^t , is calculated using the equation of [49]:

$$Rd_i^t = c_f \times A_{col} \times p_i^t \times 10^{-3} \quad \forall t, \forall i \quad (13)$$

where c_f is the runoff coefficient for the roof, A_{col} is the collector area at the roof (m^2), and p_i^t is the measured rainfall depth on day i of month t (mm).

The total rainwater volume used from the RWH tank in month t , U_t , is calculated by summing the amount of rainwater used from the RWH tank in each day of month t :

$$U_t = \sum_{i \in t} Ud_i^t \quad \forall t \quad (14)$$

The daily water demand, D_{daily} , is calculated using:

$$D_{daily} = W_d \times n \quad (15)$$

where W_d is the average daily water demand per capita ($m^3/cap/day$), and n is the number of residents.

The monthly demand for month t , D_t , is calculated using:

$$D_t = D_{daily} \times I \quad \forall t \quad (16)$$

where I is the total number of days in month t .

2.2. Cost-Benefit Analysis

After the optimum RWH tank size is obtained, the cost-benefit analysis of the RWHS is carried out. Maintenance, wastewater, and municipal water supply costs are increased using the inflation rate for each year of the simulation period. The net present value of all costs are calculated using the discount rate. The cost-benefit analysis compares the net present value of the case where a RWHS is installed and supplies some part of the total water demand to the case where all water demand is supplied from the MWSN. The total cost of the RWHS, C_{total} , is calculated using:

$$C_{total} = Z_{opt} + C_{fixed} \quad (17)$$

where Z_{opt} is the optimum value of the objective function Z (TL), and C_{fixed} is the summation of the fixed costs (TL) which is calculated using:

$$C_{fixed} = C_{inst} + C_{maint} \quad (18)$$

where C_{inst} is the RWHS installation cost (TL) and C_{maint} is the total RWHS maintenance cost that occurs throughout the simulation period (TL) which is calculated using:

$$C_{maint} = \sum_{t=1}^T \frac{c_m}{(1+im)^t} \quad (19)$$

where c_m is the base monthly RWHS maintenance cost (TL). The maintenance cost throughout the simulation period is estimated assuming that the base cost will increase with the inflation rate. The cost of supplying the whole water demand from the MWSN throughout the simulation period, C_{net} (TL), is calculated using:

$$C_{net} = \sum_{t=1}^T \sum_{j=1}^J \frac{b_j}{(1+im)^t} P_{tj} + \sum_{t=1}^T \frac{c_w}{(1+im)^t} D_t \quad (20)$$

The net financial benefit of the RWHS, NFB , is defined as the difference between the cost of supplying the whole water demand from the MWSN and the total cost of the RWHS:

$$NFB = C_{net} - C_{total} \quad (21)$$

When the NFB is negative, the RWHS ends in financial loss, and the RWHS is found to be infeasible. In addition to the NFB , the discounted payback period of the RWHS investment, which is the year at which cumulative discounted net cash-flow becomes zero, is calculated.

2.3. Water Balance Simulation Model

Tank size, daily rainfall, daily water demand, daily rainwater supply, daily tank spillage, and municipal water supply from the network are taken into account in the water balance simulation model (WBSM). The daily water balance of the RWH tank is carried out for a set of selected alternative tank sizes. The WBSM uses the yield-before-spillage algorithm.

Daily inflow to the RWH tank is calculated using Eq. (13). If the sum of daily inflow and the inventory level of the RWH tank at the end of the previous day is smaller than the daily water demand, daily rainwater supply from the RWH tank equals the sum of daily inflow and the inventory level of the RWH tank at the end of the previous day. Otherwise, daily rainwater supply from the RWH tank equals the daily water demand. Spill is the excess rainfall that exceeds the RWH tank size. Spill on day i of month t , SP_i^t (m^3), is calculated using Eqs. (22) or (23) [28]:

$$\text{If } Rd_i^t + Id_{i-1}^t - D_{daily} > T_{max} \text{ then } SP_i^t = Rd_i^t + Id_{i-1}^t - D_{daily} - T_{max} \quad (22)$$

$$\text{If } Rd_i^t + Id_{i-1}^t - D_{daily} \leq T_{max} \text{ then } SP_i^t = 0 \quad (23)$$

where T_{max} is the RWH tank size (m^3).

If spill on day i is calculated to be smaller than or equal to zero, the RWH tank inventory level at the end of day i is determined by subtracting the amount of rainwater supplied from the RWH tank on day i from the inventory level at the end of the previous day plus inflow on day i . Otherwise, the RWH tank inventory level at the end of day i is equal to the RWH tank size. For the detailed methodology of the WBSM on a daily scale, see [28]. Cost-benefit analysis of the RWHS is carried out to calculate the NFB for each alternative tank size using Eq. (21).

2.4. Performance Indicators: Resilience, Vulnerability, Reliability, and Water Saving

Resilience is the inverse of the mean value of the time the system spends in an unsatisfactory state [50]. In this study, the unsatisfactory state is considered to be the days in which water demand is not fully supplied by the RWHS. Such days are referred to as deficit events. Resilience, Res , is calculated using [50]:

$$Res = \left\{ \frac{1}{M} \sum_{k=1}^M d_k \right\}^{-1} \quad (24)$$

where d_k is the duration of the k^{th} failure event and M is the total number of failure events.

Vulnerability is an indicator of the severity of RWHS failure. In this study, vulnerability is estimated as the mean value of the deficit events (i.e., the total amount of water supplied from the MWSN during deficit events divided by the total number of deficit events) as suggested by [51]. Vulnerability, Vul , is calculated using [50]:

$$Vul = \frac{1}{M} \sum_{k=1}^M v_k \quad (25)$$

where v_k is the deficit volume of the k^{th} failure event.

Reliability is a widely used indicator to evaluate the rainwater supply performance of a RWHS. In this study, water demand is supplied either by the RWHS, the MWSN or both and a failure event does not occur throughout the simulation period. Therefore, the volumetric reliability of the RWHS which is the percent of the water demand that can be supplied from the RWHS is considered for reliability calculations. Reliability, Rel , is calculated using [12]:

$$Rel = \frac{\sum_{t=1}^T \sum_{i=1}^N U d_i^t}{D_{daily} \times N} \times 100 \quad (26)$$

where N is the total number of days in the simulation period.

Finally, water saving, Ws (m^3), is the average annual rainwater used to supply the demand:

$$Ws = \frac{\sum_{t=1}^T \sum_{i=1}^N U d_i^t}{A} \quad (27)$$

where A is the total number of years in the simulation period.

2.5. Sensitivity Analysis

The sensitivity analysis is carried out to investigate the effects of collector area and average daily water demand per capita on the optimum tank size and the discounted payback period. In the sensitivity analysis, each of these two parameters is varied while keeping all other parameters constant. The LP model is run repeatedly between the limits of the analysed parameters.

2.6. Study Area and Rainfall Characteristics

Cyprus is an island in the Eastern Mediterranean region with a semi-arid climate where summers are hot and long, and winters are warm and short. Water resources are limited and water scarcity problems are encountered. December and January are the rainiest months on the island, while July and August are the driest months. The rainy period is usually from November to March. In this study, 33 case study sites are selected in Northern Cyprus. The rainfall characteristics throughout these sites vary significantly.

The European Standard suggests that large and complex RWHS projects need to be designed using at least five years of daily rainfall data series [52]. This study uses daily rainfall records

of 33 meteorological stations from 1985 to 2015 obtained from the Meteorological Department of Northern Cyprus.

The average annual rainfall between 1985- 2015 at the study area is 386 mm. The average annual rainfall between 1985- 2015 are calculated as 470 mm for Girne (Kyrenia), 309 mm for Lefkoşa (Nicosia), 346 mm for Mağusa (Famagusta), 554 mm for Lapta, and 291 mm for Güzelyurt (Morphou). In order to demonstrate the rainfall regime at the study area, the average monthly rainfall between 1985- 2015 at the selected sites, such as Girne, Lefkoşa, Mağusa, Lapta, and Güzelyurt are presented in Fig. 1.

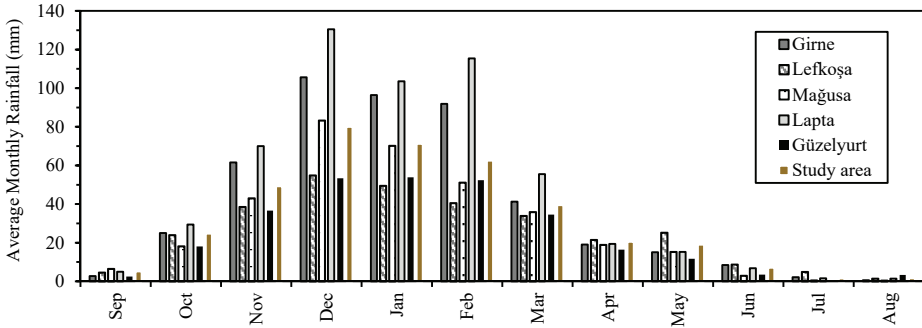


Fig. 1 - Average monthly rainfall between 1985- 2015 at the selected sites and the average in the study area

2.7. Input Data

The simulation for LP-Daily and LP-Monthly models and the WBSM is performed for a period of 30 years ($N = 10957$ days or $T = 360$ months). Accordingly, the lifetime of the RWHS is assumed to be 30 years. The wastewater collection and treatment networks are not available in all urban areas in the study area. However, the design and construction of new wastewater network projects are on the agendas of many municipalities. Despite the lack of a wastewater collection network in some sites, the wastewater tariff is included in the analyses for the sake of generalization. For the first year of the simulation period, each unit of water supplied from the MWSN is assumed to be charged an additional wastewater cost of 1 TL/m^3 ($c_w = 1 \text{ TL/m}^3$). The wastewater cost is increased according to the average annual inflation rate between 2005 and 2021 which is taken as 11.3% [53] throughout the simulation duration.

Many municipalities at the study area employ an increasing block rate water tariff to promote water savings, while others use a fixed water charge. For example, Lapta Municipality employs a fixed municipal water charge of 5 TL/m^3 . In an increasing block rate water tariff, the unit water cost increases as the water volume purchased from the MWSN increases. For example, Dipkarpaz Municipality sets the unit cost of water as 5 TL/m^3 up to 20 m^3 and 6 TL/m^3 when the amount exceeds 20 m^3 within a month [54]. Current water tariffs of each study site that are used as inputs for the models are obtained by directly contacting the

municipalities or from the local newspaper Havadis, issued on May 15th, 2017. The inflation rate is used to estimate the future prices of the simulation duration.

A rooftop RWHS is assumed to supply the domestic water demand of a single house with four residents ($n = 4$). The average daily domestic water (i.e., tap water) demand per capita in Northern Cyprus is taken as 250 liters ($W_d = 0.25 \text{ m}^3/\text{cap}/\text{day}$) [55]. It is assumed that tap water is not used for drinking purposes so the cost of a simple filter but no treatment cost is included. The roof of the single house is assumed to be a flat concrete roof with a runoff coefficient, c_f , of 0.9 [56]. Rainwater is assumed to be harvested through a 200 m^2 collector ($A_{col} = 200 \text{ m}^2$) at the roof. Some municipalities prohibit building a water tank size larger than 20 m^3 for private use, so the maximum allowable tank size is set to 20 m^3 ($S_{max} = 20 \text{ m}^3$).

The existing MWSN of the single house is assumed to be retrofitted for the RWHS installation. The existing water pump that is already connected with the single house's MWSN system to transfer municipal water from the main water tank to the single house is assumed to be used to transfer the harvested rainwater. Commonly, a water pump is used in residential units in Northern Cyprus to pressurize the water supplied from the MWSN. The user is responsible for the electricity consumption cost of the water pump. It is assumed that the same water pump will be used for the harvested rainwater, so that water pump's electricity cost is not included in the cost-benefit analysis.

Current installation (i.e., retrofitting the existing MWSN of the single house for the RWHS installation) and base annual maintenance costs of the RWHS are taken as 1500 TL ($f_{ini} = 1500 \text{ TL}$) and 102 TL ($c_m = 8.5 \text{ TL}/\text{month}$), respectively. These costs are provided by a local plumbing service supplier (Olçay Uzuçar Plumbing Service, Personal communication in December 2019). The maintenance cost is estimated using the inflation rate. Above-ground water tanks in gardens are common in Northern Cyprus. Therefore, in this study it is assumed that the RWH tank is positioned above-ground; so the excavation cost is neglected. This assumption is realistic for Northern Cyprus but excavation cost may need to be considered for other regions. The tank is assumed to be made of polyethylene and the unit cost is taken as $600 \text{ TL}/\text{m}^3$ ($a = 600 \text{ TL}/\text{m}^3$) [57]. The net present values of the costs are calculated using an average annual discount rate of 11.7% which is estimated using 2005-2021 data ($im = 0.98\%$ per month) [58].

3. RESULTS AND DISCUSSION

The validation of the LP model with the WBSM, a comparison of LP with daily and monthly time steps, the spatial evaluation of RWHS performances, and finally, sensitivity analysis are provided below.

3.1. Comparison of LP-Daily Model and WBSM

Our model differs from the water balance model approach since there is no need to specify alternative tank sizes beforehand and to individually evaluate the feasibility of each alternative tank size. The LP model searches the whole domain and finds the optimum tank size resulting in the maximum revenue in a single run. To validate the LP-Daily model, the

results are compared to those obtained from the WBSM. This analysis is carried out for Lapta, which receives an average annual rainfall of 554 mm. The WBSM is run on tank sizes from 1 m³ to 10 m³ with increments of 1 m³. As seen in Fig. 2, the maximum net financial benefit occurs at a tank size between 4 m³ and 5 m³.

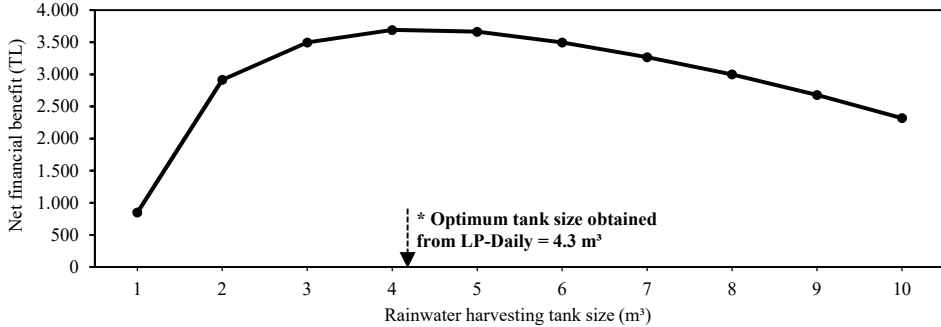


Fig. 2 - Results of the WBSM for Lapta

The optimum tank size is identified as 4.3 m³ with the LP-Daily model in a single run. On the other hand, a single run of the WBSM provides the net financial benefit associated with the chosen tank size. Thus, the WBSM is run 10 times to obtain the maximum net financial benefit curve given in Fig. 2. As can be seen from Fig. 2, The WBSM results indicate that the optimum tank size (i.e., the tank size with the highest net financial benefit) is between 4 m³ and 5 m³ which contains the LP-Daily model result of 4.3 m³. Hence, identifying the tank size with the highest net financial benefit is a trial and error procedure when the WBSM is used. Moreover, the WBSM is not as accurate as the LP model. LP is an alternative approach to the WBSM and will save time, especially when the RWH analysis is required at numerous sites with varying characteristics.

3.2. Comparison of LP-Daily and LP-Monthly Models

The results of LP-Daily and LP-Monthly models for Lapta are compared. The time required to solve LP-Daily and LP-Monthly for the 30-year simulation period differ significantly. For example, while the LP-Monthly model runs in 2 minutes, the LP-Daily model requires 1.5 hours to complete each run with OpenSolver software Ver. 2.9.0 installed on a computer with Intel® Core™ i5-9400F CPU @ 2.90GHz and 16 GB RAM. The results of LP-Monthly [36] and LP-Daily models for Lapta are given in Table 1.

As seen in Table 1, a larger tank size is obtained, and the system is assessed as an infeasible investment (i.e., a negative *NFB* value) when monthly time steps are used. Consequently, the total cost of the RWHS could not be paid back within the simulation period. On the other hand, the discounted payback period of the RWHS is calculated as less than 17 years when daily time steps are used. The difference in the amount of water savings between the models' results affects the financial feasibility calculations considerably since that difference is compensated using municipal water.

Table 1 - Comparison of LP-Monthly [36] and LP-Daily models' results for Lapta

Model	Optimum tank size (m ³)	Tank cost (TL)	Cost of water savings (TL)	Municipal water and wastewater costs (TL)	Net financial benefit (TL)	Discounted payback period (year)
LP-Monthly	8.4	5,065	7,380	46,700	-1,700	-
LP-Daily	4.3	2,600	10,350	43,730	3,730	16.6

When both models are investigated in detail, it is observed that the amount of rainwater harvested and utilized is underestimated when monthly time steps are used. Utilization of daily time steps simulates the RWH tank (i.e., filling and emptying) more realistically. The average monthly water supply and demand relations of the two models throughout the simulation period are presented in Fig. 3.

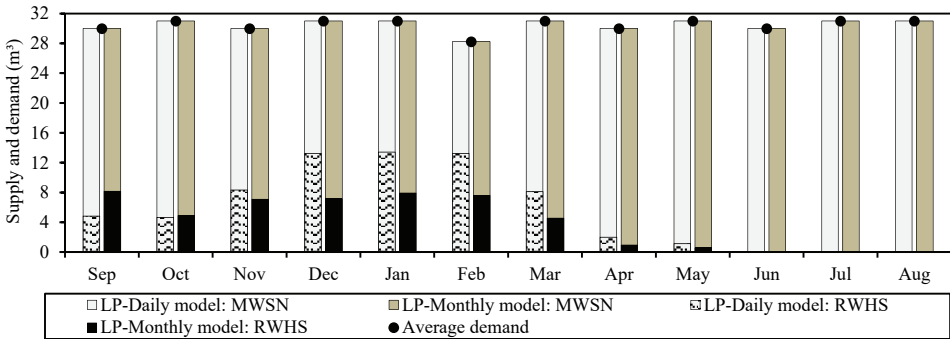


Fig. 3 - Average monthly water supply and demand relations of LP-Daily and LP-Monthly models throughout the simulation period for Lapta

As seen in Fig. 3, higher percentages of the monthly demands - other than for September - are supplied by the RWHS in the daily model compared to that of the monthly model. For example, around 13 m³ of the total average demand of 31 m³ is supplied by the tank in January when LP-Daily is used. This shows that, according to LP-Daily, the tank (i.e., 4.3 m³ as given in Table 1) is filled and emptied multiple times on the average to supply the demand in January. However, when monthly time steps are used, the water balance equation is satisfied for each month. Thus the tank can only be filled and emptied once. This causes the part of the average demand supplied by the tank to be at most 8.4 m³ (i.e., the optimum RWH tank size for LP-Monthly as given in Table 1). Similar underestimations of water savings occur in the other months as well. The water balance given in Eq. (2) is satisfied for each day in LP-Daily while it is satisfied for each month in LP-Monthly. Thus in LP-Monthly, the maximum amount of water demand that can be supplied by the tank is equal to the optimum tank size. Once the tank is filled with rainwater in a month, rainfall received in the remaining days of that month cannot be harvested and utilized, but wasted as overflow. The reader may refer to [35] and [36] for detailed explanations of LP-Monthly results.

Average annual water saving at Lapta is calculated as 69 m³ with the LP-Daily model, whereas it is 49 m³ with the LP-Monthly model. It is concluded that the utilization of monthly time steps leads to the incorrect judgment of the less efficient use of the RWH tank capacity. For realistic results, daily time steps should be used as also suggested by [39, 40, 41].

3.3. Spatial Evaluation of the Performance of the Rainwater Harvesting Systems

The LP-Daily model is configured and run for each site. The results are shown in Table S1. The optimum RWH tank sizes range from 2.1 m³ to 5.4 m³. *NFBs* at 33 sites vary and result in the discounted payback periods ranging from 12 years to 28 years. The minimum discounted payback period (i.e., 12.4 years) is obtained at Beylerbeyi, which receives 500 mm of average annual rainfall and has a relatively high average water cost (i.e., 43.6 TL/m³).

As given in Section 2.4 in detail, resilience, vulnerability, and reliability are commonly used performance indicators of water supply systems. The resilience values of RWHSs at 33 sites range from 0.061 (day/failure event)⁻¹ to 0.111 (day/failure event)⁻¹ while the vulnerability values range from 8.75 m³/failure event to 16.02 m³/failure event (see Table S1). Higher resilience means the RWHS returns to supplying the water demand state quickly and higher vulnerability means the average deficit volume (i.e., demand that the RWHS cannot supply) is high. The highest resilience and the lowest vulnerability are achieved at Tatlısu which receives an average annual rainfall of 511 mm, while Dörtyol which receives 273 mm average annual rainfall has the minimum resilience and the maximum vulnerability. For Tatlısu, the total duration of failure events is 9180 days and the total number of failure events is 1019. Thus, the resilience for Tatlısu is 1019/9180=0.111 (day/failure event)⁻¹. On the other hand, for Dörtyol, the total duration of failure events is 10118 days and the total number of failure events is 616; and its resilience is 616/10118=0.061 (day/failure event)⁻¹. Although the total number of failure events are less for Dörtyol, the average duration of each failure event is longer, meaning it takes longer to recover (i.e. it takes longer to go back to non-failure state). Thus, as the average duration of the failure event increases the resilience decreases. Vulnerability, on the other hand is related with the average amount of deficit. For Tatlısu, the total deficit volume of all failure events is 8917 m³, thus its vulnerability is 8917/1019=8.75 m³/failure event; while for Dörtyol, total deficit volume of all failure events is 9866 m³, thus its vulnerability is 9866/616=16.02 m³/failure event. As expected, when the average duration of the failure event is longer the deficit is higher and the vulnerability is higher. Except for Lapta, vulnerability values are lower (i.e. range from 8 m³/failure event to 9 m³/failure event) at the sites which receive higher than 480 mm average annual rainfall. As the performance indicators address, RWHSs should be used as auxiliary water supply systems at semi-arid regions due to low rainfall periods lasting for 4- 5 months and irregular rainfall pattern by months.

The RWHS reliability range is between 10% and 20% for the study area (Table S1). This means that at most 20% of the total demand can be supplied by the harvested rainwater. Although reliabilities higher than 20% cannot be maintained for the semi-arid Northern Cyprus, at 29 of the 33 sites, RWHSs are found to be financially feasible (i.e., resulted in net financial benefit). Low reliability values are mainly due to low rainfall and its non-uniform distribution throughout the year. As can be seen in Fig. 4, as the average annual rainfall decreases, the reliability decreases almost linearly. The maximum reliability of 20% is

observed at Kantara which receives 562 mm average annual rainfall whereas Dörtyol has the minimum reliability of 10% and its average annual rainfall is 273 mm. These results are in agreement with literature. Reliabilities between 10% and 20% in supplying non-potable water demands between 360 L and 720 L were obtained using rainwater collector areas between 120 m² and 240 m² and tank sizes between 1 m³ and 5 m³ for Tabriz, Iran which receives an average annual rainfall of 288 mm [59]. Additionally, similar to our results, [29] calculated reliabilities between 12% and 23% in Central and South-West Melbourne, Australia, receiving 465 mm and 374 mm of average annual rainfalls in dry years, respectively using a roof area of 200 m², a non-potable water demand of 600 L and tank sizes ranging from 1 m³ to 10 m³.

It is observed that there is a significant difference in rainfall amounts between the rainy period (i.e., from November to March) and the whole year for Northern Cyprus. When the reliabilities are calculated only for the rainy period, significantly higher values are obtained (i.e., 18% - 37%), sometimes overflows of tanks are observed. For example, for Lapta, the reliability of the RWHS for the rainy period is 37%, while it is only 19% when the whole year is considered. This is due to the semi-arid climatic characteristics of the study area where little rainfall is received outside the rainy period. The long dry period between June and September (see Fig. 1) decreases the reliability. In line with our findings, [62] concluded that the rainfall distribution is a major variable on non-potable water savings via RWH in Beit-Dagan, Tel Aviv, Israel where roughly 90% of the rainfall occurs between November and March and less than 1% between May and September.

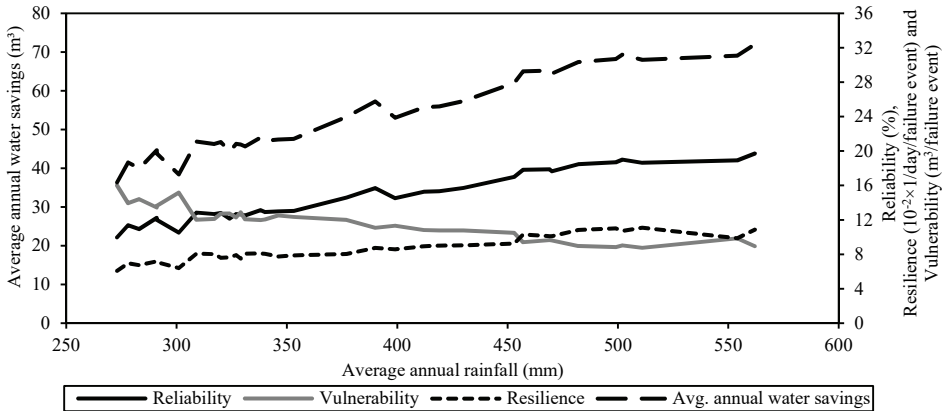


Fig. 4 - Water savings, reliability, resilience, vulnerability and annual rainfall relations

Rainfall contours together with financial feasibilities of RWHSs are shown in Fig. 5. The RWHS investments are found to be financially feasible at 29 of the 33 sites. We find that the range of the optimum tank sizes in this study is similar to those of [47] where financially feasible tank sizes are between 1 m³ and 5 m³ for warm semi-arid Lahore, Pakistan, which receives 667 mm average annual rainfall. We also find that average annual water savings of a single house range from 36 m³ to 72 m³ and are close to the water savings of combined

water use in household and irrigation obtained across Australia for tank sizes between 1 m³ and 5 m³ [60, 48].

To conclude, when the average annual rainfall is more than 300 mm, RWH tank sizes larger than 2.5 m³ can provide more than 12% of the domestic water demand of a single house in Northern Cyprus. If widespread rainwater harvesting is realized, domestic water savings will contribute to sustainable water resources management of water-scarce Northern Cyprus. RWH may offer additional benefits such as stormwater collection and reducing energy, maintenance and operational costs of existing water supply systems, but these are out of the scope of this study [61].

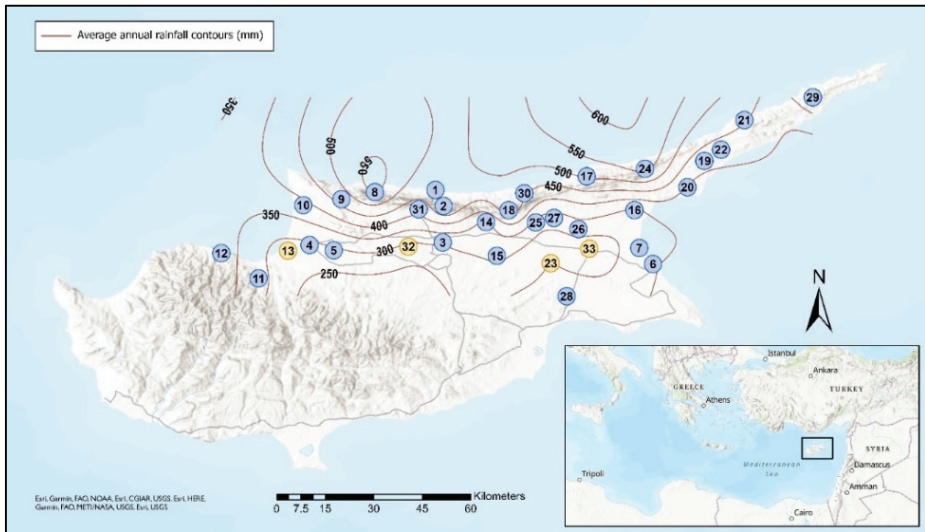


Fig. 5 - Map of the case study sites in Northern Cyprus. Blue marked sites are the locations where the RWHS is financially feasible, while the financially infeasible locations are marked with yellow.

The combined effect of rainfall characteristic and the water cost on the net financial benefit is shown in Fig. 6. The average annual rainfall is used as an indicator of the rainfall characteristic. As seen in Fig. 6, at the sites where water cost and rainfall are high, RWHSs have positive *NFBs*. Except for Lefkoşa, all the sites where the RWHSs' initial investment costs are compensated in less than 17 years are located at the north and northeast shores of the island, which receive higher than average annual rainfall of 390 mm. At Lefkoşa, the average annual rainfall throughout the 30-year simulation period is one of the lowest (i.e., 309 mm) whereas the average unit water cost is the highest (i.e., 45.1 TL/m³). The RWHS is found to be financially feasible for Lefkoşa. Kantara, on the other hand, has the highest average annual rainfall (i.e., 562 mm), but the average municipal water supply cost is relatively low (i.e., 26.8 TL/m³), resulting in a lower *NFB* than that of Lefkoşa. As also noted by [63], the economic feasibility of RWH relies on many elements such as water price, amount of rainfall, and capital cost; our results demonstrate that both water cost and amount of rainfall become critical for Northern Cyprus in the financial feasibility of the RWHS.

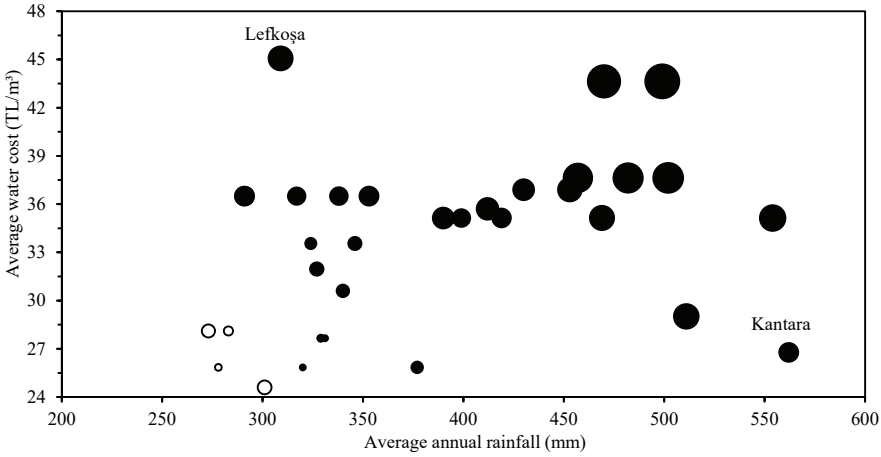


Fig. 6 - Net financial benefits of RWHSs with respect to average water costs and average annual rainfalls for 33 sites. Filled black circles represent positive net financial benefit while empty circles represent negative net financial benefit

3.4. Sensitivity Analysis

In this section, sensitivity analysis results of the LP-Daily model for Lapta are given. Effects of the collector area and the average daily water demand per capita on the optimum RWH tank size and the discounted payback period are investigated. The sensitivity analysis results for the collector area are given in Fig. 7. The discounted payback periods range from 28 years to 13.5 years when the collector area changes from 75 m² to 500 m². The RWHS is not financially feasible for collector areas of less than 75 m² for Lapta with the assumptions explained in Section 2.7. This indicates that although the RWHS with a collector area of less than 75 m² can supply some portion of the water demand at Lapta, costs associated with the RWHS exceeds its benefits, resulting in financial loss. As the collector area increases, the optimum tank size also increases to accommodate larger amounts of harvested rainwater, and consequently, the discounted payback period decreases. Likewise, [35] analyzed roof areas between 80 m² and 300 m² as rainwater collectors and found that optimum tank sizes increased from around 1 m³ to 3 m³, while financial benefits increased from 600 TL to 740 TL for Girne.

The following analysis is carried out for Lapta by changing the average daily domestic water demand per capita between 50 lt/cap/day and 650 lt/cap/day. The results are given in Fig. 8. For daily domestic water demand per capita of 150 lt/cap/day and higher, the discounted payback period is calculated to be between 15 to 19 years. The RWHS ends in financial losses at Lapta if daily domestic water demand per capita is less than 50 lt/cap/day. For Girne, [35] found that the RWHS is financially infeasible for daily water demand of less than 100 lt/cap/day using a monthly time-step LP model. These results show the effect of water demand on financial feasibility.

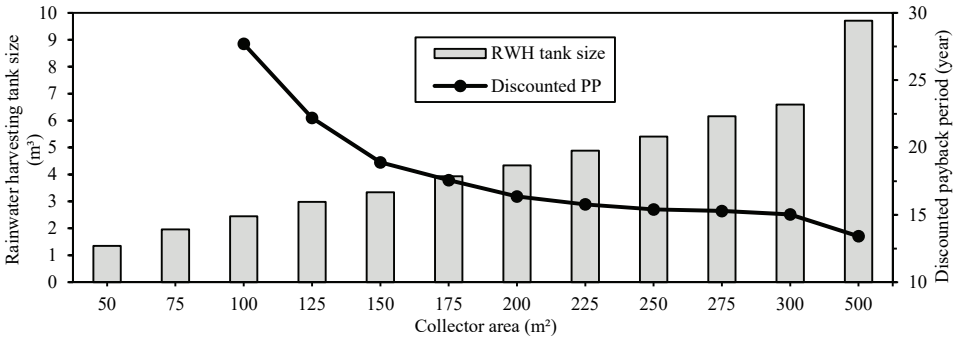


Fig. 7 - Effects of collector areas on rainwater harvesting tank sizes and discounted payback periods for Lapta

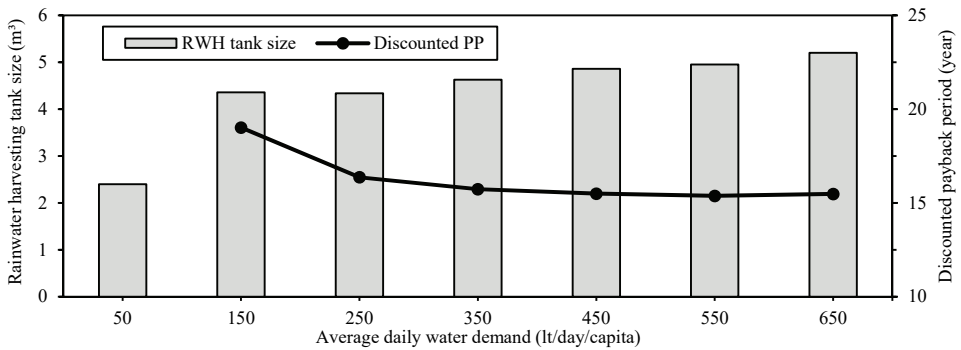


Fig. 8 - Effects of average daily water demand per capita on rainwater harvesting tank sizes and discounted payback periods for Lapta

As expected, when daily water demand per capita increases, the discounted payback period decreases until 550 lt/cap/day then levels off for larger values. This implies that the use of a larger tank size is unfavorable with respect to the increase in the benefits of the RWHS serving for a single house. Unlike [25], our sensitivity analysis results show that water demand does not significantly affect the optimum tank size for a single house at Lapta. In the current study, the average annual rainfall ranges from 273 mm to 562 mm at the study area and rainfall is mostly received during a short rainy period while the annual average rainfall is over 1000 mm in [25]. We believe that the amount of rainfall and its distribution throughout the year is the main reason for the differing effects of water demands on optimum tank sizes. At Lapta, due to limited availability of rainfall, increasing the water demand over 350 lt/cap/day does not significantly affect the optimum tank size.

Sensitivity analysis results demonstrate that the collector area plays a significant role in the optimum tank size and the financial feasibility is more sensitive to the collector area than water demand for Lapta. Thus, the RWHS should be designed to allow rainwater harvesting

from the maximum possible area to maximize the benefits and reliability of the system. Similar conclusions were also reached for Australia, Iran, and Pakistan [29, 57, 47].

4. CONCLUSION

In this study, a single objective *LP model with daily time steps* is introduced to find the optimum RWH tank size by minimizing costs. The proposed model is run for the selected 33 sites from semi-arid Northern Cyprus in the Eastern Mediterranean region where average annual rainfalls ranging from 273 mm to 562 mm. The significant conclusions of this study are given as follows:

- Comparison of the LP-Daily model and WBSM reveals that both models generate consistent optimum tank sizes but the LP-Daily model saves time since it requires a single run.
- It is demonstrated that 29 of the 33 studied sites RWHSs are feasible (i.e., have positive financial benefits). However, it is pertinent to note the relatively low reliability of RWHSs, indicating their auxiliary role vis-à-vis the existing municipal water supply network. Beyond financial considerations, RWHS desirability is contingent upon factors such as uncertainties in sources of existing municipal water supply and tariffs. Given these circumstances, rainwater harvesting emerges as a potential alternative of existing water sources, warranting governmental incentives for its adoption. Such incentives may facilitate RWHS implementation among homeowners, notwithstanding extended payback periods.
- RWHSs' initial investment costs are generally compensated in less than 15 years at the north and northeast shores of the island, where the average annual rainfall is higher than 390 mm.
- The LP-Daily model yields a notably reduced optimum tank size and provides a more accurate assessment of financial feasibility compared to the LP-Monthly model. The utilization of monthly time steps may lead homeowners to incorrect investment decisions.

The main contribution of this study lies in its spatial analysis of the assessment of RWHSs feasibility for the first time in water-scarce Northern Cyprus. The outcomes of this research hold promise for informing the development of sustainable water resource management frameworks, particularly pertinent to Mediterranean islands and semi-arid regions. In future investigations, our aim is to integrate environmental cost metrics into the existing LP-Daily model, thereby facilitating a comprehensive evaluation of the environmental advantages associated with RWHS implementation.

List of Symbols

Acronyms

LP	Linear programming
MWSN	Municipal water supply network

RWHS	Rainwater harvesting system
TL	Turkish Lira
WBSM	Water balance simulation model
<u>Indexes</u>	
A	Total number of years in the simulation period
i	Days of a month
I	Total number of days in month t
j	Price level
J	Total number of the price levels in the water tariff scheme
N	Total number of days in the simulation period
t	Months of the simulation period
T	Total number of months in the simulation period
<u>Parameters</u>	
a (TL/m ³)	Unit cost of the RWH tank
A_{col} (m ²)	Collector area at the roof
b_j (TL/m ³)	Unit municipal water cost supplied from the MWSN at price level j
c_f	Runoff coefficient for the roof
C_{fixed} (TL)	Summation of the fixed costs
C_{inst} (TL)	RWHS installation cost
c_m (TL/month)	Base monthly RWHS maintenance cost
C_{maint} (TL)	Total RWHS maintenance cost that occurs throughout the simulation period
C_{net} (TL)	Cost of supplying the whole water demand from the MWSN
C_{total} (TL)	Total cost of the RWHS
c_w (TL/m ³)	Unit wastewater cost
D_{daily} (m ³)	Daily demand
d_k	Duration of the k^{th} failure event
D_t (m ³)	Total demand in month t
im	Monthly discount rate
k	Failure event
M	Total number of failure events
NFB	Net financial benefit
n	Number of residents
p_i^t (mm)	Measured rainfall depth on day i of month t

P_t (m ³)	Total municipal water volume supplied from the MWSN in month t
P_{tj} (m ³)	Municipal water volume that is purchased in month t from the MWSN at price level j
Rd_i^t (m ³)	Maximum amount of rainwater that can be harvested on day i of month t
Rel	Reliability
Res	Resilience
S_{max} (m ³)	Maximum allowable RWH tank size
SP_i^t (m ³)	Spill on day i of month t
T_{max} (m ³)	RWH tank size
U_t (m ³)	Total rainwater volume used from the RWH tank in month t
v_k	Deficit volume of the k^{th} failure event
Vul	Vulnerability
W_d (m ³ /cap/day)	Average daily water demand per capita
Ws (m ³ /year)	Average annual water saving

Variables

Id_i^t (m ³)	Inventory level of the RWH tank at the end of day i of month t
Pd_i^t (m ³)	Municipal water volume purchased from the MWSN on day i of month t
rd_i^t (m ³)	Amount of harvested rainwater on day i of month t
T_{cap} (m ³)	Optimum RWH tank size
Ud_i^t (m ³)	Amount of rainwater used from the RWH tank on day i of month t
Z (TL)	Objective function
Z_{opt} (TL)	Optimum objective function value

Acknowledgement

The authors of this study thank to the Meteorological Authority of Northern Cyprus for providing the necessary rainfall data and we would also like to thank to Prof. Dr. Hasan Güngör for his valuable discussions.

References

- [1] UN (United Nations). (2015). International decade for action water for life 2005-2015. Retrieved July 25, 2020, from https://www.un.org/waterforlifedecade/water_and_sustainable_development.shtml

- [2] Solomon, H., & Smith, H. H. (2007). Effectiveness of mandatory law of cistern construction for rainwater harvesting on supply and demand of public water in the U.S. Virgin Islands. Seventh Caribbean Islands Water Resources Congress, University of The Virgin Islands, St. Croix, USVI (pp. 75-80).
- [3] Han, M., & Ki, J. (2010). Establishment of sustainable water supply system in small islands through rainwater harvesting (RWH): Case study of Guja-do. *Water Science and Technology*, 62(1), 148-153. <https://doi.org/10.2166/wst.2010.299>
- [4] Wallace, C. D., Bailey, R. T., & Arabi, M. (2015). Rainwater catchment system design using simulated future climate data. *Journal of Hydrology*, 529, 1798-1809. <https://doi.org/10.1016/j.jhydrol.2015.08.006>
- [5] Quigley, N., Beavis, S. G., & White, I. (2016). Rainwater harvesting augmentation of domestic water supply in Honiara, Solomon Islands. *Australian Journal of Water Resources*, 20(1), 65-77. <https://doi.org/10.1080/13241583.2016.1173314>
- [6] Donohue, M. J., Macomber, P. S., Okimoto, D., & Lerner, D. T. (2017). Survey of Rainwater Catchment Use and Practices on Hawaii Island. *Journal of Contemporary Water Research & Education*, 161(1), 33-47. <https://doi.org/10.1111/j.1936-704x.2017.3250.x>
- [7] Bailey, R. T., Beikmann, A., Kottermair, M., Taboroši, D., & Jenson, J. W. (2018). Sustainability of rainwater catchment systems for small island communities. *Journal of Hydrology*, 557, 137-146. <https://doi.org/10.1016/j.jhydrol.2017.12.016>
- [8] Ruso, M. (2021). Rainwater Harvesting Analysis for Northern Cyprus [M.S. - Master of Science]. Middle East Technical University – Northern Cyprus Campus.
- [9] Jamali, B., Bach, P. M., & Deletic, A. (2020). Rainwater harvesting for urban flood management - An integrated modelling framework. *Water Research*, 171, 115372. <https://doi.org/10.1016/j.watres.2019.115372>
- [10] van Dijk, S., Lounsbury, A. W., Hoekstra, A. Y., & Wang, R. (2020). Strategic design and finance of rainwater harvesting to cost-effectively meet large-scale urban water infrastructure needs. *Water Research*, 184, 116063. <https://doi.org/10.1016/j.watres.2020.116063>
- [11] Abdulla, F. A., & Al-Shareef, A. (2009). Roof rainwater harvesting systems for household water supply in Jordan. *Desalination*, 243(1-3), 195-207. <https://doi.org/10.1016/j.desal.2008.05.013>
- [12] Wang, C.-H., & Blackmore, J. M. (2012). Supply–Demand Risk and resilience assessment for household rainwater harvesting in Melbourne, Australia. *Water Resources Management*, 26(15), 4381–4396. <https://doi.org/10.1007/s11269-012-0150-x>
- [13] Pelak, N., & Porporato, A. (2016). Sizing a rainwater harvesting cistern by minimizing costs. *Journal of Hydrology*, 541, 1340-1347. <https://doi.org/10.1016/j.jhydrol.2016.08.036>

- [14] Kwon, Y., Hwang, J., & Seo, Y. (2018). Performance of a RBSN under the RCP scenarios: A case study in South Korea. *Sustainability*, 10(4), 1242. <https://doi.org/10.3390/su10041242>
- [15] Park, D., & Um, M. J. (2018). Sustainability index evaluation of the rainwater harvesting system in six US urban cities. *Sustainability*, 10(2), 280. <https://doi.org/10.3390/su10010280>
- [16] Khastagir, A., & Jayasuriya, N. (2011). Investment Evaluation of Rainwater Tanks. *Water Resources Management*, 25(14), 3769-3784. <https://doi.org/10.1007/s11269-011-9883-1>
- [17] Roebuck, R. M., Oltean-Dumbrava, C., & Tait, S. (2011). Whole life cost performance of domestic rainwater harvesting systems in the United Kingdom. *Water and Environment Journal*, 25(3), 355-365. <https://doi.org/10.1111/j.1747-6593.2010.00230.x>
- [18] Ward, S., Memon, F., & Butler, D. (2012). Performance of a large building rainwater harvesting system. *Water Research*, 46(16), 5127-5134. <https://doi.org/10.1016/j.watres.2012.06.043>
- [19] Fernandes, L. F., Terêncio, D. P., & Pacheco, F. A. (2015). Rainwater harvesting systems for low demanding applications. *Science of The Total Environment*, 529, 91-100. <https://doi.org/10.1016/j.scitotenv.2015.05.061>
- [20] Morales-Pinzón, T., Rieradevall, J., Gasol, C. M., & Gabarrell, X. (2015). Modelling for economic cost and environmental analysis of rainwater harvesting systems. *Journal of Cleaner Production*, 87, 613-626. <https://doi.org/10.1016/j.jclepro.2014.10.021>
- [21] Karim, M. R., Bashar, M. Z., & Imteaz, M. A. (2015). Reliability and economic analysis of urban rainwater harvesting in a megacity in Bangladesh. *Resources, Conservation and Recycling*, 104, 61-67. <https://doi.org/10.1016/j.resconrec.2015.09.010>
- [22] Lopes, V. A., Marques, G. F., Dornelles, F., & Medellín-Azuara, J. (2017). Performance of rainwater harvesting systems under scenarios of non-potable water demand and roof area typologies using a stochastic approach. *Journal of Cleaner Production*, 148, 304-313. <https://doi.org/10.1016/j.jclepro.2017.01.132>
- [23] Bashar, M. Z., Karim, M. R., & Imteaz, M. A. (2018). Reliability and economic analysis of urban rainwater harvesting: A comparative study within six major cities of Bangladesh. *Resources, Conservation and Recycling*, 133, 146-154. <https://doi.org/10.1016/j.resconrec.2018.01.025>
- [24] Karim, M. R., Sakib, B. M., Sakib, S. S., & Imteaz, M. A. (2021). Rainwater harvesting potentials in commercial buildings in Dhaka: Reliability and economic analysis. *Hydrology*, 8(1), 9. <https://doi.org/10.3390/hydrology8010009>
- [25] Ghisi, E., Bressan, D. L., & Martini, M. (2007). Rainwater tank capacity and potential for potable water savings by using rainwater in the residential sector of southeastern Brazil. *Building and Environment*, 42(4), 1654-1666. <https://doi.org/10.1016/j.buildenv.2006.02.007>

- [26] Aladenola, O. O., & Adeboye, O. B. (2010). Assessing the Potential for Rainwater Harvesting. *Water Resources Management*, 24(10), 2129-2137. <https://doi.org/10.1007/s11269-009-9542-y>
- [27] Basinger, M., Montalto, F., & Lall, U. (2010). A rainwater harvesting system reliability model based on nonparametric stochastic rainfall generator. *Journal of Hydrology*, 392(3-4), 105-118. <https://doi.org/10.1016/j.jhydrol.2010.07.039>
- [28] Rahman, A., Keane, J., & Imteaz, M. A. (2012). Rainwater harvesting in Greater Sydney: Water savings, reliability and economic benefits. *Resources, Conservation and Recycling*, 61, 16-21. <https://doi.org/10.1016/j.resconrec.2011.12.002>
- [29] Imteaz, M. A., Ahsan, A., & Shanableh, A. (2013). Reliability analysis of rainwater tanks using daily water balance model: Variations within a large city. *Resources, Conservation and Recycling*, 77, 37-43. <https://doi.org/10.1016/j.resconrec.2013.05.006>
- [30] Bocanegra-Martínez, A., Ponce-Ortega, J. M., Nápoles-Rivera, F., Serna-González, M., Castro-Montoya, A. J., & El-Halwagi, M. M. (2014). Optimal design of rainwater collecting systems for domestic use into a residential development. *Resources, Conservation and Recycling*, 84, 44-56. <https://doi.org/10.1016/j.resconrec.2014.01.001>
- [31] García-Montoya, M., Bocanegra-Martínez, A., Nápoles-Rivera, F., Serna-González, M., Ponce-Ortega, J. M., & El-Halwagi, M. M. (2015). Simultaneous design of water reusing and rainwater harvesting systems in a residential complex. *Computers & Chemical Engineering*, 76, 104-116. <https://doi.org/10.1016/j.compchemeng.2015.02.011>
- [32] Sample, D. J., & Liu, J. (2014). Optimizing rainwater harvesting systems for the dual purposes of water supply and runoff capture. *Journal of Cleaner Production*, 75, 174-194. <https://doi.org/10.1016/j.jclepro.2014.03.075>
- [33] Emami Javanmard, M., Ghaderi, S. F., & Sangari, M. S. (2020). Integrating energy and water optimization in buildings using multi-objective mixed-integer linear programming. *Sustainable Cities and Society*, 62, 102409. <https://doi.org/10.1016/j.scs.2020.102409>
- [34] Zhang, L., Njepu, A., & Xia, X. (2021). Minimum cost solution to residential energy-water nexus through rainwater harvesting and greywater recycling. *Journal of Cleaner Production*, 298, 126742. <https://doi.org/10.1016/j.jclepro.2021.126742>
- [35] Okoye, C. O., Solyali, O., & Akıntuğ, B. (2015). Optimal sizing of storage tanks in domestic rainwater harvesting systems: A linear programming approach. *Resources, Conservation and Recycling*, 104, 131-140. <https://doi.org/10.1016/j.resconrec.2015.08.015>
- [36] Ruso, M., Akıntuğ, B., & Kentel, E. (2019). Optimum tank size for a rainwater harvesting system: Case study for Northern Cyprus. *IOP Conference Series: Earth and Environmental Science*, 297, 012026. <https://doi.org/10.1088/1755-1315/297/1/012026>

- [37] Lucas, S. A., Geary, P. M., Hardy, M. J., & Coombes, P. J. (2006). Rainwater harvesting: revealing the detail. *Water: Journal of the Australian Water Association*, 33, 89-94. Retrieved from <https://search.informit.com.au/documentSummary;dn=200709850;res=IELAPA>. ISSN: 0310-0367.
- [38] Coombes, P., & Barry, M. (2007). The effect of selection of time steps and average assumptions on the continuous simulation of rainwater harvesting strategies. *Water Science and Technology*, 55(4), 125-133. <https://doi.org/10.2166/wst.2007.102>
- [39] Ndiritu, J., Odiyo, J. O., Makungo, R., Ntuli, C., & Mwaka, B. (2011). Yield–reliability analysis for rural domestic water supply from combined rainwater harvesting and run-of-river abstraction. *Hydrological Sciences Journal*, 56(2), 238-248. <https://doi.org/10.1080/02626667.2011.555766>
- [40] Campisano, A., & Modica, C. (2015). Appropriate resolution timescale to evaluate water saving and retention potential of rainwater harvesting for toilet flushing in single houses. *Journal of Hydroinformatics*, 17(3), 331-346. <https://doi.org/10.2166/hydro.2015.022>
- [41] Zhang, S., Jing, X., Yue, T., & Wang, J. (2020). Performance assessment of rainwater harvesting systems: Influence of operating algorithm, length and temporal scale of rainfall time series. *Journal of Cleaner Production*, 253, 120044. <https://doi.org/10.1016/j.jclepro.2020.120044>
- [42] Campisano, A., & Modica, C. (2012). Optimal sizing of storage tanks for domestic rainwater harvesting in Sicily. *Resources, Conservation and Recycling*, 63, 9–16. <https://doi.org/10.1016/j.resconrec.2012.03.007>
- [43] Magliano, P. N., Murray, F., Baldi, G., Aurand, S., Páez, R. A., Harder, W., & Jobbágy, E. G. (2015). Rainwater harvesting in dry Chaco: Regional distribution and Local Water Balance. *Journal of Arid Environments*, 123, 93–102. <https://doi.org/10.1016/j.jaridenv.2015.03.012>
- [44] Notaro, V., Liuzzo, L., & Freni, G. (2016). Reliability analysis of rainwater harvesting systems in southern Italy. *Procedia Engineering*, 162, 373–380. <https://doi.org/10.1016/j.proeng.2016.11.077>
- [45] Jing, X., Zhang, S., Zhang, J., Wang, Y., Wang, Y., & Yue, T. (2018). Analysis and modelling of stormwater volume control performance of rainwater harvesting systems in four climatic zones of China. *Water Resources Management*, 32(8), 2649–2664. <https://doi.org/10.1007/s11269-018-1950-4>
- [46] Musayev, S., Burgess, E., & Mellor, J. (2018). A global performance assessment of rainwater harvesting under climate change. *Resources, Conservation and Recycling*, 132, 62–70. <https://doi.org/10.1016/j.resconrec.2018.01.023>
- [47] Ali, S., Zhang, S., & Yue, T. (2020). Environmental and economic assessment of rainwater harvesting systems under five climatic conditions of Pakistan. *Journal of Cleaner Production*, 259, 120829. <https://doi.org/10.1016/j.jclepro.2020.120829>

- [48] Preeti, P., & Rahman, A. (2021). A case study on reliability, water demand and economic analysis of rainwater harvesting in Australian Capital Cities. *Water*, 13(19), 2606. <https://doi.org/10.3390/w13192606>
- [49] Ghisi, E., Montibeller, A., & Schmidt, R. W. (2006). Potential for potable water savings by using rainwater: An analysis over 62 cities in southern Brazil. *Building and Environment*, 41(2), 204-210. <https://doi.org/10.1016/j.buildenv.2005.01.014>
- [50] Kjeldsen, T. R., & Rosbjerg, D. (2004). Choice of reliability, resilience and vulnerability estimators for risk assessments of water resources systems / Choix d'estimateurs de fiabilité, De résilience et de vulnérabilité pour les analyses de risque de systèmes de ressources en eau. *Hydrological Sciences Journal*, 49(5). <https://doi.org/10.1623/hysj.49.5.755.55136>
- [51] Hashimoto, T., Stedinger, J. R., & Loucks, D. P. (1982). Reliability, resiliency, and vulnerability criteria for Water Resource System Performance Evaluation. *Water Resources Research*, 18(1), 14–20. <https://doi.org/10.1029/wr018i001p00014>
- [52] European Standards. (2018). BS EN 16941-1:2018 - On-site non-potable water systems – Part 1: Systems for the use of rainwater. Retrieved November 07, 2020, from <https://www.en-standard.eu/bs-en-16941-1-2018-on-site-non-potable-water-systems-systems-for-the-use-of-rainwater/>
- [53] Northern Cyprus Statistical Institute. (2021). Consumer Price Index. Retrieved November 8, 2021, from <http://www.stat.gov.ct.tr/tufe-3.aspx>
- [54] Havadis Newspaper. (2017). Water tariffs. Retrieved July 25, 2020, from <https://www.havadiskibris.com/en-pahali-lefkosa-en-ucuz-akincilar/>
- [55] Elkiran, G., & Turkman, A. (2008). Water Scarcity Impacts on Northern Cyprus and Alternative Mitigation Strategies. In J. Qi & K. T. Evered (Eds.), *Environmental Problems of Central Asia and their Economic, Social and Security Impacts* (pp. 241–250). NATO Science for Peace and Security Series C: Environmental Security. Dordrecht: Springer Netherlands. https://doi.org/10.1007/978-1-4020-8960-2_17
- [56] California State Water Resources Control Board. (2011). The Clean Water Team Guidance Compendium for Watershed Monitoring and Assessment State Water Resources Control Board 5.1.3. Runoff Coefficient (C) Fact Sheet. Retrieved July 25, 2020, from https://www.waterboards.ca.gov/water_issues/programs/swamp/docs/cwt/guidance/513.pdf
- [57] Paralik Group. (2020). Main Products Cold Water Tanks. Retrieved July 25, 2020, from https://www.paralikgroup.com/water_tanks.html
- [58] Northern Cyprus Central Bank. (2021). Discount Rate. Retrieved November 8, 2021, from <http://www.kktcmerkezbankasi.org/tr/oranlar/mevduat-faiz>
- [59] Rashidi Mehrabadi, M. H., Saghafian, B., & Haghghi Fashi, F. (2013). Assessment of residential rainwater harvesting efficiency for meeting non-potable water demands in three climate conditions. *Resources, Conservation and Recycling*, 73, 86–93. <https://doi.org/10.1016/j.resconrec.2013.01.015>

- [60] Coombes, P. J., & Barry, M. E. (2009). The spatial variation of climate, household water use, and the performance of rainwater tanks across Greater Melbourne. In WSUD09 Conference. Engineers Australia. Perth.
- [61] Özdağlar, D., Benzedem, E. & Kahraman, A. M. (2006). Kompleks Su Dağıtım Şebekelerinin Genetik Algoritma ile Optimizasyonu [Optimization of Complex Water Distribution Networks with Genetic Algorithm]. *Teknik Dergi*, 17(82), 3851-3867. Retrieved from <https://dergipark.org.tr/en/pub/tekderg/issue/12775/155306>
- [62] Nachson, U., Silva, C. M., Sousa, V., Ben-Hur, M., Kurtzman, D., Netzer, L., & Livshitz, Y. (2022). New modelling approach to optimize rainwater harvesting system for non-potable uses and groundwater recharge: A case study from Israel. *Sustainable Cities and Society*, 85, 104097. <https://doi.org/10.1016/j.scs.2022.104097>
- [63] Campisano, A., Butler, D., Ward, S., Burns, M. J., Friedler, E., DeBusk, K., Fisher-Jeffes, L. N., Ghisi, E., Rahman, A., Furumai, H., & Han, M. (2017). Corrigendum to “urban rainwater harvesting systems: Research, implementation and future perspectives” [water res. 115 (2017) 195–209]. *Water Research*, 121, 386. <https://doi.org/10.1016/j.watres.2017.06.002>

Table S1 - Characteristics of the stations and the linear programming model results for each site.

Station number	Study site	Avg. annual rainfall (mm/year)	Avg. unit water cost ¹ (TL/m ³)	Optimum tank size (m ³)	Reliability ² (%)	Avg. annual water saving ³ (m ³ /year)	Resilience (10 ² × 1/day/failure event)	Vulnerability (m ³ /failure event)	Net financial benefit (TL)	Discounted payback period (year)
1	Girne	470	43.6	5.1	18	64	10.1	9.6	5,811	12.5
2	Beylerbeyi	499	43.6	5.4	19	68	11.0	8.8	6,342	12.4
3	Lefkoşa	309	45.1	3.4	13	47	8.1	12.0	3,302	16.0
4	Güzelyurt	291	36.5	2.8	12	45	7.2	13.4	2,147	17.6
5	Zümrütköy	291	36.5	2.7	12	44	7.1	13.6	2,009	18.0
6	Mağusa	346	33.6	3.5	13	47	7.8	12.5	1,115	22.7
7	Salamis	324	33.6	3.2	12	44	7.7	12.7	837	24.3
8	Lapta	554	35.1	4.3	19	69	9.9	9.9	3,729	16.4
9	Çamlıbel	469	35.1	4.0	18	65	10.1	9.6	3,346	17.0
10	Akdeniz	390	35.1	3.4	16	57	8.8	11.1	2,552	17.0
11	Lefke	320	25.8	2.5	13	47	7.6	12.7	306	27.6
12	Yeşilirmak	377	25.8	2.8	15	53	8.1	12.0	885	26.1
13	Gaziveren	278	25.8	2.3	11	42	7.0	14.0	-222	-
14	Değirmenlik	338	36.5	3.6	13	48	8.1	12.0	1,897	19.5
15	Erean	317	36.5	3.3	13	46	8.0	12.1	1,836	19.3
16	İskele	340	30.6	3.1	13	47	8.1	12.1	1,021	24.0
17	Tatlısu	511	29.0	4.5	19	68	11.1	8.8	3,451	16.5
18	Alevkaya	482	37.6	4.9	18	67	10.8	9.0	4,812	14.8
19	Mehmetçik	419	35.1	3.8	15	56	9.0	10.8	2,092	19.8
20	Çayrova	399	35.1	3.4	15	53	8.6	11.3	1,883	19.8
21	Yeni Erenköy	453	36.9	4.3	17	62	9.3	10.5	3,164	16.6
22	Ziyamet	430	36.9	4.1	16	57	9.1	10.8	2,558	17.5

Table S1 - Characteristics of the stations and the linear programming model results for each site. (Continue)

Station number	Study site	Avg. annual rainfall (mm/year)	Avg. unit water cost ¹ (TL/m ³)	Optimum tank size (m ³)	Reliability ² (%)	Avg. annual water saving ³ (m ³ /year)	Resilience (10 ³ × 1/day/failure event)	Vulnerability (m ³ /failure event)	Net financial benefit (TL)	Discounted payback period (year)
23	Vadili	301	24.6	2.1	11	38	6.4	15.2	-938	-
24	Kantara	562	26.8	4.2	20	72	10.9	8.9	2,110	19.0
25	Serdarlı	329	27.7	3.0	13	46	7.5	12.9	398	27.2
26	Geçitkale	327	32.0	3.2	13	46	7.9	12.3	1,155	22.4
27	Gönendere	331	27.7	3.0	13	46	8.1	12.1	326	27.5
28	Beyparmudu	353	36.5	3.5	13	48	7.9	12.3	2,124	19.8
29	Diplkarpaz	502	37.6	5.0	19	69	10.7	9.0	4,948	13.9
30	Esentepe	457	37.6	4.7	18	65	10.3	9.4	4,539	15.0
31	Boğaz	412	35.7	3.6	15	56	8.9	10.8	2,727	17.7
32	Alayköy	283	28.1	2.3	11	40	6.7	14.4	-418	-
33	Dörtöl	273	28.1	2.4	10	36	6.1	16.0	-847	-
	Max	562	45.1	5.4	20	72	11.1	16.0	6,342	27.6
	Min	273	24.6	2.1	10	36	6.1	8.8	-938	12.4
	Avg.	386	33.7	3.6	15	53	8.6	11.6	2,151	19.2

⁺ Bold rows represent the locations where RWHSs are identified as financially infeasible.

¹ Average values are calculated using the average inflation rate from 2005 to 2021 for the simulation duration by assuming that a four-person family's average monthly domestic water consumption is 31 m³ (i.e., 1 m³ per day).

² Ratio of the rainwater supply to the water demand throughout the simulation period.

³ Per single house. This is the amount of water supplied from the RWHS instead of the MWSN in a year.

Spatial Prediction of Groundwater Potential of Upper Tigris Basin Mapping in Türkiye with GIS-Based Multicriteria Decision Making (MCDM) Method

Recep ÇELİK¹



ABSTRACT

The Upper Tigris region in the Middle East is in Turkey and this study shows it to be an area with significant water resources that enable agricultural activities in the region. Since the GAP irrigation project, yet to be completed, there is an extensive use of groundwater for irrigation. This situation threatens the groundwater potential of the basin. Therefore, determination of groundwater potential should be evaluated properly instead of relying assessment of the groundwater potential of the region with observation wells, which is a more costly method. In this study, the groundwater potential of the basin was determined by the GIS-based Multi-Criteria Decision Making (MCDM) method; the GIS-based-AHP method is used for identifying the groundwater potential zones of the Upper Tigris Basin as an alternative to expensive and time-consuming method of well drilling. There are 8 key criteria considered; Geomorphology (GM), Geology(G), Line Density (LD), Slope (SL), Drainage Density (DD), Land Use (LU), Rainfall (R), and Soil Type (ST) and the individual weight of each criterion was evaluated by the AHP technique and utilized by the “Spatial Analysis Overlay Weighted Method” obtaining the “Groundwater Potential Index (GWPI)”. The GWPI values obtained is used to classify the Upper Tigris Basin into five categories as follows: 319 km² of the basin has very poor potential (3.8%); 2217 km² has poor potential (26.7%); 2800 km² has moderate potential (33.7%); 2200 km² has good potential (26.5%); and finally, 763 km² has very good potential (9.2%).

Keywords: Diyarbakır basin, groundwater potential, the AHP Multi-Criteria Decision Making (MCDM) Method, GIS.

1. INTRODUCTION

The Upper Tigris Basin is significant for surface water potential. However, due to the incomplete projects in the basin, groundwater is widely used as an alternative irrigation method (Çelik 2015). The advantage of the groundwater compared to surface water is the

Note:

- This paper was received on June 10, 2023 and accepted for publication by the Editorial Board on April 5, 2024.
- Discussions on this paper will be accepted by November 30, 2024.
- <https://doi.org/10.14800/tjce.1358155>

1 Dicle University, Department of Civil Engineering, Diyarbakır, Türkiye
recep.celik@dicle.edu.tr - <https://orcid.org/0000-0002-0739-6146>

fact that the risk of contamination for the groundwater is substantially lower than that for the surface water. In this regard, the groundwater potential of the basin must be figured out. In partially arid zones, when surface water reaches to minimum flow level, groundwater is also a significant alternative for agriculture and irrigation and also for other intended uses (Çelik 2015).

Determination of groundwater potentials by wells is not always economically feasible. Under these circumstances, among several other methods, GIS and MCDM methods have been properly and successfully employed (Rahman et al 2012; Nag et al., 2012; Lee et al., 2012; Pradhan 2013; Feizizadeh et al., 2014) to determine aquifer parameters and their impacts on groundwater sources and supplies.

Multi-Criteria Decision Making (MCDM) techniques, which requires at least two criteria and two alternatives (Diakoulaki et al., 1995), have been utilized successfully for the solution of similar problems in various areas (Makropoulos and Butler, 2006; Mendoza and Martins, 2006; Karnatak et al., 2007; Greene et al., 2011). Since relative importance is attached to each variable based on qualitative and quantitative criteria, not only the numerical data but also the previous experience of expert users is important (Triantaphyllou and Sanchez, 1997; Malczewski, 1999; Ho and Dey, 2010). For the assignment of the relative importance, among many methods available, the most common alternative is the Analytical Hierarchical Method (AHP) method (Saaty, 1980, 1989, 2000). It has been in use for the selection of the suitable area by counting the co-efficiency rates of the comparative importance of multiple criteria in relation with each other (Abdalla, 2012) and recharges assessment (Zaidi et al., 2015; Senanayake et al., 2016; Hermann et al., 2016, Verma & Patel, 2021). The AHP -MCDM techniques have become very common in positional planning and management. Comparative studies were conducted in a number of research studies through multivariate statistical analyses with GIS methods (Althuwaynee et al., 2014; Haghizadeh et al., 2017; Çelik, 2019; Doke et al, 2021). Furthermore, similar works were also conducted by the fuzzy-AHP method in some of the above-mentioned research activities (Nobre et al., 2007; Iqbal et al., 2015; Mallick et al., 2019; Mahammad & Islam, 2021).

Diyarbakır Basin is a sub-basin of the upper Tigris basin known for its relatively rich surface water potential. Since irrigation projects of the GAP Project has not yet been completed in the basin, agricultural activities along the riverbank are based on surface water consumption and in other places, water is obtained from the groundwater storages through the wells. Thus, it is necessary to figure out the quality and quantity potential of the groundwater in this region. This study aims to define suitable maps of the upper Tigris sub-basin groundwater potential zones owing to the GIS-based MCDM method. The borders of the basin are marked using the ArcMap Spatial Analysis based on Dem maps. There are eight key parameters considered; Geomorphology (GM), Geology (G), Drainage Density (DD), Line Density (LD), Land Use (LU), Slope (SL), Rainfall (R), and Soil Type (ST). Weights of all criteria are determined with the AHP technique. The ultimate results were compared with the records of the 61 wells drilled within the basin. After comparing the well log data with the ultimate map studies, the results are consistent at 80% accuracy.

2. MATERIALS AND METHODS

2.1. Study Area

The total length of the Tigris River is 1750 km, and only 500 km flows within Turkish borders (Isaev and Mikhailova, 2009). It arises from the joint point of the Hazar Baba Mountain (2290 m) and Hazar Lake in the southeast of the Elazığ province. Its drainage area is about 10550 km², starting from the upstream of the Tigris River and covering Batman in the west and the northern parts of Mardin Savur region in the south (Figure 1).

Upper Tigris basin is located between eastern longitudes at 40 ° -44° and northern latitudes at 37 ° -55°, around the Diyarbakır province. North of this basin is surrounded by mountains (GAP Development Plan 2002).

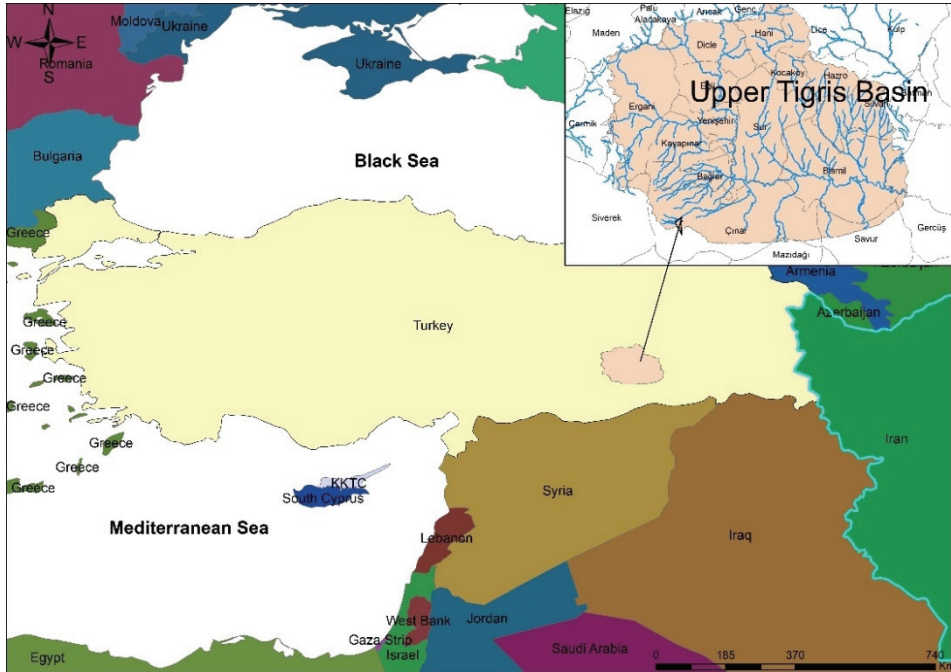


Figure 1 - Upper Tigris Basin location map

2.2. Methodology

As mentioned before, there are eight parameters taken into consideration; these are Geomorphology (GM), Land Use (LU), Geology (G), Line Density (LD), Drainage Density (DD), Slope(S), Rainfall (R), and Soil Type (ST). Each parameter weight is assessed via the AHP technique.

Initially, DEM (Digital Elevation Model) maps are obtained from General Directorate of Spatial Planning's M43, M44, M45, M46's layouts where 1/100 000 topographic maps of the region (mpgm.csb.gov.tr) were digitized using (35 × 35) m² resolution. With these DEM

data; slope, geomorphologic and drainage density maps are produced via the Spatial Analysis and Arc Hydro extensions of the Arc GIS 10.2.1 program.

The necessary information about the active and energetic fault lines, which are published both by the General Directorate of Mineral Research and Exploration (MTA) (Emre et al., 2013) and on its website online data system, are digitized and turned into kml format and the fault is converted to shp. format by the Data Interoperability extension. Land use is obtained in Erdas image format from Global Land Cover Facility site and converted in accordance with the CORINE method. Average annual rainfall values between 1971-2017 are taken from the Turkish State Meteorology website, and the precipitation maps of the entire region are obtained by using the ARC GIS Inverse Distance Weight (IDW) method. Moreover, soil type is obtained by processing the data from Özden (2001) and the official website of the Ministry of Agriculture. The study flow chart is shown in Figure 2.

Firstly, all criteria maps are converted to raster maps, and then they are reclassified via spatial analyses “reclassification” modules considering all sub-ranks as shown in Table 4. All thematic maps are then reclassified in accordance with the weight ratio determined via the AHP method (Tables 1 and 2). Ultimately, the Groundwater Potential Index (GWPI) is constructed considering the relative weights of each parameter by using the Overlay Sum method.

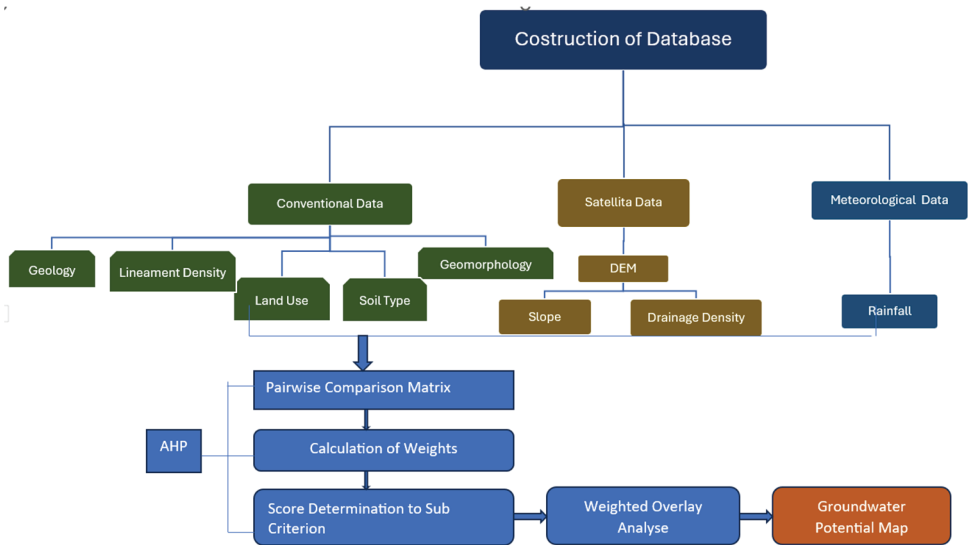


Figure 2 - The study methodology flow chart

2.2.1. The AHP Methods

The AHP is the common method of MCDA, which is set on three principles: extrication, relative decision, and integration the preferences (Saaty, 2000). In the AHP method, all quantitative and qualitative factors affecting the decision process are determined by

consulting the opinions of experts on this subject. Afterward, as a result of the information obtained, a hierarchical structure is created by determining the purpose, criteria and alternatives. AHP is comprised of four stages as follows:

- **The First Stage:** The objective, criteria, and alternatives of the problem are determined. The hierarchical Structure is formed (Table 1).

Table 1 - All criteria AHP Comparison Matrix

	GM	G	LD	SL	R	ST	DD	LU
GM	1.00	1.00	1.40	0.78	1.00	1.17	1.40	1.17
G	1.00	1.00	1.40	0.78	1.00	1.17	1.40	1.17
LD	0.71	0.71	1.00	0.56	0.71	0.83	1.00	0.83
SL	1.29	1.29	1.80	1.00	1.29	1.50	1.80	1.50
R	1.00	1.00	1.40	0.78	1.00	1.17	1.40	1.17
ST	0.86	0.86	1.20	0.67	0.86	1.00	1.20	1.00
DD	0.71	0.71	1.00	0.56	0.71	0.83	1.00	0.83
LU	0.86	0.86	1.20	0.67	0.86	1.00	1.20	1.00

GM: Geomorphology, G: Geology, LD: Line Density, SL: Slope, DD: Drainage Density, LU: Land Use, R: Rainfall, ST: Soil Type

- **The Second Stage:** At this stage, the comparison of the relative weights of each criterion with one another and alternative is performed. The comparisons demonstrate which criterion is more significant and are managed according to the 1-9 scale (Table 2) determined by Saaty (2000). In this study, the scores of all the main and sub-criteria are shown in Table 4.

Table 2 - Pairwise comparison scale

scale	• Explain
1	• Equal
3	• Slightly superior
5	• Much superior
7	• too much superior
9	• Absolute superiority
2,4,6,8	• Intermediate compromise values

- **The Third Stage:** The vector of the weights (W) is determined through the priority vectors and comparison matrices (Table 3). Initially, the paired comparison matrix is normalized through $A \cdot w = \lambda_{max}$. Subsequently, the weights are determined. The normalization is determined via division of all a_{ij} matrix elements by the column total.

Weight calculation:

$$W_i = \sum_{i=1}^n a_{ij} / n \tag{1}$$

Table 3 - AHP Normalized Matrix and Significance Weighting Values of Using Parameters

	GM	G	LD	SL	R	S	DD	LU	W
GM	0.11	0.13	0.13	0.13	0.13	0.13	0.13	0.13	0.13
G	0.11	0.13	0.13	0.13	0.13	0.13	0.13	0.13	0.13
LD	0.08	0.10	0.10	0.10	0.10	0.10	0.10	0.10	0.09
SL	0.15	0.17	0.17	0.17	0.17	0.17	0.17	0.17	0.17
R	0.11	0.13	0.13	0.13	0.13	0.13	0.13	0.13	0.13
S	0.08	0.12	0.12	0.12	0.12	0.12	0.12	0.12	0.11
DD	0.15	0.10	0.10	0.10	0.10	0.10	0.10	0.10	0.11
LU	0.20	0.12	0.12	0.12	0.12	0.12	0.12	0.12	0.14

λ_{max} : 8.23; CI: 0.03; CR: 0.023<0.1: all are acceptable (Saaty, 2000).

- The Fourth Stage:** The calculation of consistency ratio and the CR coefficient are conducted after the calculation of consistency index (CI). In the paired comparison of the decision matrices, it is accepted as consistent if CR is lower than 10%. The primary matrix of topics and their linked sub-themes have been reviewed in a methodical manner via AHP branch of information. The coherence ratio of precedence matrix can be made feasible with the aid of this technique (Saaty, 2000).

The AHP table (Table 2) indicates the highest weight criteria is the Slope with 17%, followed by Land Use 14%, Rainfall, Geology and Geomorphology 13%. The lowest weight parameter is Lineament Density with 9%.

3. RESULTS

In order to define the potential groundwater recharge zones in any basin, the primary parameters are mapped in Figure 3 as: Slope (S), Lineament Density (LD), Geology (G), Geomorphology (GM), Land Use (LU), Soil Type, Rainfall (R) and they are summarized in Table 4. The scores of the criteria were determined by examining studies in the literature (Adiat et al., 2012; Althuwaynee et al., 2014; Doke et al., 2021, etc.) and considering the effect rates of the parameters on groundwater formation. In the table, areas with high groundwater potential are ranked with high ranking. For example, for the slope parameter, % 0-2 is ranked as 9 because it is high in terms of groundwater potential. Finally, Groundwater potential index (GWPI) is mapped in Figure 4. Both series of maps depicted in Figures 3 and 4 are constructed by the author based on scientific data and findings.

3.1. Geomorphology

Geomorphology represents an important criterion describing the plain, mountainous, hilly and alluvium districts of the topographic map. It is a criterion showing the gathering of groundwater potential in the basin area. Most effective areas are flatness (30.1 %), plains (27.7%) and hills (27.3 %). The alluvium portion is 9.4% while the rate of the mountains is 5.5%.

3.2. Geology

Geologic features are considered significant for determining the groundwater potential (Krishnamurthy et al., 2010). Besides, the geological structure is important for the location of an aquifer. Limestone and basalt structures are good aquifers. On the other hand, alluviums in the streambeds play an important role as well (Gale et al., 2002; Kresic 2010;). The basin is comprised of particularly Terrestrial clastic (35.1 %), Basalt (23.2 %), and Neritic limestone (16.7%).

3.3. Slope

The main source of the groundwater potential is the infiltration capacity of the rainfall. However, this infiltration is mostly occurred with high permeability soil types and low slope condition. The slope of the terrain has a very high value effect. Infiltration is higher where the slope is small since the surface flow is slow, whereas underground water supply is less where the slope is high since the surface flow is higher (Reid & Iverson, 1992). As shown in Table 4, slope of the significant portion of the land varies between 0-4 %. As it moves towards the north, the slope is increasing.

3.4. Land Use

Land Use is also a major parameter for groundwater capacity assessments (Eulenstein et al.,2016). Due to the urbanization, infiltration is scarce and thus the runoff rate is high. Wetlands are considered to be at the highest assessment level and, there is a high rate of infiltration in rivers and alluvial deposits. Another rating is followed up by wet agricultural areas. A major part of the water leaks into subsurface in the irrigation zones. Similarly, the planted zones have a high rate of infiltration, since surface runoff is mitigated by plantations. Rate and usage classification of land use are shown in Table 4.

3.5. Rainfall

Precipitation is the main source of groundwater formation. A portion of the precipitation runoff on surface feeds the surface water sources, and another portion infiltrates to underground and forms the groundwater reservoirs (Jan et al.,2007; Wang et al., 2015). In this study, the annual average precipitation data are used between 1975 and 2017 taken from the General Directorate of Meteorology. Through the interpolation of these data and ArcMap

Spatial Analysis IDW method, the average rainfall map of the region is obtained. It is classified in Table 4 and ranking coefficients are determined accordingly.

3.6. Soil

Soil classes are obtained from the class maps of the Ministry of Agriculture. Soil type class distribution of basin is revealed in Table 4. Soil type is a particularly essential criterion for groundwater because of its infiltration capacity for groundwater recharge to aquifers. The capacity of coarse-grained soils is high in the infiltration such as gravelly, sandy, and alluvial soils, this has a high-grade weight in the groundwater potential formation. Besides, soils of clay, sand or silt have low infiltration capacity. Thus, such soil classes are at a lower assessment class.

3.7. Drainage Density

Drainage Density (DD) is one of the criteria affecting the groundwater potential index (GWPI). In river channels infiltration is less in the regions with high drainage density (Tucker and Bras, 1992), whereas the infiltration gets at a higher proportion due to the surface flow; slow regions with low drainage density. Therefore, the output rate parameter is considered as a higher rank with low drainage density. Drainage density is obtained from DEM maps, with the practical help of GIS Arc-Hydro tool, in the order of, fill sinks – flow direction – flow accumulation – stream segmentation – stream definition are acquired by the accurate classification of the rivers through the hierarchical process. Drainage density (DD) is expressed as follows:

$$DD = L/A \quad (2)$$

where L is the total drainage length and A is area (Tarboton, 1992).

3.8. Lineament Density

The lineament density (LD) indicates an important geological feature for groundwater recharge (Magowe and Carr, 1999). The cracked areas generate discontinuities between the areas and cause groundwater recharge to aquifers in a short period of time. The areas with high fault intensity have a high rate of effect in terms of recharge and the areas with low fault intensity have a low rate of effect. The LD is calculated as follows (Mandal et al., 2016);

$$LD = \sum_{i=1}^n L_i/A \quad (3)$$

where L_i is lineaments length, and i indicates the number of lineaments and A is basin drainage area.

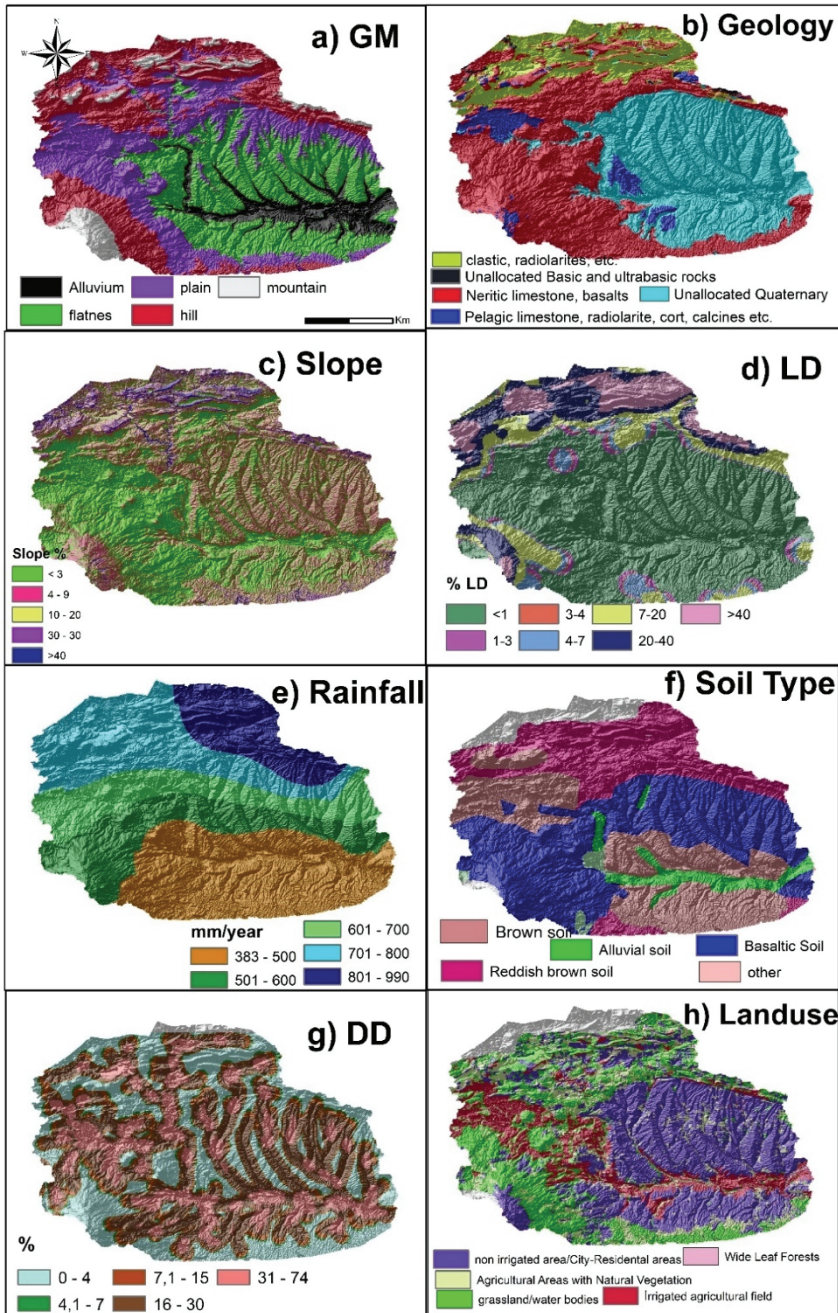


Figure 3 - Main parameters effect on Groundwater Potential Recharge Map (GM: Geomorphology, G: Geology, LD: Line Density, SL: Slope, DD: Drainage Density, LU: Land Use, R: Rainfall, ST: Soil Type)

Table 4 - AHP Assessment Sub-Properties of Parameters Summarized Table

Feature Rank	Assigned Normalized Weight	Sub-Feature	Area Coverage (%)	Rank
7	Geomorphology map	Alluvium	9.4	9
		flatness	30.1	7
		plain	27.7	6
		hill	27.3	3
		mountain	5.5	1
7	Geology	Neritic limestone	16.7	7
		Terrestrial clastic	35.1	9
		Magmatic and Volcanic Rocks	4.1	6
		Unallocated Quaternary	3.6	9
		Pelagic limestones, clastic, radiolarites, etc.	0.6	5
		Basalt	23.2	6
		Soils and carbonates	11.4	5
		Unallocated Basic and ultrabasic rocks	0.3	5
		Pyroclastic rocks	0.4	5
		Unallocated terrestrial clastic	4.0	5
Pelagic limestone, radiolarite, cort, calcines etc.	0.7	6		
5	Lineament Density (km/km ²)	0-1	61.7	1
		1-3	2.4	2
		3-4	1.2	3
		4-7	4.5	5
		7-20	11.0	7
		20-40	11.2	8
		>40	8.1	9
9	Slope (%)	0-2	33.5	9
		2-4	21.4	7
		4-8	21.2	5
		8-15	14.7	3
		>15	9.2	1
7	Rainfall (mm/year)	383-500	32.5	4
		500-600	17.7	5
		600-700	8.7	6
		700-800	10.4	7
		800-900	19.3	8
		900-985	11.4	9

6	Soil	Aluvial soil	1.3	9
		Basaltic soil	39.9	8
		other	5.3	7
		Brown Forestry soil	0.1	6
		Brown Soil	24.0	5
		reddish brown soil	29.5	5
5	Drainage Density (km /km ²)	0-4	0.0	9
		4-7	0.0	7
		7-15	0.0	5
		15-30	0.0	3
		30-50	0.0	1
6	Land use	grassland	19.15	7
		Rocks	1.63	2
		Discrete Rural Building	0.68	5
		Agricultural Areas with Natural Vegetation	9.91	7
		Irrigated Area	13.63	8
		Non-irrigated agricultural area	43.16	5
		Natural Meadows	6.11	7
		Wide Leaf Forests	4.07	6
		Continuous City Structure	0.06	3
		Water bodies	1.01	9
		coastal, sandy	0.10	9
		Industrial or Commercial Areas	0.13	2
		marsh	0.12	9
Construction sites/airport	0.12	3		

3.9. Groundwater Potential Index (GWPI)

GWPI represent a dimensionless magnitude, which implies the groundwater potential in a region. It is obtained through the weights of various parameters. It provides information about groundwater potential in various locations (Rahmati et al., 2015; Shektar and Pandey, 2015). It is calculated via the AHP method as shown below (Lee et al., 2012, Rahmati et al., 2015, Çelik 2019):

$$GWPI = SL_r \cdot SL_w + LD_r \cdot LD_w + G_r \cdot G_w + GM_r \cdot GM_w + LU_r \cdot LU_w + ST_r \cdot ST_w + R_r \cdot R_w + DD_r \cdot DD_w \quad (4)$$

where SL is the slope, LD is the lineament density, G is geology, GM is geomorphology, LU represents the land use, ST is the soil type, R is the rainfall, and DD is the drainage density. In addition, the subscripts “r” and “w” refer to the rating and weight of the parameter, respectively. The reclassification of GWPI index is given in Figure 4.

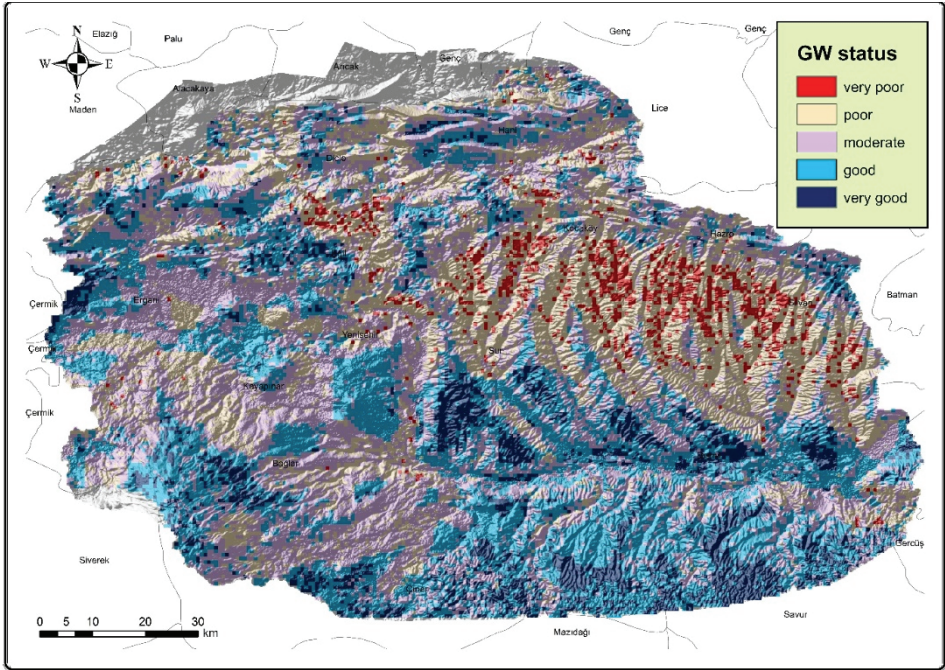


Figure 4 - Upper Tigris Basin groundwater potential recharge map

3.10. Determination of Groundwater Potential Zones

The ranking assigned for all thematic maps and a comprehensive description of their corresponding sub-features are shown in Table 4. In order to produce the GWPZ map efficiently, the sum of the weights criteria is used as determined by the AHP method. In Figure 4, the groundwater potential index of the basin is divided into five classes; very good potential, good potential, moderate potential, poor potential and very poor potential.

Table 5 - Upper Tigris Basin Groundwater Potential Status

Status	Percentage	Area (km ²)
very poor	3.8%	319
poor	26.7%	2217
moderate	33.7%	2800
good	26.5%	2200
very good	9.2%	763

Table 5 summarises the basin groundwater potential status; 319 km² (3.8%) portion of the basin is rated as very poor potential, 2217 km² (26.7%) portion of the basin is poor potential; 2800 km² (33.7%) portion of the basin is moderate potential; 2200 km² (26.5%) portion of

the basin as good potential; 763 km² (9.2%) as very good potential. There is a major part of the basin with a moderate groundwater potential. In the northern part of the basin, GWPI index has a very poor potential. This is due to both the aquifer properties and the steep slopes in these regions.

3.11. Validation and Sensitivity Analysis

The results of this study are compared with 61 well-records over the basin in Table 7. Classification of the Yield Values are performed as follows: 0.00-2.00 as “very low”; 2.01-4.00 as “low”; 4.01-8.00 as “moderate”; 8.01-15.00 as “good”; and 15.01 and above as “very good”. Each of the “Well GW Status” and “Obtained GWPI Status” are assigned 5 ranks in an increasing order as “very low”, “low”, “moderate”, “good” and “very good”. The evaluation is performed on the results compiled in Table 7 by assigning the corresponding “comparison score” from among a 5 point-scale, where the highest and lowest scores assigned are 5 and 1 respectively, as follows:

- If the Well GW Status and the Obtained GWPI Status match exactly, i.e., if they differ by no rank order, the comparison score assigned is 5 as shown in lines 1 through 5 in Table 6.
- If the Well GW Status and the Obtained GWPI Status differ by 1 rank order, the comparison score assigned is 4 as shown in lines 6 through 13 in Table 6.
- If the Well GW Status and the Obtained GWPI Status differ by 2 rank orders, the comparison score assigned is 3 as shown in lines 14 through 19 in Table 6.
- If the Well GW Status and the Obtained GWPI Status differ by 3 rank orders, the comparison score assigned is 2 as shown in lines 20 through 23 in Table 6.
- If the Well GW Status and the Obtained GWPI Status differ by 4 rank orders, the comparison score assigned is 1 as shown in lines 24 and 25 in Table 6.

After that, all comparison scores (the blue entries in Table 7) are summed up and the result is divided by the perfect matching scoring which is $61 \times 5 = 305$, i.e., the sum of the comparison scores for the hypothetical case when all “Well GW Status” and “Obtained GWPI Status” pairs match perfectly.

In this case, 80% validation rate is obtained for the 61 wells analysed. In this situation, GWPI index shows 100% compliance with the data from 23 wells, 80% compliance with the data from 19 wells and 60% compliance with the data from 15.

Table 6 - Comparison Score Assignment

Line Number	Well GW Status	Obtained GWPI Status	Rank Difference	Comparison Score
1	very low	very low	0	5
2	low	low	0	5
3	moderate	moderate	0	5
4	good	good	0	5

5	very good	very good	0	5
6	very low	low	1	4
7	low	very low	1	4
8	low	moderate	1	4
9	moderate	low	1	4
10	moderate	good	1	4
11	good	moderate	1	4
12	good	very good	1	4
13	very good	good	1	4
14	very low	moderate	2	3
15	low	good	2	3
16	moderate	very low	2	3
17	moderate	very good	2	3
18	good	low	2	3
19	very good	moderate	2	3
20	very low	good	3	2
21	low	very good	3	2
22	good	very low	3	2
23	very good	low	3	2
24	very low	very good	4	1
25	very good	very low	4	1

Table 7 - a Upper Tigris Basin Validation Well Information with GWPI results

Well Number	Y	X	Yield (sec/l)	Well GW Status	Obtained GWPI Status	Comparison Score
1	4234976	594798	1.00	very low	very low	5
2	4240605	641220	5.00	moderate	moderate	5
3	4170332	618940	60.00	very good	very good	5
4	4248630	619128	29.00	very good	good	4
5	4252657	627148	3.60	low	low	5
6	4185994	618632	18.00	very good	moderate	3
7	4175722	651710	28.00	very good	good	4
8	4254428	611381	7.00	moderate	very good	3
9	4187953	640152	10.00	good	moderate	4
10	4190264	649502	26.00	very good	very good	5
11	4251104	596420	5.00	moderate	moderate	5
12	4234587	567662	1.00	very low	good	2
13	4233371	650890	1.00	very low	very good	1
14	4162753	608983	17.00	very good	good	4

15	4175743	659607	15.00	good	good	5
16	4173275	666873	24.00	very good	moderate	3
17	4234982	659234	1.00	very low	moderate	3
18	4220954	569040	36.00	very good	moderate	3
19	4170605	624752	47.00	very good	very good	5
20	4223240	580608	2.00	low	low	5
21	4203377	667978	20.00	very good	low	2
22	4191198	633005	24.00	very good	good	4
23	4238558	630703	4.00	moderate	good	4
24	4174932	635793	38.00	very good	good	4
25	4181275	653577	5.00	moderate	moderate	5
26	4193562	607319	30.00	very good	moderate	3
27	4237944	560898	1.00	very low	moderate	3
28	4165449	640104	23.00	very good	good	4
29	4174411	612403	40.00	very good	moderate	3
30	4177651	669466	11.00	good	good	5
31	4181012	641897	40.00	very good	good	4
32	4236705	583757	3.00	low	good	3
33	4179984	605814	35.00	very good	moderate	3
34	4182577	632206	30.00	very good	good	4
35	4173824	642624	22.00	very good	good	4
36	4181645	625847	34.00	very good	very good	5
37	4174894	617440	14.00	good	good	5
38	4189429	623372	15.00	good	good	5
39	4185502	598971	3.00	low	moderate	4
40	4222567	621532	2.10	low	low	5
41	4231481	626618	3.30	low	very low	4
42	4217025	648300	3.00	low	low	5
43	4184591	608795	2.00	low	moderate	4
44	4222736	641586	1.60	very low	very low	5
45	4228009	599394	3.50	low	good	3
46	4236613	621107	2.80	low	very good	2
47	4177644	598191	4.00	moderate	moderate	5
48	4221388	603826	10.00	good	low	3
49	4214235	614259	1.30	very low	moderate	3
50	4220908	635885	3.00	low	low	5
51	4193657	615252	4.00	moderate	very good	3
52	4196175	591900	5.00	moderate	good	4
53	4208575	574553	2.00	low	low	5

54	4204265	606998	6.00	moderate	moderate	5
55	4202196	572525	5.00	moderate	moderate	5
56	4217281	598313	3.00	low	good	3
57	4203855	618848	20.00	very good	very good	5
58	4230751	613900	3.00	low	moderate	4
59	4210382	631105	5.00	moderate	low	4
60	4201907	587760	10.00	good	moderate	4
61	4199178	611842	2.00	low	moderate	4

GWPI: Groundwater Potential Index; Validation Rate: $243/(5*63) = 0.80 = 80\%$ accuracy

4. DISCUSSION

In order to determine the groundwater potential of a region in the most accurate way, it is necessary to drill observation wells in the fields. However, this method is uneconomic and takes a long time in large basins. However, taking into account the RS data and the parameters affecting the groundwater with their weight, methods such as GIS based AHP methods give an idea about a basin's groundwater potential in a shorter time with great accuracy. In this study, it has been demonstrated that the use of this method is a viable one.

On the other hand, at a macro-level analysis performed over an expanded area the groundwater potential map is a significant tool that can be useful in basin-based hydrological studies and possibly for groundwater well digging operations in the future. As an added benefit of this study, for micro planning, more reliable assessment can also be conducted with the help of similar criteria and lower-scale maps. Especially geological factors, slope, geomorphological factors and the potential effects of the land use should be taken into consideration.

Finally, aquifer region risk and pollution analyses should be carried out regularly due to agricultural and other anthropological activities, and sustainable groundwater management should be provided properly at the local Governor and Municipality levels. Urbanization areas and their development axis and structures such as urban solid waste facilities should be projected by taking into account groundwater maps in the future.

5. CONCLUSION

The Analytical Hierarchical Process (AHP) integrated with Geospatial technology is presented as an accurate method for finding out the groundwater potential of a region as demonstrated in this study. Groundwater potential maps were obtained with an 80% accuracy for the North (Upper) Tigris Basin by utilizing this method. Moreover, It was determined that 3.8% of the basin area has very poor potential, 26.7% has poor potential, 33.7% has moderate potential, 26.5% has good potential, and 9.2 % of the basin shows very good potential.

Approximately 36% of the basin has good potential to very good potential. These key areas are predominantly in the plain part of the basin and are close to the Tigris River in Diyarbakır-Sur, Çınar, Bismil and Batman regions. In places with good and very good water potential, there are sufficient water resources for agricultural irrigation as well. Provided that the

amount of groundwater recharge is taken into account, groundwater can be used for agricultural irrigation in these regions. Especially, north-northeast areas of the basin seem to have poor potential in terms of the groundwater. The reason for this is that the region has hilly and mountainous geomorphological characteristics, and the water supply is low. However, there is enough groundwater potential in these regions for domestic use/drinking water and small-scale agricultural irrigation.

The western and south-western parts of the basin generally have a moderate potential. There are also hills in these areas. However, the slope is not as high as it is in the northern regions. There is suitable groundwater potential in these regions both domestic use and moderate scale agricultural irrigation.

6. SUGGESTIONS FOR FURTHER STUDIES

GIS based AHP methods give an idea about a basin's groundwater potential in a shorter time with great accuracy instead of the time consuming and very expensive method of well drilling. The use of GIS based AHP methods, based on the implementation on the Upper Tigris Basin in Turkey as demonstrated in this study, seem to be a good alternative method to determine groundwater potential.

We suggest that this method should be used at different geographies both within and outside Turkey. The reason is simple; due to global warming, water is quickly becoming a rare resource for consumption as well as agriculture. Having groundwater potential maps readily constructed at local and national administrations, may prove to be valuable at times of mild or severe draught, in order to determine the water resources that can be tapped into.

References

- [1] Abdalla, F.: Mapping of groundwater prospective zones using remote sensing and GIS techniques: a case study from the Central Eastern Desert, Egypt. *Journal of African Earth Sciences*, 70, 8-17, DOI: 10.1016/j.jafrearsci.2012.05.003, 2012.
- [2] Adiat, K. A. N., Nawawi, M. N. M., & Abdullah, K.: Assessing the accuracy of GIS-based elementary multicriteria decision analysis as a spatial prediction tool—a case of predicting potential zones of sustainable groundwater resources. *Journal of Hydrology*, 440, 75-89, DOI: 10.1016/j.jhydrol.2012.03.028, 2012.
- [3] Akbaş, B., Akdeniz, N., Aksay, A., Altun, İ., Balcı, V., Bilginer, E., Bilgiç, T., Duru, M., Ercan, T., Gedik, İ., Günay, Y., Güven, İ.H., Hakyemez, H. Y., Konak, N., Papak, İ., Pehlivan, Ş., Sevin, M., Şenel, M., Tarhan, N., Turhan, N., Türkecan, A., Ulu, Ü., Uğuz, M.F., Yurtsever, A. and etc.: *Türkiye Jeoloji Haritası Maden Tetkik ve Arama Genel Müdürlüğü Yayını* Ankara, 2002.
- [4] Althuwaynee, O. F., Pradhan, B., Park, H. J., & Lee, J. H.: A novel ensemble bivariate statistical evidential belief function with knowledge-based analytical hierarchy process and multivariate statistical logistic regression for landslide susceptibility mapping. *Catena*, 114, 21-36, DOI: 10.1016/j.catena.2013.10.011, 2014.

- [5] Çelik, R.: Temporal changes in the groundwater level in the Upper Tigris Basin, Turkey, determined by a GIS technique. *Journal of African Earth Sciences*, 107, 134-143, DOI: 10.1016/j.jafrearsci.2015.03.004, 2015.
- [6] Çelik R. Evaluation of Groundwater Potential by GIS-Based Multicriteria Decision Making as a Spatial Prediction Tool: Case Study in the Tigris River Batman-Hasankeyf Sub-Basin, Turkey. *Water*. 2019; 11(12):2630. <https://doi.org/10.3390/w11122630>
- [7] Doke, A. B., Zolekar, R. B., Patel, H., & Das, S. (2021). Geospatial mapping of groundwater potential zones using multi-criteria decision-making AHP approach in a hardrock basaltic terrain in India. *Ecological Indicators*, 127, 107685.
- [8] Diakoulaki, D., Mavrotas, G., & Papayannakis, L. (1995). Determining objective weights in multiple criteria problems: The critic method. *Computers & Operations Research*, 22(7), 763-770.
- [9] Eulenstein, F., Saparov, A., Lukin, S., Sheudshen, A. K., Mayer, W. H., Dannowski, R., ... & Cremer, N. (2016). Assessing and controlling land use impacts on groundwater quality. Novel methods for monitoring and managing land and water resources in Siberia, 635-665.
- [10] Feizizadeh, B., Jankowski, P., & Blaschke, T.: A GIS based spatially-explicit sensitivity and uncertainty analysis approach formula multi-criteria decision analysis. *Computers & geosciences*, 64, 81-95, DOI: 10.1016/j.cageo.2013.11.009, 2014.
- [11] Gale, I., Neumann, I., Calow, R., & Moench, D. M. (2002). The effectiveness of Artificial Recharge of groundwater: a review.
- [12] Global Land Cover Facility (GLCF): <http://glcf.umd.edu/data>, last access: 25 October 2018.
- [13] Greene R., Devillers R., Luther J. E., and Eddy B. G.: GIS-based multiple-criteria decision analysis, *Geography Compass*, 5/6, 412-432, DOI: 10.1111/j.1749-8198.2011.00431.x, 2011.
- [14] Haghizadeh, A., Moghaddam, D. D., & Pourghasemi, H. R.: GIS-based bivariate statistical techniques for groundwater potential analysis (an example of Iran). *Journal of Earth System Science*, 126(8), 109, DOI: 10.1007/s12040-017-0888-x, 2017.
- [15] Herrmann, F., Baghdadi, N., Blaschek, M., Deidda, R., Duttman, R., La Jeunesse, I., ... & Wendland, F.: Simulation of future groundwater recharge using a climate model ensemble and SAR-image based soil parameter distributions—A case study in an intensively-used Mediterranean catchment. *Science of the Total Environment*, 543, 889-905, DOI: 10.1016/j.scitotenv.2015.07.036, 2016.
- [16] Ho W., Xu X. and Dey P.K.: Multi-criteria decision making approaches for supplier valuation and selection: a literature review, *European Journal of Operational Research*, 202/1, 16-24, DOI: 10.1016/j.ejor.2009.05.009, 2010.

- [17] Iqbal, J., Gorai, A. K., Katpatal, Y. B., & Pathak, G.: Development of GIS-based fuzzy pattern recognition model (modified DRASTIC model) for groundwater vulnerability to pollution assessment. *International journal of environmental science and technology*, 12(10), 3161-3174, DOI: 10.1007/s13762-014-0693-x, 2015.
- [18] Isaev, V.A.; Mikhailova, M.V.: "The hydrology, evolution, and hydrological regime of the mouth area of the Shatt al-Arab River". *Water Resources*. 36 (4): 380–395, DOI: 10.1134/S0097807809040022, 2009.
- [19] Islamic encyclopedia: <https://islamansiklopedisi.org.tr/dicle>, last access: 25 January 2019
- [20] Jan, C. D., Chen, T. H., & Lo, W. C. (2007). Effect of rainfall intensity and distribution on groundwater level fluctuations. *Journal of hydrology*, 332(3-4), 348-360.
- [21] Karnatak, H. C., Saran S., Bhatia K. and Roy P. S.: Multicriteria spatial decision analysis in web GIS environment, *Geoinformatica*, 11, 407–429, DOI: 10.1007/s10707-006-0014-8, 2007.
- [22] Kresic, N. (2010). Types and classifications of springs. In *Groundwater hydrology of springs* (pp. 31-85). Butterworth-Heinemann.
- [23] Krishnamurthy, J., Mani, A., Jayaraman, V., & Manivel, M.: Groundwater resources development in hard rock terrain-an approach using remote sensing and GIS techniques. *International journal of applied earth observation and geoinformation*, 2(3-4), 204-215, DOI: 10.1016/S0303-2434(00)85015-1, 2000.
- [24] Lee, S., Kim, Y. S., & Oh, H. J.: Application of a weights-of-evidence method and GIS to regional groundwater productivity potential mapping. *Journal of environmental management*, 96(1), 91-105, DOI: 10.1016/j.jenvman.2011.09.016, 2012.
- [25] Magowe, M., & Carr, J. R.: Relationship between lineaments and ground water occurrence in western Botswana. *Groundwater*, 37(2), 282-286, DOI: 10.1111/j.1745-6584.1999.tb00985.x, 1999.
- [26] Makropoulos C.K. and Butler D.: Spatial ordered weighted averaging: incorporating spatially variable attitude towards risk in spatial multi-criteria decision-making, *Environmental Modelling & Software*, 21/1, 69–84, DOI: 10.1016/j.envsoft.2004.10.010, 2006.
- [27] Malczewski J.: *GIS and Multicriteria Decision Analysis*, Wiley & Sons, Toronto, 1999
- [28] Mallick, J., Khan, R. A., Ahmed, M., Alqadhi, S. D., Alsubih, M., Falqi, I., & Hasan, M. A. (2019). Modeling groundwater potential zone in a semi-arid region of Aseer using fuzzy-AHP and geoinformation techniques. *Water*, 11(12), 2656.
- [29] Mahammad, S., & Islam, A. (2021). Evaluating the groundwater quality of Damodar Fan Delta (India) using fuzzy-AHP MCDM technique. *Applied Water Science*, 11(7), 1-17.

- [30] Mandal, U., Sahoo, S., Munusamy, S. B., Dhar, A., Panda, S. N., Kar, A., & Mishra, P. K.: Delineation of groundwater potential zones of coastal groundwater basin using multi-criteria decision making technique. *Water resources management*, 30(12), 4293-4310, DOI: 10.1007/s11269-016-1421-8, 2016.
- [31] <https://mpgmn.csb.gov.tr/adiyaman---sanliurfa---diyarbakir-planlama-bolge-i-82181>
- [32] Mendoza G.A. and H. Martins,: Multi-criteria decision analysis in natural resource management: A critical review of methods and new modelling paradigms, *Forest Ecology and Management*, 230/1–3, 1–22, DOI: 10.1016/j.foreco.2006.03.023, 2006.
- [33] MTA, <http://yebilimleri.mta.gov.tr/anasayfa.aspx>, last access: 28 September 2018.
- [34] Nag A, Ghosh S, Biswas S, Sarkar D, Sarkar P.: An image Steganography technique using X-box mapping. In: 2012 International conference on advances in engineering, science and management (ICAESM), pp 709–713. IEEE, 2012.
- [35] Nobre, R. C. M., Rotunno Filho, O. C., Mansur, W. J., Nobre, M. M. M., & Cosenza, C. A. N.: Groundwater vulnerability and risk mapping using GIS, modeling and a fuzzy logic tool. *Journal of Contaminant Hydrology*, 94(3-4), 277-292, DOI: 10.1016/j.jconhyd.2007.07.008, 2007.
- [36] Ö. Emre, Duman, T.Y., Özalp, S., Elmacı, H., Olgun, Ş. ve Şaroğlu, F.: 1/1.250.000 Ölçekli Türkiye Diri Fay Haritası, Maden Tetkik ve Arama Genel Müdürlüğü Özel Yayınlar Serisi-, Ankara, 2013.
- [37] Özden, D. M., Keskin, S., Dinç, U., Kapur, S., Akça, E., Şenol, S., & Dinç, O.: 1: 1.000.000 Ölçekli Türkiye Coğrafi Toprak Veri Tabanı, 2001.
- [38] Pradhan, B.: A comparative study on the predictive ability of the decision tree, support vector machine and neuro-fuzzy models in landslide susceptibility mapping using GIS. *Computers&Geosciences*, 51, 350-365, DOI: 10.1016/j.cageo.2012.08.023, 2013.
- [39] Rahman, M. A.,Rusteberg, B., Gogu, R. C., Ferreira, J. L., &Sauter, M.: A new spatial multi-criteria decision support tool for site selection for implementation of managed aquifer recharge. *Journal of environmental management*, 99, 61-75, DOI: 10.1016/j.jenvman.2012.01.003, 2012.
- [40] Rahmati O, Samani AN, Mahdavi M, Pourghasemi HR, Zeinivand H.: Groundwater potential mapping at Kurdistan region of Iran using analytic hierarchy process and GIS. *Arab J Geosci* 8(9):7059–707, DOI: 10.1007/s12517-014-1668-4, 2015.
- [41] Reid, M. E., & Iverson, R. M. (1992). Gravity-driven groundwater flow and slope failure potential: 2. Effects of slope morphology, material properties, and hydraulic heterogeneity. *Water Resources Research*, 28(3), 939-950.
- [42] Republic of Turkey Prime Ministry, GAP Regional Development Administration: GAP Bölge Kalkınma Planı 2002 (GAP Development Plan), Ankara, 2002.
- [43] Saaty T. L.: *The Analytic Hierarchy Process*, McGraw-Hill, New York, 1980.
- [44] Saaty, T. L.: Hierarchical-Multi objective Systems, *Control-Theory and Advanced Technology*, 5, 4, 485-489, 1989.

- [45] Saaty T.L.: *Fundamentals of Decision Making and Priority Theory*, RWS Pub., Pittsburgh, 2000.
- [46] Senanayake, I. P., Dissanayake, D. M. D. O. K., Mayadunna, B. B., & Weerasekera, W. L.: An approach to delineate groundwater recharge potential sites in Ambalantota, Sri Lanka using GIS techniques. *Geoscience Frontiers*, 7(1), 115-124, DOI: 10.1016/j.gsf.2015.03.002, 2016.
- [47] Shekhar S, Pandey A., C.: Delineation of groundwater potential zone in hard rock terrain of India using remote sensing, geographical information system (GIS) and analytic hierarchy process (AHP) techniques. *Geocarto Int* 30(4):402–421, DOI: 10.1080/10106049.2014.894584, 2015.
- [48] Triantaphyllou E, Sanchez A.: A Sensitivity Analysis Approach for some Deterministic Multi-Criteria Decision Making Methods. *Decision Sciences*, 28(1), 151-194, DOI: 10.1111/j.1540-5915.1997.tb01306.x, 1997.
- [49] Tarboton, D. G., Bras, R. L., & Rodriguez-Iturbe, I.: A physical basis for drainage density. *Geomorphology*, 5(1/2), 59-76, DOI: 10.1016/0169-555X(92)90058-V, 1992.
- [50] Tucker, G. E., & Bras, R. L.: Hillslope processes, drainage density, and landscape morphology. *Water Resources Research*, 34(10), 2751-2764, DOI: 10.1029/98WR01474, 1998.
- [51] Turkey Agricultural Ministry, <https://www.tarim.gov.tr/sgb/Belgeler/SagMenuVeriler/TRGM.pdf>, last access: 10 December 2018.
- [52] Turkey State Meteorology, <https://www.mgm.gov.tr/veridegerlendirme/il-ve-ilceleristatistik.aspx?k=A&m=DIYARBAKIR>, last access: 10 October 2018.
- [53] Verma, N., & Patel, R. K. (2021). Delineation of groundwater potential zones in lower Rihand River Basin, India using geospatial techniques and AHP. *The Egyptian Journal of Remote Sensing and Space Science*, 24(3), 559-570.
- [54] Wang, H., Gao, J. E., Zhang, M. J., Li, X. H., Zhang, S. L., & Jia, L. Z. (2015). Effects of rainfall intensity on groundwater recharge based on simulated rainfall experiments and a groundwater flow model. *Catena*, 127, 80-91.
- [55] Zaidi, F. K., Nazzal, Y., Ahmed, I., Naeem, M., & Jafri, M. K.: Identification of potential artificial groundwater recharge zones in Northwestern Saudi Arabia using GIS and Boolean logic. *Journal of African Earth Sciences*, 111, 156-169, DOI: 10.1016/j.jafrearsci.2015.07.008, 2015.

Design and Tests of Structural Post-Tensioned Glass T-Beams

Emrullah KOCA^{1*}
Ahmet TÜRER²



ABSTRACT

Glass manifests superior properties with high strength and transparency although it may not be considered as a commonly used structural material. This study targets to improve the structural performance of glass by post-tensioning; a series of T-shaped glass beams are tested to develop a proper and safe design. Traditionally, glass is widely used in buildings as windows where its brittleness and strength capacity are not significant. Architects prefer to use glass in the structural field because of aesthetics, recyclability, and transparency. Although there is more demand for the usage of glass as a structural material, a common fear of its brittle nature and lack of research about its structural behavior have mostly hindered it. Since glass is a brittle material and has high compressive strength in the order of 400 to 800 MPa and lower tensile strength (40 to 120 MPa), post-tensioning to target distributed loads is investigated to increase its fracture capacity and even obtain a post-cracking ductile behavior. In this study, several material tests are conducted to confirm the theoretical mechanical properties of glass. After obtaining the bending and compressive strength of the glass, Finite Element Models (FEMs) of the T-beams were generated and analytical hand calculations were conducted. The tests of T-shaped annealed (float) and tempered (toughened) glass beams with and without post-tensioning were conducted. The results of the experiments were compared with the analytical hand calculations and FEM results. A favorable outcome of this study is that float glass' post cracking strength has been drastically increased and a ductile post-cracking performance is obtained. Tempered glass has a brittle response but with much higher strength, with about 4 times the capacity of annealed glass T-beams

Keywords: Post-tensioned glass beam, T-beam, structural glass, glass beam test.

Note:

- This paper was received on December 14, 2023 and accepted for publication by the Editorial Board on April 5, 2024.
- Discussions on this paper will be accepted by November 30, 2024.
- <https://doi.org/10.18400/tjce.1405084>

1 Middle East Technical University, Department of Civil Engineering, Ankara, Türkiye
koca.emrullah@metu.edu.tr - <https://orcid.org/0000-0002-0459-7946>

2 Middle East Technical University, Department of Civil Engineering, Ankara, Türkiye
aturer@metu.edu.tr - <https://orcid.org/0000-0002-2214-1387>

* Corresponding author

1. INTRODUCTION

Glass is an inorganic, visco-elastic, and isotropic material with a non-crystalline molecular structure. The typical composition of glass consists of silica-SiO₂ (70-74%), lime-CaO (5-12%), soda-Na₂O (12-16%), and other chemical elements with influence on transmittance, thermal properties, tensile strength, fracture toughness, and color, etc. Considered a structural material, no plastic deformation occurs before the failure and it breaks suddenly similar to high-strength concrete. There are several types of glass such as float (annealed), heat-strengthened, fully tempered, laminated, and insulated. Typical fractures of different glass types are demonstrated in Fig. 1.



Fig. 1 - Typical fracture shapes of glass types [1]

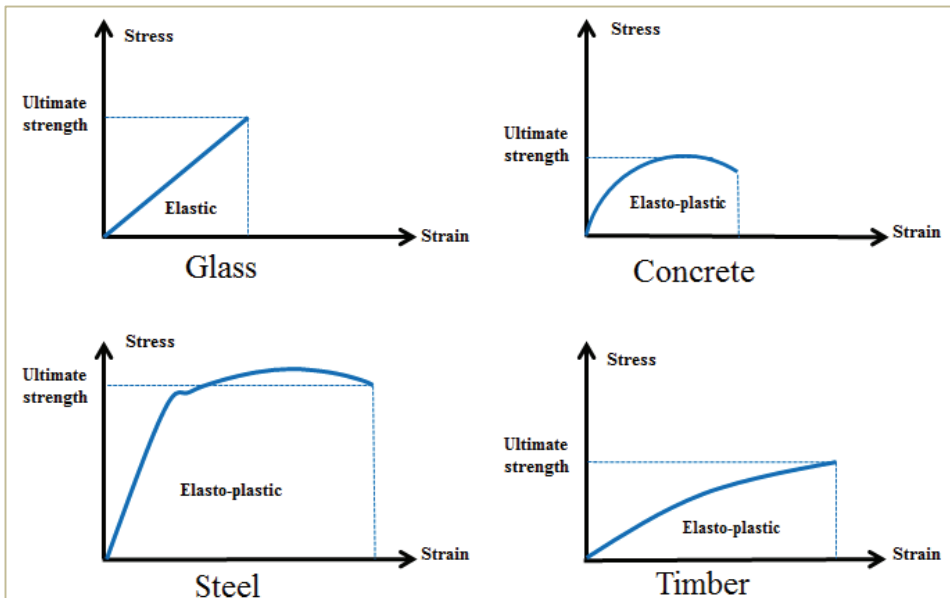


Fig. 2 - Typical stress-strain graphs of structural materials under bending

The compressive strength of glass is about ten times larger than its tensile strength, so the breakage of a glass beam is mostly governed by its tensile strength. Therefore, reinforced glass beams using rebars or even with post-tensioning would cause significant strength and ductility increase making it useable as a structural material such as in the case of reinforced concrete. Additional advantages such as prefabrication, visually pleasing, and high strength make glass superior to concrete under certain applications. Some mechanical and physical properties of glass are as follows: density (ρ)=2500 kg/m³, modulus of elasticity (E)=70 GPa, shear modulus (G)=30 GPa, and Poisson's ratio (ν)=0.23 [2, 3]. Typical stress-strain curves of structural materials such as glass, concrete, steel, and timber are compared in Fig. 2.

It should be noted that the graphs are not to scale. It can be inferred from the graphs that glass has brittle behavior somewhat like high-strength concrete and timber.

This research explores using a technique well-established in concrete construction (post-tensioning) for a new material (glass). The study investigates how the T-shaped cross-section, which is efficient for carrying loads, can be combined with post-tensioning for glass beams. The research includes data for two commonly used types of architectural glass, providing a broader understanding of the technique's effectiveness.

1.1. Post-Tensioning Application

Pre-stressing can be applied to members in two ways, pre-tensioning or post-tensioning. In pre-tensioned members, the pre-stressing strands are tensioned against restraining before the material is cast and the strands are released after hardening. Post-tensioning involves installing and stressing strand or bar tendons after the material has been placed, hardened, and attained a minimum compressive strength for the transfer. The function of post-tensioning is to generate a compression field, especially in regions where tensile stresses develop. Post-tensioning below the neutral axis in a simply supported beam would generate compression at the bottom and create an upward deflection; in this way, minimizes tensile stresses and beam deflections under loading in the gravitational direction. The post-tensioning wire may be placed with different geometric layouts to optimize the negative bending and camber to suit loading patterns. In this study, galvanized steel wire rope with an 8 mm diameter and ultimate strength (f_u) of 750 MPa was used as a post-tensioning member.

The advantages of using glass beams with post-tensioning can be considered as a) an increase in cracking capacity, b) ductility gained by post-cracking strength, c) no losses because of shrinkage (as in the case of post-tensioned concrete), d) making use of high strength of glass which is about 400 to 800 MPa in compression and about 40 MPa in tension, and e) appealing view of the transparent glass material.

1.2. Literature Review

The concept of post-tensioned glass beams has currently been studied in a limited number of research papers. The main goals of post-tensioning structural glass beams were explained as increasing the initial fracture strength of the glass and providing a significant post-fracture residual load-carrying capacity. However, in all of the studies, post-tensioning was applied in different ways and geometries.

Cupac *et al.* [4] offer a valuable starting point for anyone interested in understanding the potential and current advancements in post-tensioned glass beam technology. It provides a comprehensive survey of the field, highlighting the benefits, design considerations, and ongoing research directions for this promising structural application.

Belis *et al.* [5] studied the enhancement of the buckling strength of glass beams using lateral restraints focusing on load-bearing glass beams, subjected to different loading types. They concluded that the addition of point-wise lateral restraints has a very important positive effect on the load-bearing capacity of a beam subjected to a concentrated load.

Louter *et al.* [6] investigated the post-tensioning load transfer mechanism from the cable to the glass beam at its ends. In this research, it was observed that the most essential aspect of post-tensioning glass beams seems to be the alignment of the end pieces to match the inclination of post-tensioning forces.

Belis, Louter, *et al.* [7] worked on the effect of post-tensioning on the buckling behavior of a T-shaped glass beam. The conclusion was that the geometry of the prototype had relatively good resistance to buckling and the beam failed due to the fracture of glass.

Louter [8] studied the aspects of embedded reinforcement in layered glass beams numerically and experimentally. It was concluded that both the numerical and the experimental models provide a promising method for describing the structural response of reinforced glass beams.

Louter *et al.* [9] conducted experimental tests on beams with mechanically anchored post-tensioning tendons integrated at the top and bottom edges of the glass beams. It was concluded that post-tensioning using mechanically anchored or adhesively bonded tendons was a feasible concept, which provided increased initial fracture strength and enhanced post-fracture performance.

Engelmann and Weller [10] studied the results of three 9 m glass beams post-tensioned with 24 mm high-grade spiral cables. The primary aim was to describe the load-bearing behavior of large-span, post-tensioned glass beams and to determine their ultimate load-bearing capacity. The secondary aim was to present a practical application by designing a 9 m pedestrian bridge. It was concluded that numerical methods were suitable for preliminary design. Furthermore, a 9 m span is said to be feasible and confirmed with test results.

Cupac *et al.* [11] investigated the mechanisms that can cause failure in post-tensioned glass beams. Their design used a flat stainless-steel tendon bonded with adhesive to the underside of the glass. The potential failure modes included the tendon snapping, the glass itself fracturing under tension, and the adhesive bond failing at the point where the load is introduced. The researchers compared the results of their physical model with a computer simulation, finding good agreement between the two. Finally, they used this validated model to conduct a parametric study, which explored how different beam design choices affect the effectiveness of post-tensioning in glass beams.

Several other studies have been found in the literature, reporting the behavior of laminated glass beams with or without post-tensioning [12-16]. The lamination process allows the usage of multiple layers of glass and post-cracking behavior is better controlled preventing shattering.

Although post-tensioning was applied in different patterns and shapes, more research should be done about structural glass to effectively use it as a structural material. This study aims to

investigate numerical and experimental aspects of glass T-beams with and without post-tensioning on float and tempered glass.

2. MATERIAL TESTS

Several compression and bending (indirect tension) material tests were conducted to confirm the theoretical mechanical properties of glass. Compression tests were conducted with cubes of float glass in 60x60x60 mm dimensions. However, the cubes were prepared using 10 layers of 60x60x6 mm thick glass pieces piled on top of each other. The tests (Fig. 3) yielded a compressive strength of 267 MPa, which is much lower than the theoretical 400 MPa. Specimens had partial cracking and portion spalling, which indicated an uneven stress distribution. The layered characteristic of test specimens is deemed to cause small gaps and variations in stress; therefore, the compressive strength was assumed as 400 MPa for post-tensioned T-beam tests, and no compression failure was observed. Although the shear capacity of glass is not broadly referenced, the compressive and tensile capacities were utilized together with the Coulomb-Mohr Fracture Criterion [14] to calculate shear strength as 36.4 MPa for float glass and 92.3 MPa for tempered glass.

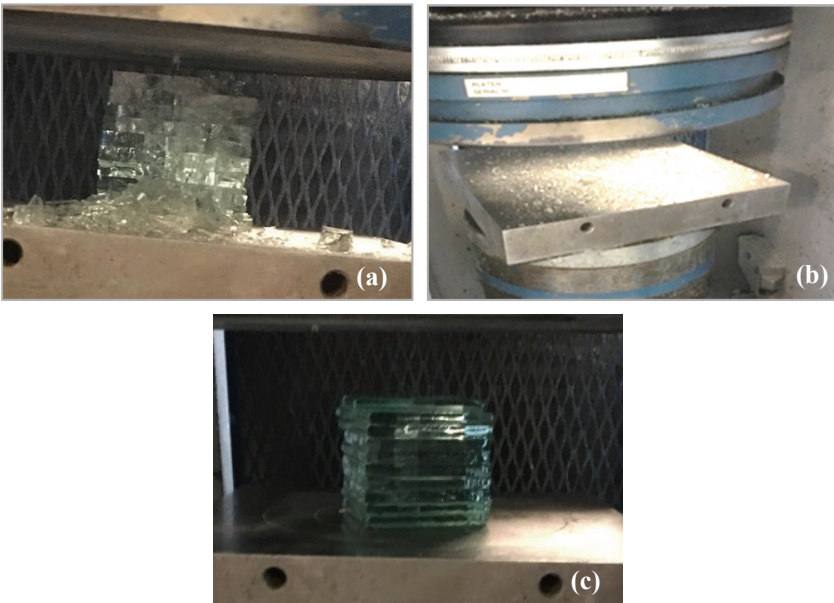


Fig. 3 - A glass cube a) before, b) exploded after, and c) premature failure after the compression test

Float and tempered glass samples were also tested under bending both in their weak and strong axes to determine the bending (indirect tension) strength of glass. The reason for testing samples both in their weak and strong axes was to see how the characteristic strength changes concerning the glass edge placement. Three samples from each 1000x100x6mm and 1000x200x6 mm dimensioned specimens were loaded from two 1/3 length points until they

were fractured (Fig. 4). The same bending test procedure was conducted on three sets of samples. Load-displacement graphs were obtained by post-processing data recorded from the data logger. The load-displacement graphs of float glass specimens placed in their weak axes are given in Fig. 5(a), and their strong axes are shown in Fig. 5(b).

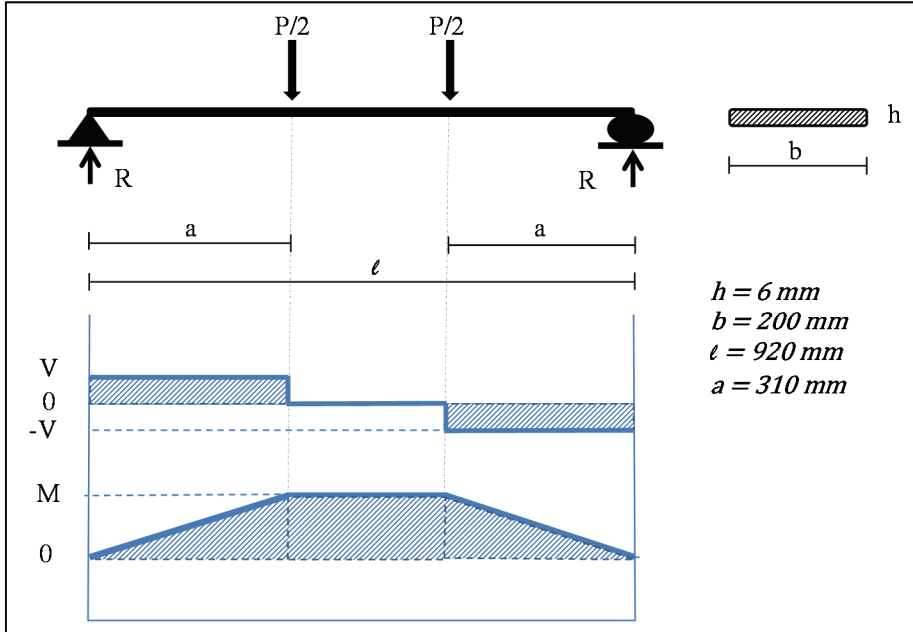
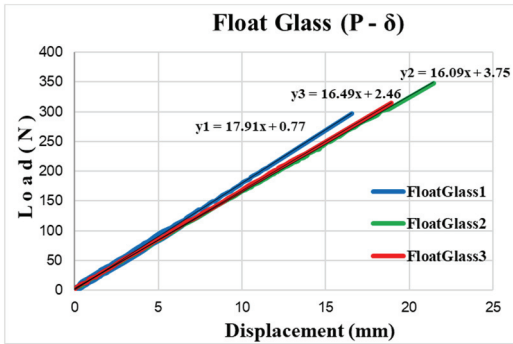
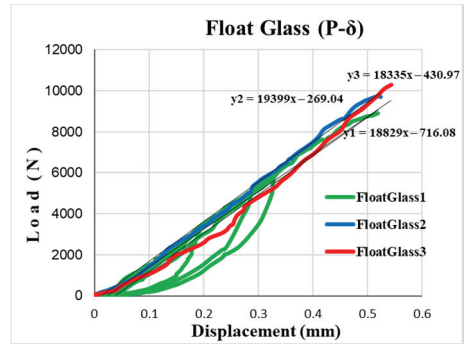


Fig. 4 - Test setup, and shear and moment diagrams of the test specimens



(a)



(b)

Fig. 5 - Bending test load-displacement graph of float glass (a) weak axis and (b) strong axis

Bending strength (σ) (indirect tension) and elastic modulus (E) were calculated using standard engineering formulas and listed in Table 1 together with their theoretical counterparts. The mean bending strength and elastic modulus were comparable to the values found in the literature. The characteristic bending strength and modulus of elasticity (with a %5 probability of lowering) were obtained for design purposes.

Table 1 - Theoretical-experimental values of mean-characteristic strength and modulus of elasticity

	Tensile Strength		
	<u>Experimental (MPa)</u>		<u>Theoretical (MPa)</u>
	Weak axis	Strong axis	
Float Glass	33.58	32.64	40
Tempered Glass	121.7	169.27	120
	Modulus of Elasticity		
	<u>Experimental (MPa)</u>		<u>Theoretical (MPa)</u>
	Weak axis	Strong axis	
Float Glass	57.15	62.1	70
Tempered Glass	55.74	62.58	70

3. HAND CALCULATIONS OF GLASS T-BEAMS

Dimensions of the T-beam were selected as shown in Fig. 6. Simply supported T-beam specimens were tested under 8-point loading both for beams with and without post-tensioning. The main reason for the 8-point loading test was to mimic a uniformly distributed loading case which was not studied in the literature and is a very common loading pattern. Furthermore, the post-tensioning tendon creates a reverse uplift force and bending moment which is very similar to the one created by a uniform loading, such that two effects cancel each other. The horizontal component of tendon force at each transfer point is small, beneficiary, and neglected for practical reasons. Maximum shear force, moment, and deflection of a simply supported T-beam with 8-point loads are calculated. Then, a stress check procedure was carried out for the float and tempered glass T-beam cases to calculate the maximum load that beams can bear.

Maximum load-carrying capacity (P_{max}) was calculated for float and tempered glass beams without post-tensioning by common formulas (Eq. (1)). The governing failure stress is considered to be the tensile strength; however, the compressive and shear strengths are also checked. The maximum deflection (δ_{max}) of the T-beam is calculated using the Moment Area Method (Eq. (2)). Calculation results of T-beam without post-tensioning are tabulated in Table 2.

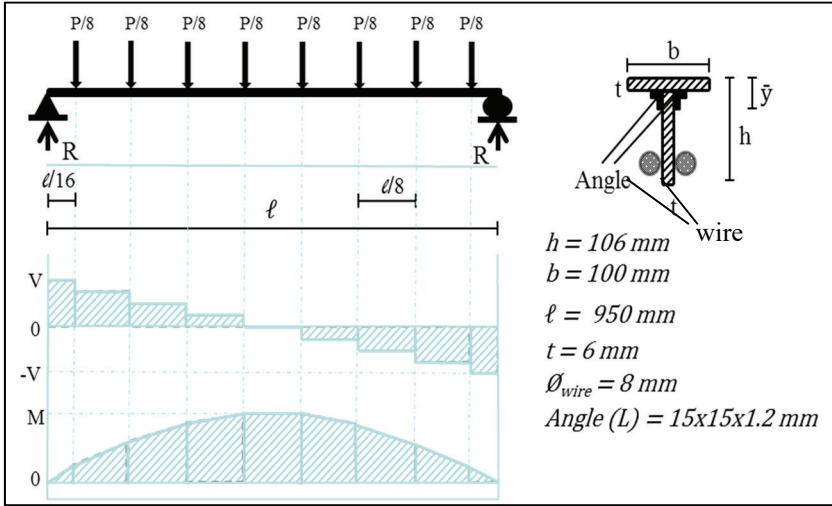


Fig. 6 - Cross-section, loading pattern, shear force, and moment diagrams of the T-beam

$$P_{\max} = \frac{8 \cdot \sigma_{\text{bottom}} \cdot I_{\text{beam}}}{(h - \bar{y}_{\text{beam}}) \cdot \ell} \quad (1)$$

$$\delta_{\max} = \frac{658}{49152} \frac{P_{\max} \ell^3}{EI_{\text{beam}}} \quad (2)$$

where I_{beam} stands for a moment of inertia, \bar{y}_{beam} for neutral axis, and E for modulus of elasticity of the T-beam.

Table 2 - Calculation results of T-beam without post-tensioning

Parameters	Float Glass	Tempered Glass
P_{\max} (kN)	4.86	25.19
δ_{\max} (mm)	0.66	3.37
σ_{top}^* (MPa)	11.94 < 400	61.94 < 400
σ_{bottom} (MPa)	32.64	169.27
$\tau_{\text{neutral axis}}$ (MPa)	5.34 < 36.4	25.83 < 92.3
$\tau_{\text{glue line}}^{**}$ (MPa)	4.50 < 36.4	21.79 < 92.3

*compression ** at the web and flange connection

The post-tensioned glass T-beams shall be analyzed for transfer (short term) and final (long term) cases. The transfer case is when the beam is under its self-weight and post-tensioning

load; the final case is when the beam is subjected to all loads such as post-tensioning load, live load, self-weight, relaxation, etc. Shear force and moment diagrams due to post-tensioning are shown in Fig. 7.

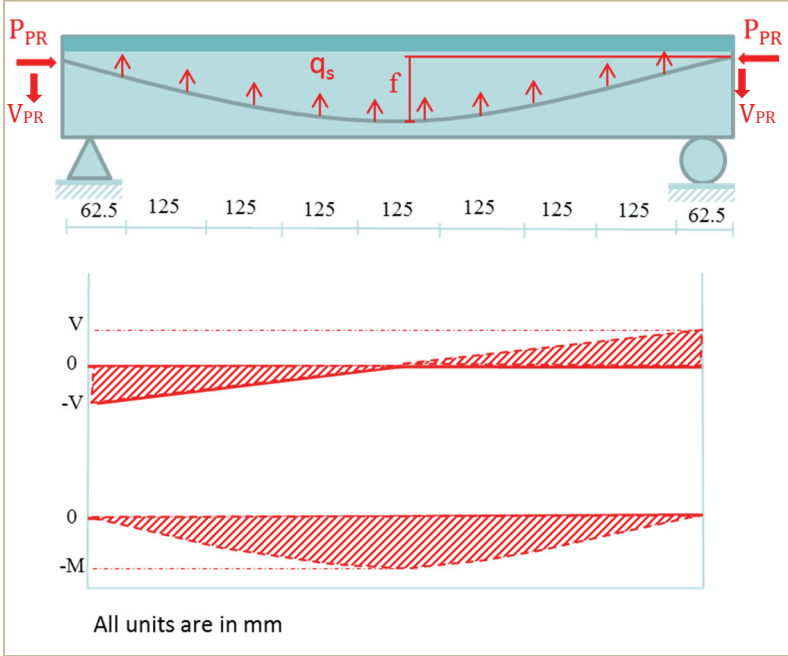


Fig. 7 - Shear force and moment diagrams due to post-tensioning

The post-tensioning force (P_{PR}) is calculated using Eq. (3) where f_u is the ultimate tensile strength and A is the cross-sectional area of tendon. The losses for post-tensioning were considered to be 15% to 25%. Moment due to post-tensioning (M_{PR}) is calculated by Eq. (4) and shear force (V_{PR}) by Eq. (5).

$$P_{PR} = (1 - \text{Percentage of loss}) * (\text{Tensioning ratio}) * (f_u) * A_{\text{tendon}} \quad (3)$$

$$M_{PR} = P_{PR} * f = q_s * \frac{(\ell)^2}{8} = P * \ell / 8 \Rightarrow q_s = \frac{8 * P_{PR} * f}{(\ell)^2} \quad (4)$$

$$V_{PR} = q_s * \frac{\ell}{2} \quad (5)$$

Stresses at the top and bottom ($\sigma_{\text{top}}, \sigma_{\text{bottom}}$) of the T-beams' mid-spans are calculated according to the equations for transfer and final cases (Eqs. (6), (7), (10), and (11)). Shear stress at neutral and glue points are calculated by Eqs. (8), (9), (12), and (13). In the equations below, $\Delta M_{\text{transfer}}$ is the moment at the mid-span of the T-beam under dead load and post-tensioned load, and ΔM_{final} is the moment at the mid-span of the T-beam under all loads

including post-tensioned load, $\Delta V_{transfer}$ is the shear force at the mid-span of the T-beam under dead load and post-tensioned load, and ΔV_{final} is the shear force at the mid-span of the T-beam under all loads including post-tensioned load,

Transfer (Short-term) Case

$$\sigma_{top} = \frac{-P_{PR}}{A_{beam}} - \frac{\Delta M_{transfer} * \bar{y}_{beam}}{I_{beam}} \quad (6)$$

$$\sigma_{bottom} = \frac{-P_{PR}}{A_{beam}} + \frac{\Delta M_{transfer} * (h - \bar{y}_{beam})}{I_{beam}} \quad (7)$$

$$\tau_{neutral\ axis} = \frac{\Delta V_{transfer} * Q_{neutral}}{I_{beam} * t} \quad (8)$$

$$\tau_{glue\ point} = \frac{\Delta V_{transfer} * Q_{glue\ point}}{I_{beam} * t} \quad (9)$$

Final (Long term) Case

$$\sigma_{top} = \frac{-P_{PR}}{A_{beam}} - \frac{\Delta M_{final} * \bar{y}_{beam}}{I_{beam}} \quad (10)$$

$$\sigma_{bottom} = \frac{-P_{PR}}{A_{beam}} + \frac{\Delta M_{final} * (h - \bar{y}_{beam})}{I_{beam}} \quad (11)$$

$$\tau_{neutral\ axis} = \frac{\Delta V_{final} * Q_{neutral}}{I_{beam} * t} \quad (12)$$

$$\tau_{glue\ point} = \frac{\Delta V_{final} * Q_{glue\ point}}{I_{beam} * t} \quad (13)$$

The maximum load ($P_{crack/ultimate}$) that the T-beam can sustain is calculated by Eq. (14). The maximum load for float glass is considered to be the cracking load while it is considered as an ultimate load for tempered glass.

$$P_{crack\ or\ ultimate} = \left(\frac{(\sigma_{bottom} + \frac{P_{PR}}{A_{beam}}) * I_{beam}}{(h - \bar{y}_{beam})} + M_{PR} \right) * \frac{8}{\ell} \quad (14)$$

All calculations done for post-tensioned glass T-beams are tabulated in Table 3.

Compared with T-beam without post-tensioning, the maximum load that the same dimensioned T-beam can resist increased from 4.86 kN to 10.53 kN for float glass and from 25.19 kN to 39.97 kN for tempered glass. Theoretically, the tensile strength capacity increased substantially after the post-tensioning application.

Table 3 - Calculation results of post-tensioned T-beam

	Property	Float Glass	Tempered Glass
Transfer case	P_{PR} (kN)	8.26	21.54
	$\delta_{transfer}$ (mm)	0.62	1.60
	σ_{top} (MPa)	5.00	13.20
	σ_{bottom} (MPa)	-37.89	-99.38
Final case	$P_{crack/ult.}$ (kN)	10.53	39.97
	δ_{final} (mm)	0.81	3.754
	σ_{top} (MPa)	-20.68	-85.12
	σ_{bottom} (MPa)	32.30	169.47
	$\tau_{neutral\ axis}$ (MPa)	6.34	32.39
	$\tau_{glue\ line}$ (MPa)	5.34	27.32

4. NUMERICAL MODELING OF T-BEAMS

The finite element models (FEMs) of T-beams were modeled in structural software for analysis and design (SAP2000 v.20). Post-tensioned float and tempered glass T-beams were modeled as well as the models without post-tensioning. After defining the materials and sections, the T-beam was modeled as shown in Fig. 8.

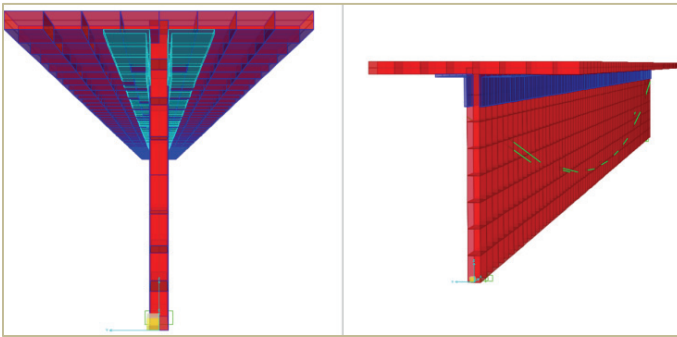


Fig. 8 – Finite element model of post-tensioned float glass T-beam

In the T-beam structural model, glass, aluminum, and wire rope were defined. The aluminum was defined as AA6063-T6 from SAP2000 materials manual, while glass is defined as in Fig. 9.

The L-shaped aluminum angles were defined as 2x15x15x1.2 mm dimensioned double angle section with a back-to-back spacing of 6 mm (Fig. 10). The wire used in the specimen for post-tensioning is defined as a tendon as shown in Fig. 11.

The dialog box titled "Material Property Data" is divided into three sections. The "General Data" section includes a text field for "Material Name and Display Color" containing "Glass", a dropdown for "Material Type" set to "Other", and a "Modify/Show Notes..." button. The "Weight and Mass" section has input fields for "Weight per Unit Volume" (2,452E-05) and "Mass per Unit Volume" (2,500E-09), along with a "Units" dropdown set to "N, mm, C". The "Isotropic Property Data" section contains input fields for "Modulus Of Elasticity, E" (62096), "Poisson, U" (0,23), "Coefficient Of Thermal Expansion, A" (9,000E-06), and "Shear Modulus, G" (25242,276).

Fig. 9 - Material property data of glass

The dialog box titled "Double Angle Section" is divided into several sections. The "Section Name" is "2xT15x15x1.2" and "Section Notes" has a "Modify/Show Notes..." button. The "Dimensions" section includes input fields for "Outside depth (t3)" (15), "Outside width (t2)" (36), "Horizontal leg thickness (tf)" (1,2), "Vertical leg thickness (tw)" (1,2), and "Back to back distance (dis)" (6). The "Section" section shows a grid with a diagram of a double angle section. The "Material" section has a dropdown set to "6063T6". The "Property Modifiers" section has a "Set Modifiers..." button. The "Properties" section has buttons for "Section Properties..." and "Time Dependent Properties...".

Fig. 10 - Aluminum double angle section definition

Then it was loaded to the maximum load found from calculations, the stress at the top and bottom of the mid-span of the beam was found both at transfer and final cases. The stress distribution at transfer case of post-tensioned float glass T-beam is displayed in Fig. 12, and at the final case in Fig. 13.

S Tendon Section Data

Tendon Section Name: 8mmRope

Section Notes: Modify/Show...

Tendon Modeling Options For Analysis Model

- Model Tendon as Loads
- Model Tendon as Elements

Tendon Parameters

Prestress Type: Prestress

Material Property: + A416Gr250-PT

Tendon Properties

- Specify Tendon Diameter: 8.
- Specify Tendon Area: 50.2655
- Torsional Constant: 402.1239
- Moment of Inertia: 201.0619
- Shear Area: 45.2389

Units: N, mm, C

Display Color:

Fig. 11 - Tendon section data

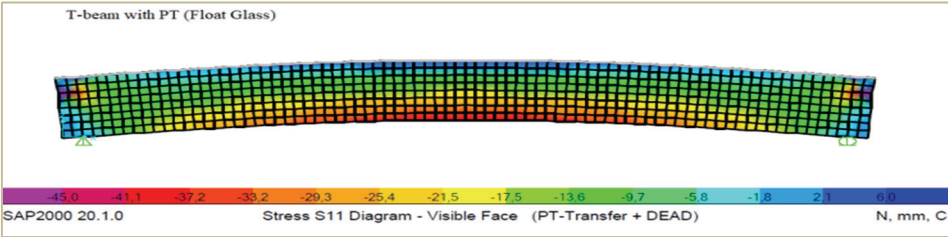


Fig. 12 - Stresses at transfer case of post-tensioned float glass T-beam

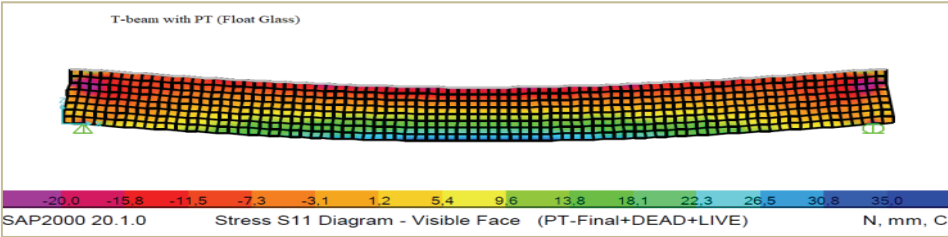


Fig. 13 - Stresses at the final case of post-tensioned float glass T-beam

FEM results of T-beams with post-tensioning at their mid-spans are tabulated in Table 4.

Table 4 - FEM results of T-beam with post-tensioning

Property	Float Glass		Tempered Glass	
	Transfer Case	Final Case	Transfer Case	Final Case
δ_{max} (mm)	0.70	0.82	1.84	3.92
$\sigma_{max,tensile}$ (MPa)	4.88	32.73	12.86	169.3
$\sigma_{max,compressive}$ (MPa)	-39.22	-23.82	-103.3	-95.89

Results taken from FEMs were close to hand calculations both for float and tempered glass types. The FEM results will be compared with hand calculations and experiment outputs and discussed in the following sections.

5. TESTS OF T-BEAMS

5.1. Test Setup and Components

T-beam specimens were prepared for the tests with and without post-tensioning. The web and flange of the T-Beam were 1000 mm in length, 100 mm in height, and 6 mm in thickness. The flange and web parts of the glass beam were bonded with two aluminum L profiles in 15x15x1.2 mm dimensions with the help of polyurethane-based adhesive as a bonding material. Aluminum alloy AA6063-T6 type is used. The parabolic shape of the wire rope and coordinates of the brass connection points are shown in Fig. 14. All the units given in the figure are in millimeters.

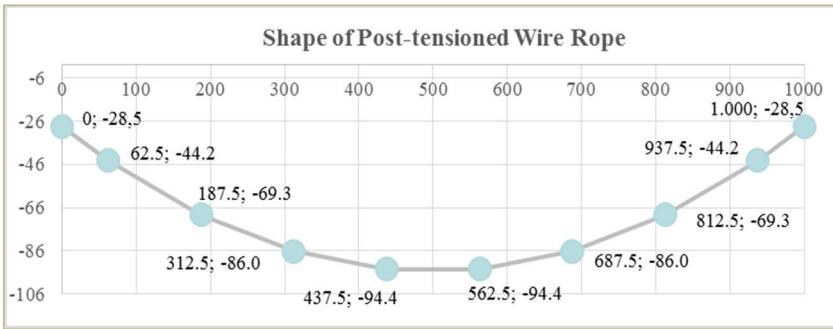


Fig. 14 - Geometry and coordinates of post-tensioned wire rope connectors

The set-up of a T-beam sample without post-tensioning is displayed in Fig. 15a and the set-up of post-tensioned T-beam in Fig. 15b.

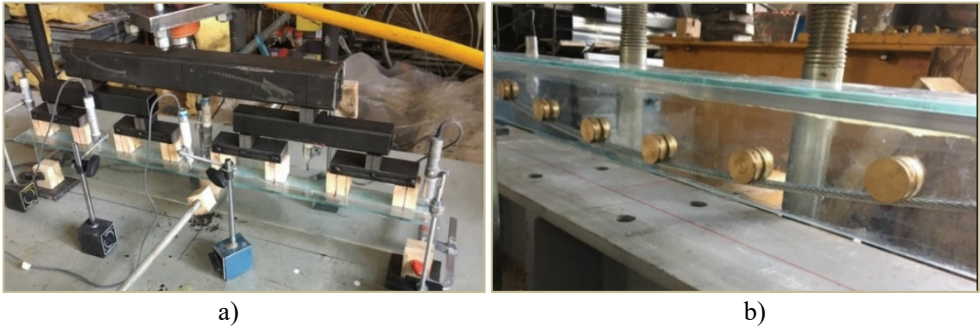


Fig. 15 - Test set-up of T-beam (a) without post-tensioning and (b) with post-tensioning

5.2. Conducting the Tests and Obtaining the Results

Three specimens of each type (float and tempered) of T-beams with and without post-tensioning tests were conducted. The specimens were loaded until their fracture point. The float glass without post-tensioning fractured at the constant moment zone due to tensile stress. The crack started at the constant moment zone of the tensile area and fragmented upwards to the compression zone (Fig. 16).



Fig. 16 - Float glass T-beam exposed to its cracking load



Fig. 17 - Tempered glass T-beam exposed to its ultimate loading

Tempered glass T-beam fractured into small pieces at its ultimate load in the maximum moment zone without any ductility as shown in Fig. 17.

The load-displacement graphs of float and tempered glass T-beam specimens are given in Fig 18. Rapid unloading at about 10 kN and 15 kN loads indicated some energy dissipating mechanisms, which may be related to the hydraulic loading jack’s damping properties. However, no residual deformations were observed as all tests returned to their original starting points.

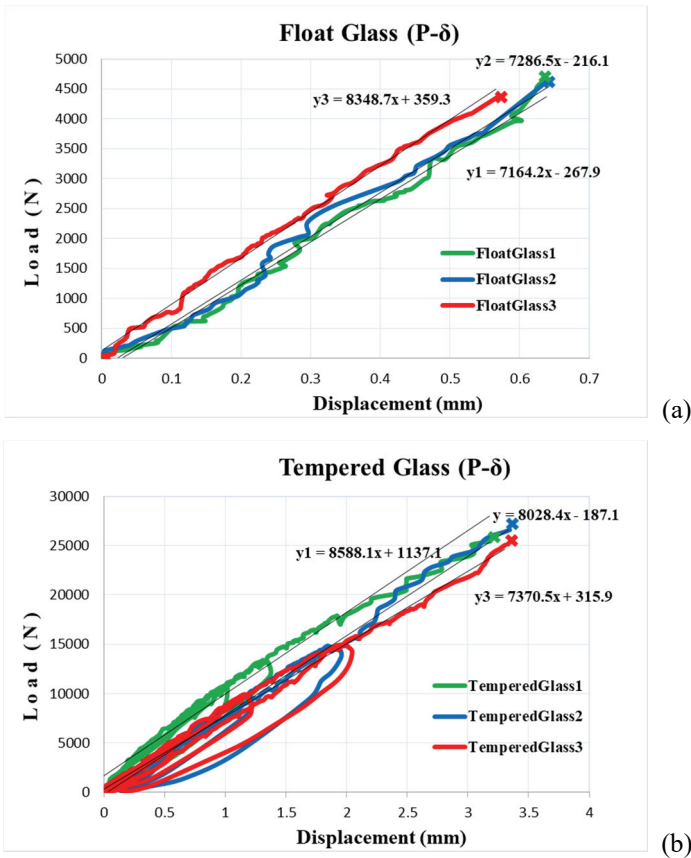


Fig. 18 - Load-displacement graph of (a) float and (b) tempered glass T-beam without post-tensioning

Although promising results were obtained from the tests compared with hand calculations and FEMs, the modulus of elasticity and characteristic strength of the T-beam without post-tensioning are also calculated as it was done for material tests. The aim was to confirm whether the T-beam concept was proper with the bonding material and aluminum L-shaped angle. The results of the modulus of elasticity and characteristic strength calculations are given in Table 5.

Table 5 - Calculation results of characteristic modulus of elasticity and strength for glass T-beam samples

	Characteristic Tensile Strength (MPa)	Characteristic Modulus of Elasticity (GPa)
Float Glass	29.34	52.21
Tempered Glass	160.04	61.23

As it is seen, the characteristic strength and modulus of elasticity results obtained for the T-beam were almost the same results in the material tests, so the glue material used and the T-beam concept were accepted.

The T-beams for post-tensioning tests were prepared in the same way as the T-beam without post-tensioning. The tests conducted for T-beams with post-tensioning were the most crucial and difficult part of the study since the wire rope slipping problem had to be overcome. This problem was overcome with grips used at the supports which are used to grasp wires tightly with no movement. After the setup was prepared, the wire rope was tensioned to 8.25 kN for float glass and to 21.58 kN for tempered glass. These post-tensioning forces were determined by following the standard procedure of concrete beams except for shrinkage losses. The relaxation, slippage, and creep losses were considered and transfer stresses (tension at the top) and design loads (tension at the bottom) were considered. Web shear, support bearing, flange-web shear transfer, flange, and web buckling checks were made.

Starting loading, the first crack was observed at the maximum moment region in the tests of float glass with post-tensioning. As the loading progressed, more cracks were observed propagating towards the supports of the beam and from the bottom (tension) to the top (compression) zone (Fig. 19).

Deflection-controlled loading test results for the post-tensioned float glass T-beam are given in Fig. 20. The graph shows how the mid-span of the beam deflects with post-tensioning load and vertical loading. The upward direction was assumed a positive deflection and the downward as a negative deflection.

The float glass T-beam deflected 0.62 mm upward at its mid-span when post-tensioning of 8.25 kN is applied (Point 1 in Fig. 20). Then, the beam was loaded at 8 points in a pattern close to uniform loading and cracked at 10.86 kN corresponding to 0.749 mm downward deflection at the mid-span (Point 2 in Fig. 20). The cracks first appeared around the maximum bending moment zone at the mid-span and then spread out towards the supports while the beam was continued to be loaded (Between points 2 and 3 in Fig. 20). The fluctuations occurred as a result of progressing cracks.

The beam was unloaded at 15.72 kN load which corresponds to 12.5 mm deflection at its mid-span, where cracks were too large to proceed with the test (Point 3 in Fig. 20). The tests for the second and the third samples of post-tensioned float glass T-beams were conducted the same way and the results were all close to each other.

The tempered glass T-beam with post-tensioning fractured into small pieces at its cracked and ultimate load condition as shown in Fig. 21.



Fig. 19 - Float glass T-beam with post-tensioning after the fracture.

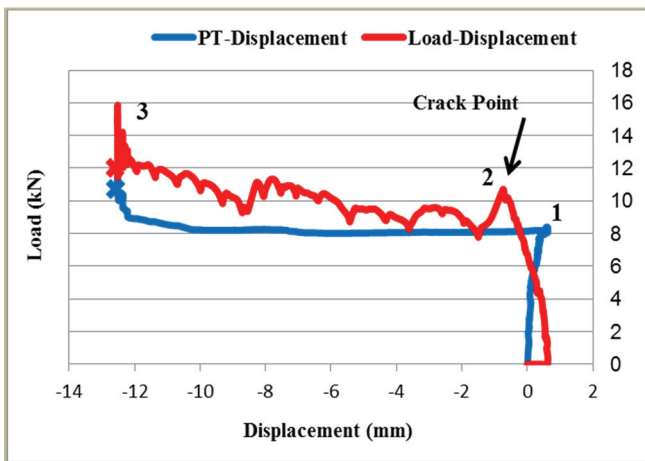


Fig. 20 - Load-displacement graph of post-tensioned float glass T-beam



Fig. 21 - Post-tensioned tempered glass T-beam after fracture.

The tempered glass T-beam had been post-tensioned to 21.54 kN. The sample deflected 1.66 mm in an upward direction upon post-tensioning (Point 1 in Fig. 22). Then, the beam was loaded at 8 points and started to deflect downward. The first sample cracked at 37.98 kN corresponding to 4.26 mm downward deflection at its mid-span. The first crack also marked the ultimate load capacity of the beam since tempered glass breaks in an explosive manner separating into small pieces of glass (Point 2 in Fig. 22).

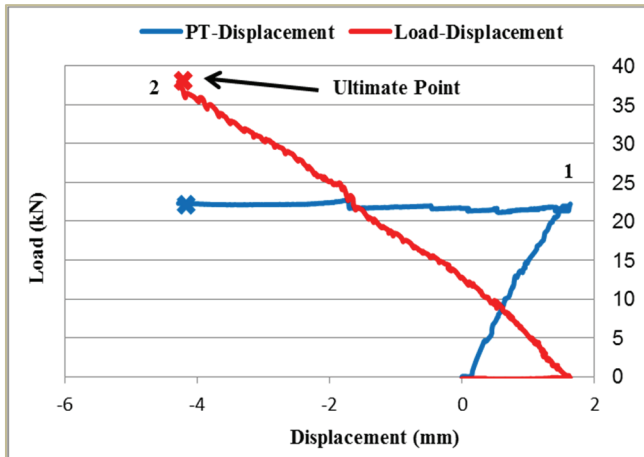


Fig. 22 - Load-displacement graph of post-tensioned tempered glass T-beam

The loading tests were repeated three times on similar samples and the average test results of T-beam samples are summarized below (Table 6).

After the tests, it was seen that T-beams without post-tensioning had a brittle failure. The tempered glass beam failed at 25.69 kN, which is 5.39 times higher than the float glass beam failure at 4.76 kN. Tempered glass T-beam with post-tensioning again had a brittle failure

but at 1.55 times higher load (39.79 kN) compared with the same tempered glass T-beam without post-tensioning. The capacity increase of the maximum load that T-beams with post-tensioning can resist depends on the post-tensioning design such as the tensioning ratio, the quantity of the wire rope, etc. However, a more preferable result was obtained from post-tensioned float glass which had a ductile failure. The crack load was 11.15 kN, which is 2.34 times higher than the same beam without post-tensioning. Moreover, the ultimate load was recorded as 19.28 kN, which is 4 times higher than the load float glass T-beam without post-tensioning can sustain. The comparisons between different types of the same dimensioned T-beams according to the test results are displayed in a column chart in Fig. 23.

Table 6 - Summary of T-beam test results

	T-beam without PT		T-beam with PT	
	Float Glass	Tempered Glass	Float Glass	Tempered Glass
P _{crack/ultimate} (kN)	4.76	25.69	11.14	39.79
δ _{max} (mm)	0.63	3.28	0.75	4.05

The capacities are accepted to be the cracking point, even though the post-tensioned float glass T-beam had post-tensioning ductile behavior. It can be concluded that the most preferable result was obtained from post-tensioned float glass, which had a ductile failure and a good post-fracture performance. The same amount of tempered glass may provide up to 4 times the strength; nevertheless, a sudden brittle failure may not be acceptable.

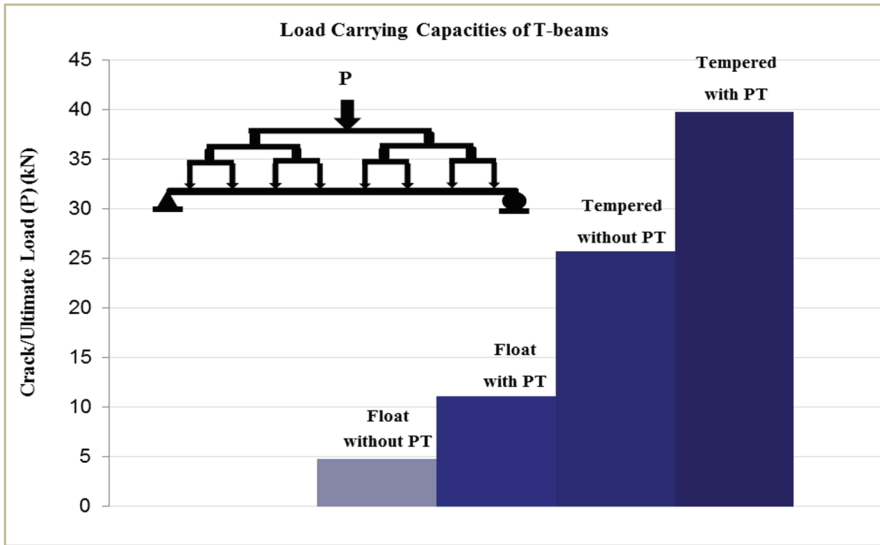


Fig. 23 - Load-carrying capacities of the same dimensioned T-beams

The results for T-beam of finite element models (FEMs), hand calculations, and tests were compared with load-deflection behavior and tabulated in Table 7 for T-beams without post-tensioning and in Table 8 for post-tensioned T-beams.

Table 7 - Summary of the results for T-beam without post-tensioning

	Float Glass		Tempered Glass	
	P_{crack} (kN)	δ_{max} (mm)	$P_{crack/ultimate}$ (kN)	δ_{max} (mm)
Hand Calc.	4.86	0.66	25.19	3.37
FEM	4.86	0.70	25.19	3.64
Test	4.76	0.63	25.69	3.28

Table 8 - Summary of the results for T-beam with post-tensioning

	Float Glass		Tempered Glass	
	P_{crack} (kN)	δ_{max} (mm)	$P_{crack/ultimate}$ (kN)	δ_{max} (mm)
Hand Calc.	10.53	0.81	39.97	3.75
FEM	10.53	0.82	39.97	3.92
Test	11.14	0.75	39.79	4.05

Comparison of hand calculations and FEM analyses with the test results showed a good correlation within the range of about $\pm 3\%$. These results can be deemed as in good agreement, considering that the glass test results had a scatter of about $\pm 4\%$. It can be concluded that both hand calculations and FEMs are valid for the design of post-tensioned glass T-beams.

6. CONCLUSION AND FUTURE WORK

The chosen problem is to investigate the feasibility of using post-tensioning to improve the structural performance of glass beams, specifically T-shaped beams. The use of glass as an architecturally appealing and structurally high-strength material (float glass tension capacity 40 MPa compression capacity 400 MPa and tempered glass tension capacity 120 MPa compression capacity 400-800 MPa) for load-carrying members is studied. The study includes numerical and experimental work on T-shaped glass beams considering post-tensioning. A minimalistic geometric approach was taken with the T-shape as the floor formed the top flange. One of the best outcomes of this study is that float glass post-cracking deflection can be drastically increased in a ductile manner while about a 55% increase in strength is achieved. This means that glass may be used as a beam in the construction field.

Comparison of the hand calculations, FEM analyses, and test results gave close values; therefore, analyses are close to the experimental results showing confidence for design.

Although the capacity of tensile strength increased in tempered glass T-beam, it still fractured and collapsed suddenly at its ultimate strength as expected. However, the superior post-cracking performance was achieved for post-tensioned float glass as an additional safety property even though glass is a brittle material.

Studies for the behavior of laminated or heat-strengthened glass with samples being tested under combined or more complex loading scenarios may be studied as future work. Also, glass being a visco-elastic material having some liquid-like properties, post-tensioned glass beams may be better checked for post-tensioning force losses at certain time intervals. Furthermore, exploring practical methods for fabricating, installing, and maintaining post-tensioned glass beams in real-world applications and analyzing the life cycle assessment of post-tensioned glass T-beams to understand their environmental impact compared to traditional materials contributes to the usage of glass as a viable and sustainable option for modern architecture.

References

- [1] Super safe CE certified 13.52 mm laminated glass panels for padel tennis court (2021, November) <https://www.szdragonglass.com/13-52-laminated-glass-panels-for-padel-court/>
- [2] BS EN 572-1 (2004), Glass in Building - Basic soda lime silicate glass products Part 1: Definitions and general physical and mechanical properties, European Committee for Standardization.
- [3] EN 572-2 (2004), Glass in Building - Basic Soda Lime Silicate Glass Products - Part 2: Float Glass, European Committee for Standardization.
- [4] Cupać, J., Louter, C., & Nussbaumer, A. (2021). Flexural behaviour of post-tensioned glass beams: Experimental and analytical study of three beam typologies. *Composite Structures*, 255, 112971.
- [5] Belis, J., Van Impe, R., Lagae, G. and Vanlaere, W. (2003), "Enhancement of the buckling strength of glass beams by means of lateral restraints.", *Structural Engineering and Mechanics*, 15(5), 495-511. <https://doi.org/10.12989/sem.2003.15.5.495>.
- [6] Louter, C., Heusden, J. Veer, F., Vambersky, J., Boer, H., Versteegen, J. (2006), "Post-tensioned glass beams.", https://www.researchgate.net/publication/241016445_Post-Tensioned_Glass_Beams
- [7] Belis, J., Louter, C., Verfaillie, K., Van Impe, R., and Callewaert, D. (2006), "The effect of post-tensioning on the buckling behaviour of a glass T-beam.", *Proceedings of International Symposium on the Application of Architectural Glass*, (129-136).
- [8] Louter, C. (2011), "Fragile yet Ductile, Structural Aspects of Reinforced Glass Beams". Ph.D. Dissertation, Technische Universiteit, Delft.

- [9] Louter, C., Cupac, J., and Lebet, J. P. (2014), “Exploratory experimental investigations on post-tensioned structural glass beams.”, *Journal of Façade Design and Engineering*, 2(1-2), 3-18. DOI: 10.3233/FDE-130012
- [10] Engelmann, M., Weller, B. (2016), “Post-tensioned Glass Beams for a 9 m Spannglass Bridge.”, *Structural Engineering International*, 26(2), 103-113. DOI: 10.2749/101686616X14555428759000
- [11] Cupac, J., Louter, C., & Nussbaumer, A. (2021). Post-tensioning of glass beams: Analytical determination of the allowable pre-load. *Glass Structures & Engineering*, 6(2), 233-248.
- [12] Weller, B. and Engelmann, M. (2014), “Deformation of Span-glass beams during post-tensioning”, *Proceedings of Challenging Glass 4 & Cost Action TU0905 Final Conference*, London, United Kingdom. https://www.researchgate.net/publication/290179946_Deformation_of_Spannglass_beams_during_post-tensioning
- [13] Jordão, S., Pinho, M., Martins, J.P., Santiago, A., and Neves, L.C. (2014), “Behaviour of laminated glass beams reinforced with pre-stressed cables.”, *Steel Constr.*, 7(3), 204–207. <https://doi.org/10.1002/stco.201410027>
- [14] Bedon, C. and Louter, C. (2016), “Finite-element analysis of post-tensioned SG-laminated glass beams with mechanically anchored tendons.”, *Glass Struct Eng*, 1, 39–59. <https://doi.org/10.1007/s40940-016-0020-7>.
- [15] Cupac, J., Martens, K., Nussbaumer, A. et al. (2017), “Experimental investigation of multi-span post-tensioned glass beams.”, *Glass Struct Eng*, 2, 3–15. <https://doi.org/10.1007/s40940-017-0038-5>.
- [16] Ugural AC, Fenster SK. *Advanced Strength and Applied Elasticity*. 4th ed. New Jersey: Prentice Hall; 2003, p. 160-161.

6 Şubat 2023 Depremleri ve Saha Gözlemlerine Dayalı Bina Hasarları Hakkında Ön Değerlendirme

Cem YENİDOĞAN¹



ÖZ

6 Şubat 2023 depremleri geniş bir coğrafyada hissedilmesi ve yaratmış olduğu yıkım ile son yüzyılın en yıkıcı depremleri arasında yerini almıştır. 6 Şubat depremlerinde oluşan karmaşık kaynak özellikleri, deprem kayıtlarının karakterizasyonu, afet bölgesi ilan edilen 11 şehir için yürütülen hasar tespiti çalışmaları mühendisler için çok önemli veriler barındırmaktadır. Hazırlanan bu çalışmanın amacı depremin ikinci gününden itibaren periyodik bir şekilde afet bölgesi ilan edilen 11 ilde saha gözlemleri özelinde 6 Şubat depremlerinin sismo-tektonik, güçlü yer hareketi kayıtlarının özellikleri, binalarda ortaya çıkan hasar dağılımı ve karakteristik özellikleri hakkında bulguları paylaşmaktır. Depremden etkilenen bölgede ağır hasarın yoğunlaştığı illerde elde edilen verilere yönelik tespitler bu çalışma kapsamında kısaca açıklanmaya çalışılmıştır. Derlenen veriler yetkili kurumlar tarafından paylaşılan raporlar, duyurular ve yürürlükte olan deprem yönetmeliği dikkate alınarak bölgede hakim olan bina tipi mevcut yapı envanterinden faydalanarak elde edilmiştir. Kırsal kesimde ve şehir merkezlerinde hasar dağılımı incelendiğinde tescilli kültür varlığı statüsündeki yığma binalar dışında hakim yapısal sistemin şehir merkezlerinde mühendislik hizmeti almış, orta yükseklikte betonarme binalar olduğu, kırsal kesimde ise mühendislik hizmeti almamış, az katlı betonarme, karma veya yığma tipi binalar olduğu belirlenmiştir. Hasar tespitinde geçmiş deneyimlerle kıyaslandığında akademisyenler tarafından verilen eğitimlere katılmış olan saha ekiplerinin göreceli olarak daha hızlı ve titiz bir çalışma ortaya koydukları görülmüştür. Geleneksel binalara ek olarak hastane binalarına yönelik çalışmalarda deprem yönetimi uygulanmış binalar ve geleneksel binaların kıyaslanması bir sistematik içerisinde gerçekleştirilmiştir.

Anahtar Kelimeler: 6 Şubat 2023 depremleri, hasar gözlemleri, Türk Bina Deprem Yönetmeliği, hastane hasarları, afet yönetimi, 6 Şubat 2023 deprem kayıtları.

Not: Bu yazı

- Yayın Kurulu'na 2 Ağustos 2023 günü ulaşmıştır. 6 Mayıs 2024 günü yayımlanmak üzere kabul edilmiştir.
- 30 Kasım 2024 gününe kadar tartışmaya açıktır.

• <https://doi.org/10.18400/tjce.1335742>

1 Yıldız Teknik Üniversitesi, İnşaat Mühendisliği Bölümü, İstanbul, Türkiye
cem.yenidogan@yildiz.edu.tr - <https://orcid.org/0000-0001-9842-3607>

ABSTRACT

February 6, 2023 Earthquakes and Preliminary Assessment of Building Damage Based on Field Surveys

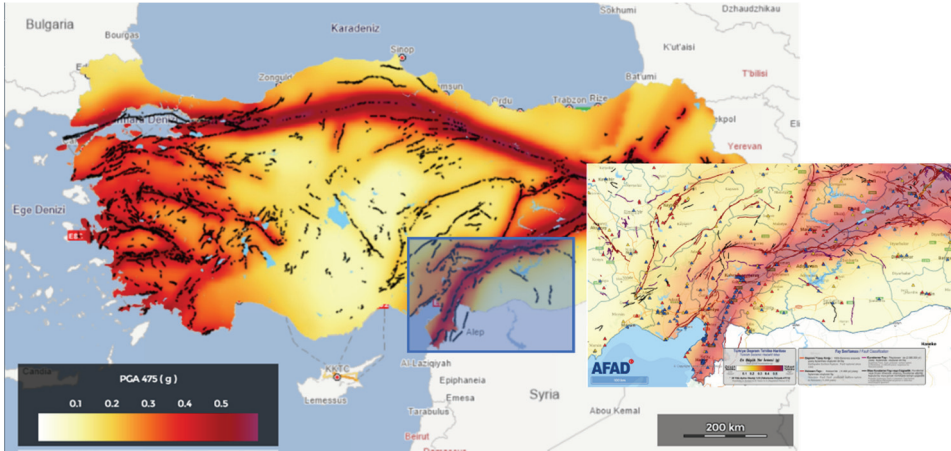
February 6 earthquakes have taken its place among the most destructive earthquakes of the last century, due to extend of the damage, complexity of the source mechanism and being felt in a wide geography. Eleven cities were declared as disaster region by the administration. The source mechanism of the 6 February earthquakes, the characterization of earthquake records, and the rapid damage assessment carried out for 11 cities in the disaster area offers important findings and valuable data for engineering society. The aim of this study is to share the preliminary findings about the seismo-tectonic, strong ground motion characteristics of the earthquake records of the 6 February 2023 earthquakes and the building damage observation. Provinces that were declared as disaster region is periodically visited since the second day of the earthquake. The strong ground motion data obtained in the heavily damaged region have been tried to be explained briefly within the scope of this study. The compiled data were obtained by making use of the existing building inventory of the building type prevailing in the region, considering the reconnaissance trips of the author, institutional reports, press releases of the authorized institutions. When the damage distribution of city centers is examined, it is determined that the dominant structural system is medium-rise reinforced concrete buildings that have received engineering service, whereas predominant structural systems were low-rise reinforced concrete, or masonry buildings that have not received engineering service in rural areas. Compared to the past experiences in damage assessment, it has been observed that the field survey teams, who participated in the training given by the academicians, performed a relatively more meticulous and rapid work. In addition to traditional residential buildings, the comparison of conventional earthquake-resistant hospital buildings and seismically isolated hospital buildings were examined in a systematic way.

Keywords: February 6, 2023 earthquakes, damage observations, disaster management, hospital damages, Turkish Seismic Design Code for Buildings, February 6, 2023 earthquake records.

1. GİRİŞ

Son yüzyılda Türkiye Cumhuriyeti sınırları içerisinde meydana gelen depremler büyük can ve ekonomik kayıplara neden olmuştur. 6 Şubat 2023 sabaha karşı Türkiye saati ile 04.17 sularında AFAD tarafından Pazarcık merkez üssü olan $M_w=7.7$, Amerika Birleşik Devletleri Jeoloji Araştırmaları Kurumu (USGS) tarafından $M_w=7.8$ büyüklüğünde bildirilen deprem afet bölgesi ilan edilen 11 ilde yüksek can ve mal kayıplarına neden olmuş yıkıcı bir depremdir. Birinci depremin yarattığı yıkıcı etkiler geniş bir coğrafyada hissedilirken, Pazarcık depreminden sadece 11 dakika sonra $M_w=6.6$ büyüklüğünde bir artçı ve birinci depremden yaklaşık olarak dokuz saat sonra (UTC+3 13:24) AFAD tarafından $M_w=7.6$, USGS tarafından $M_w=7.5$ büyüklüğünde olduğu bildirilen ve merkez üssü Kahramanmaraş Elbistan olan ikinci bir deprem can ve mal kayıplarının artışına neden olmuştur. Ardı sıra gerçekleşen depremler, yaşanan maddi ve ekonomik kayıplar dışında depremin ilk gününden itibaren yıkımın büyüklüğüyle orantılı olarak depremden etkilenen geniş bir alanda yürütülecek olan arama-kurtarma faaliyetlerini ve afet yönetimini olumsuz etkilemiştir.

Depremi ilk günlerinde yaşanan kayıpların yüksek sayılara ulaşacağı tahmin edilmesi, sahada görev yapabilecek sınırlı sayıda AFAD personelinin yetersiz kalma riski ve depremlerin etkili olduğu bölgenin genişliği düşünülerek ortaya çıkabilecek koordinasyon aksaklıklarının en aza indirilmesi için 11 il Afet Bölgesi ilan edilerek uluslararası yardım çağrısında bulunulmuştur. Afet Bölgesi ilan edilen 11 ilin coğrafi konumu, güncellenmiş diri fay haritaları [1] ve en büyük yer ivmesi (PGA) cinsinden binalar için tasarım depremi için kullanılan DD-2 deprem yer hareketi seviyesi için geliştirilen 2018 deprem tehlike haritaları Şekil 1’de gösterilmiştir. Kahramanmaraş merkezli meydana gelen deprem çifti ve artçıları sadece Türkiye’de değil, Suriye dahil olmak üzere Irak, Ermenistan, Mısır, İsrail, Kıbrıs, Yunanistan, Ürdün, Lübnan gibi çevre ülkelerde de hissedilmiştir. Belirtilen ülkeler arasında Suriye ise Türkiye’ye komşu ülkeler arasında yüksek can kaybının yaşandığı diğer bir ülke olmuştur. 6 Şubat deprem çiftinden sonra bölgenin artan sismik aktivitesinin tetiklediği 20 Şubat 2023 tarihinde üçüncü ayrı bir deprem olarak Yayladağı depremi meydana gelmiştir. 6 Şubat-6 Mayıs 2023 tarihleri arasında ana şok olarak tabir edilen üç depremin merkez üssü, odak mekanizmaları ile bölgede meydana gelen artçıların dağılımı Şekil 2’de gösterilmiştir.



Şekil 1 - Afet bölgesi ilan edilen bölgenin PGA cinsinden Standart Tasarım Deprem Yer Hareketi düzeyi (DD-2 seviyesi) için kullanılan deprem tehlike haritası ve bölgede bulunan AFAD deprem istasyonlarının yerleri (<https://tdh.afad.gov.tr/>)

31 Aralık 2022 tarihli güncellenmiş resmi Adrese Dayalı Kayıt Sistemi (ADNKS) verilerine göre bölgede toplam 14.013.196 kişi yaşamaktadır. Bölgede yer alan ve afet bölgesi ilan edilen üç şehrin demografik yapısı Çizelge 1’de gösterilmiştir. Türkiye sınırları içerisinde üç deprem ile artçılarının sonucu olarak İçişleri Bakanı Ali Yerlikaya’nın 2 Şubat 2024 tarihinde yapmış olduğu basın açıklaması doğrultusunda toplam can kaybının 53.537 kişiye, yaralı sayısının 107.213 kişiye ve yıkılan bina sayısının ise 37.984 ulaştığı teyit edilmiştir. Suriye sınırları içinde ise ölü sayısının 7000 kişinin üzerinde olduğu belirtilmektedir. Belirtilen 60.000 kişinin üzerinde yaşanan can kaybı ile sonuçlanan depremler son yüzyıllık süreçte deneyimlenmiş ve derin yaralar açan Kuzey Anadolu Fay hattında meydana gelmiş 1939

Erzincan, 1999 Gölcük, 2011 Van Depremleri ile 2020 yılında Doğu Anadolu fay hattı üzerinde yaşanan Elazığ depremlerinin çok üzerinde bir yıkıma neden olmuştur. Yıkımlar afet bölgesi ilan edilen 11 ilde yaşayan toplam 14013196 kişinin hayatını olumsuz etkilemiştir. Türkiye Cumhuriyeti Cumhurbaşkanlığı Strateji ve Bütçe Başkanlığı tarafından hazırlanan Kahramanmaraş ve Hatay Depremleri Raporunda sigortacılık sektörü ve makroekonomik ölçekte ekonomik kaybın 103.6 milyar dolar olarak tahmin edildiği raporlanmıştır [2].

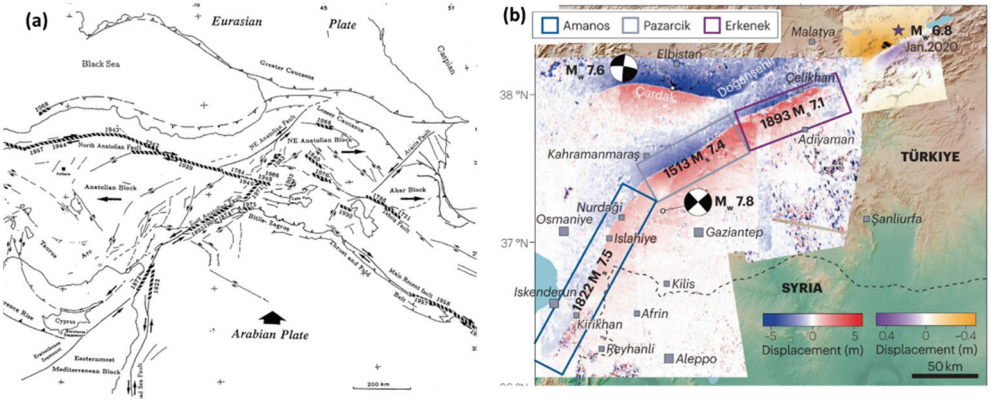
Çizelge 1 - 2022 ADNKS verilerine göre Afet Bölgesinde nüfus ve yaş dağılımı

İl	Toplam	(0-17)	(15-24)	(15-29)	(0-29)	(15-64)	65+
Adana	2.274.106	650.919	337.196	500.939	1.040.186	1.523.411	211.448
Adıyaman	635.169	213.088	104.216	151.927	329.544	404.271	53.281
Diyarbakır	1.804.880	677.944	323.328	479.726	1.051.408	1.140.208	92.99
Elazığ	591.497	152.439	93.264	136.714	262.186	401.774	64.251
Gaziantep	2.154.051	790.077	373.459	543.469	1.206.932	1.366.161	124.427
Hatay	1.686.043	537.008	265.09	382.846	828.626	1.102.478	137.785
Malatya	812.58	215.978	126.831	184.285	361.013	545.21	90.642
Kahramanmaraş	1.177.436	373.637	193.881	278.382	586.363	764.905	104.55
Şanlıurfa	2.170.110	974.864	403.597	580.835	1.414.726	1.246.531	89.688
Kilis	147.919	48.947	27.599	39.283	80.164	95.119	11.919
Osmaniye	559.405	171.036	87.769	125.901	266.411	366.904	51.991
Bölge Toplamı	14.013.196	4.805.937	2.336.230	3.404.307	7.427.559	8.956.972	1.032.972
Erkek	7.049.219	2.461.656	1.196.670	1.731.596	3.792.656	4.524.779	463.38
Kadın	6.963.977	2.344.281	1.139.560	1.672.711	3.634.903	4.432.193	569.592

Bölgede karayolu ve havayolu ulaşım ağlarının hasar görmesi ve yaşanan olumsuz hava koşulları arama-kurtarma faaliyetlerinin ve acil müdahalenin gecikmesi, 72 saatlik kritik sürecin koordinasyonu ve yönetiminde zorluklar yaratmıştır. Bölgede yer alan Hatay havalimanının hasar görmesinden dolayı bölgeye ekiplerin ulaşımı çevre illerde yer alan havalimanları ve karayolu üzerinden öncelikli olarak arama kurtama ekiplerinin ve Çevre Şehircilik ve İklim Değişikliği Bakanlığı tarafından görevlendirilen idari ve akademik personelin kullanımına açılmıştır.

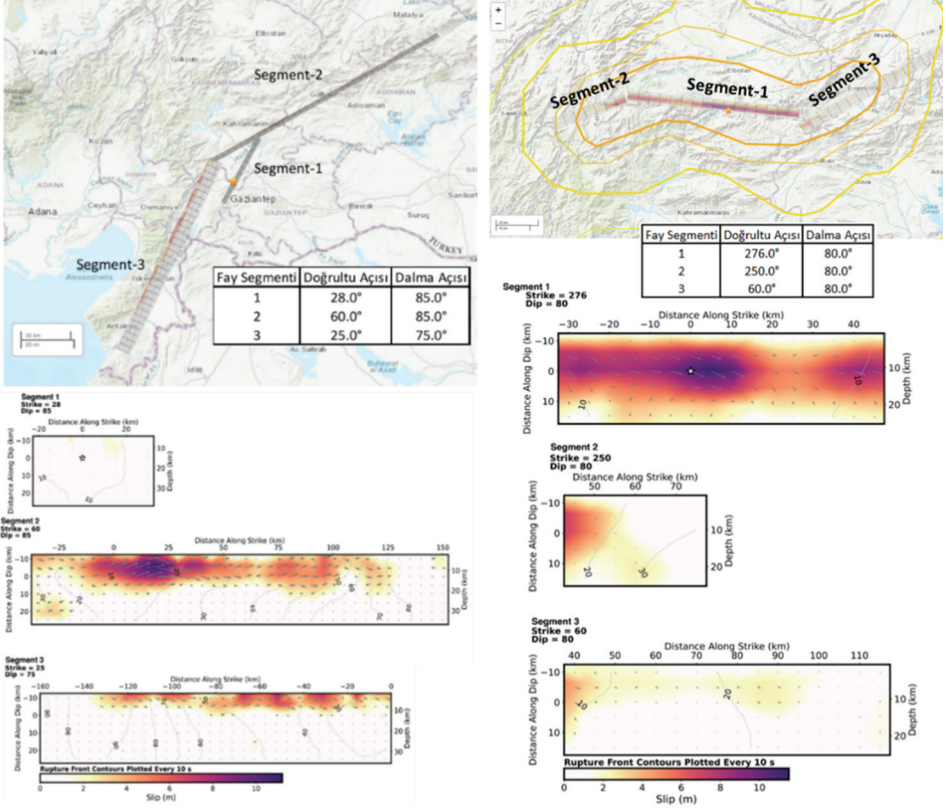
Bu çalışma kapsamında 6 Şubat depremleri sonrasında afet bölgesi ilan edilen illerde sismo-tektonik yapı, AFAD istasyonlarından elde edilen güçlü yer hareketi kayıtlarının, binalarda ortaya çıkan hasar dağılımı ve hasarın karakteristik özellikleri saha gözlemlerinden elde edilen bulgular yardımı ile paylaşılmaktadır. Bina hasarlarına yönelik olarak bölgede yer alan konutlar, iş yerleri, hastaneler, kültür varlığı statüsünde olan binalar ve endüstriyel yapılar saha gözlemleri özelinde incelenmiştir. Aynı gün içerisinde meydana gelen Pazarcık ve Elbistan merkez üslü iki depremin çok kısa süre aralığında olması iki depremin farklı etkilerinin bina hasarları açısından kayıt altına alınmasını engellemiştir. Bina hasarları ile

Doğu Anadolu Fay zonunun içerisinde yer alan segmentler ve mekanizması ile ilgili birçok araştırmacı tarafından detaylı çalışmalar gerçekleştirilmiştir [5-16]. Derlenen deprem katalog çalışmalarında sismik boşluktan dolayı bölgede büyük bir deprem tehlikesi altında olduğu birçok araştırmacı tarafından bilinmekteydi. Sismik tehlike çalışmaları için derlenen tarihsel depremler, bölgenin büyük deprem üretme potansiyeline sahip olduğu görüşünü desteklemekteydi. Tarihsel depremler arasında yüzey dalgası büyüklüğü olarak $M_s=7.4$ olan 1513 Türkoğlu, $M_s=7.5$ olan 1822 Halep, $M_s=7.2$ olan 1872 Amik gölü depremi ve son olarak 1893 Malatya depremleri yer almaktadır [13-15]. Fakat tahmin senaryolarında ortaya çıkabilecek çoklu yırtılmaya bağlı en kötü senaryolardan bir tanesi şehir bazlı deprem kaybı kestirim çalışmalarında dikkate alınmamıştır. AFAD-RED tarafından hazırlanmış olan Kahramanmaraş Deprem Kayıp ve tahmin senaryosunda ön görülen rakamlar ve deprem büyüklüğü meydana gelen Pazarcık depreminin altında kalan rakamları işaret ediyordu.

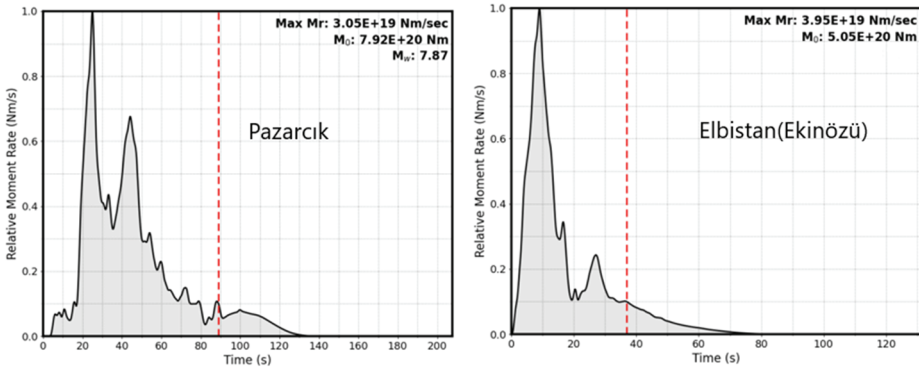


Şekil 3 - (a) Pazarcık ve Elbistan depremlerinin meydana geldiği deprem bölgesi ve tektonik levhalar [10-12] (b) tarihsel depremlerin yıllara göre dağılımı [17]

6 Şubat depremlerinde karmaşık deprem kaynak özelliklerine sahip olmasının nedenlerinden bir tanesi aynı anda çoklu fay kırıklarının oluşmasıdır. Ayrıca yırtılmanın her iki yönde farklı yayılım özellikleri göstermesi deprem kayıtlarında yakın saha özelliklerine yansımıştır. Fayın taban ve tavan bloklarında deprem yer hareketleri hız zaman tanım alanında çizdirildiğinde itkiler kolaylıkla gösterilebilmektedir. Bu durum mevcut deprem senaryolarından farklı bir büyüklükte bir deprem ve geniş bir bölgede büyük bir yıkım ortaya çıkarmıştır. 6 Şubat 2023 Pazarcık ve Elbistan depremlerinin sonlu fay modeli bölgede yer alan ivme ölçerler, GPS cihazları ve telesismik verilerden faydalanarak yapılan güncellemeler, depremin ilk haftalarında kaynak mekanizması hakkında bilgiler sağlamıştır (Şekil 4). Elde edilen sonlu fay modelinden depremin etkin süresi güçlü yer hareketi kayıtlarını destekleyecek bilgiler sunmaktadır (Şekil 5). Ayrıca elde edilen uzun süreli deprem kayıtları yazarın saha incelemelerinde elde ettiği kamera görüntülerinde de doğrulanmaktadır.

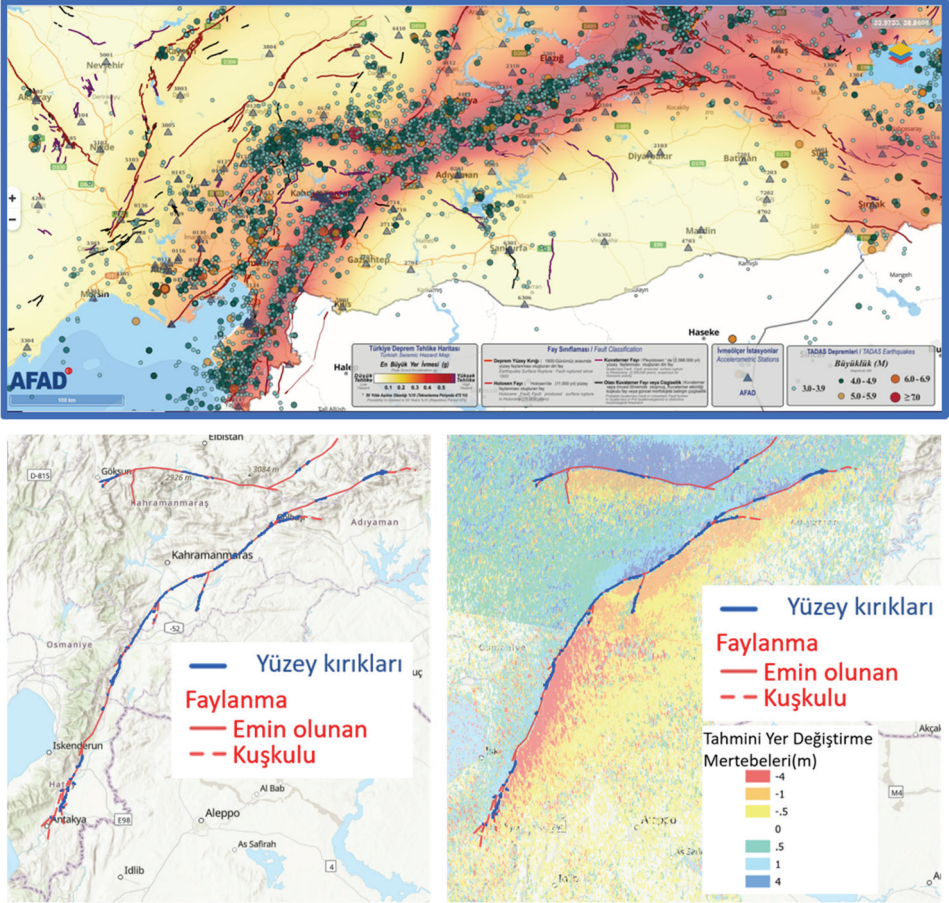


Şekil 4 - Pazarlık ($M_w=7.8$) ve Elbistan merkez üslü ($M_w=7.5$) sonlu fay modelleri (USGS, (<https://earthquake.usgs.gov>), son güncelleme tarihi, 2023-02-21 03:47:31 (UTC))



Şekil 5 - USGS tarafından yürütülen sonlu fay modellerinden elde edilen kaynak özellikleri (<https://earthquake.usgs.gov>), son güncelleme tarihi 2023-02-21 03:47:31 (UTC))

Gelişen teknoloji ile birlikte uydu görüntüleri ve mevcut araçlar kullanılarak aktif fay izi ve yüzey kırıklarının dağılımları Kahramanmaraş depremleri sonrasında görüntülenebildiler. AFAD tarafından fay kırıkları ve bölgede küçük ölçekli depremler ile birlikte meydana gelen tüm artçılar Şekil 6'da gösterilmiştir[18].



Şekil 6 - (a) Haritalandırılmış fay kırıkları ve oluşan depremlerin büyüklükleri (<https://tadas.afad.gov.tr/>) (b) 6 Şubat 2023 depremleri sonrasında tespit edilen yüzey kırıkları ve tahmini yer değiştirme mertebeleri (<https://usgs.maps.arcgis.com/apps/webappviewer/index.html?id=5229bb842bd64b688d769abbefe43b46>)

Üç ana depremin ve büyüklüğü 5.5 ve üzeri olan artçı depremlerin listesi Çizelge 2'de verilmiştir.

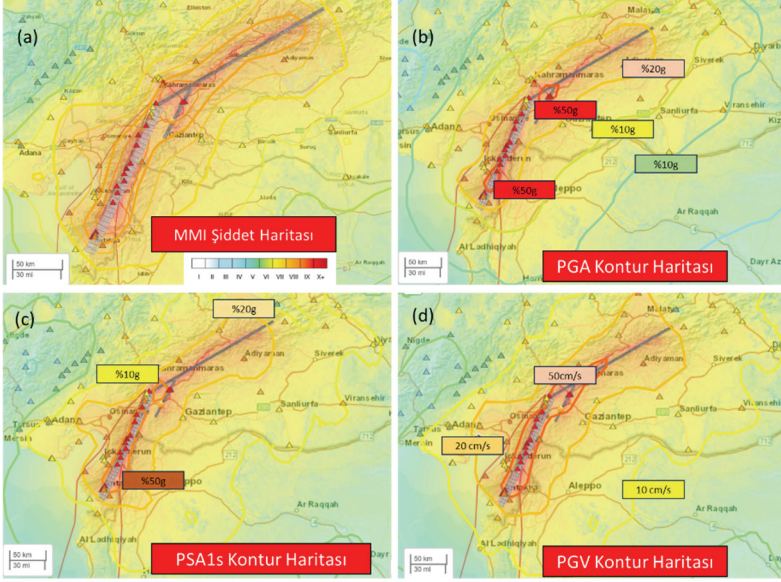
Çizelge 2 - Afet bölgesinde üç ana deprem ve büyüklüğü 5.5 üzeri olan artçı depremlerin listesi[18]

Tarih ve Zaman (UTC)	Epicenter (İlçe/ İl)	Büyüklik Mw/ML)	Derinlik
6 Şubat 2023, 01:17:32	Pazarcık / Kahramanmaraş	7.7	8.6
6 Şubat 2023, 01:26	Nurdağı / Gaziantep	5.6	6.98
6 Şubat 2023, 01:28	Nurdağı / Gaziantep	6.6	6.2
6 Şubat 2023, 01:36	İslahiye / Gaziantep	5.7	11.19
6 Şubat, 2023, 02:03	Doğanşehir / Malatya	5.6	10.23
6 Şubat 2023, 10:24:47	Elbistan / Kahramanmaraş	7.6	7
6 February 2023, 10:26	Yeşilyurt / Malatya	5.8	6.89
6 February 2023, 10:32	Ekinözü / Gaziantep	5.5	10.93
6 February 2023, 20:37	Pazarcık/Kahramanmaraş	5.5	5.96
20 February 2023, 17:04	Yayladağı / Hatay	6.4	21.73
20 February 2023, 17:04	Samandağ / Hatay	5.8	6.64
27 February 2023, 09:04	Yeşilyurt / Malatya	5.6	6.15

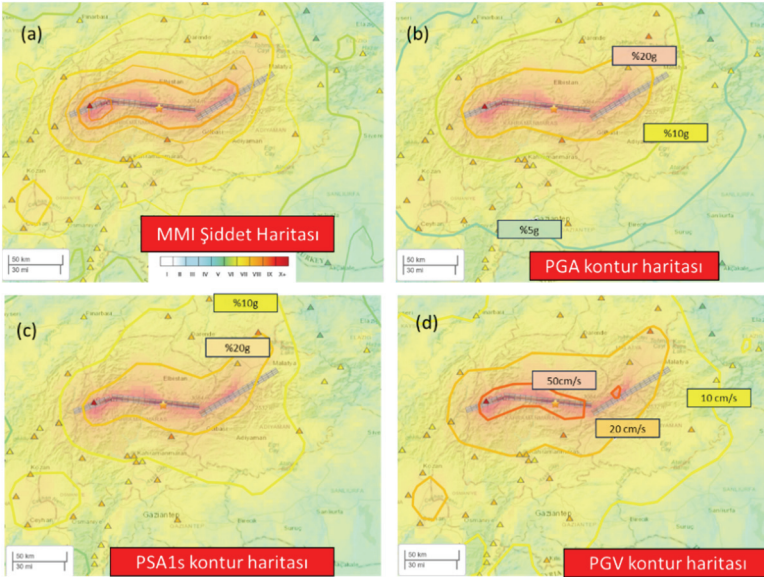
3. DEPREMLERDEN ELDE EDİLEN YER HAREKETİ KAYITLARI VE HASAR DAĞILIMININ TAHMİNİNDE KULLANILAN HARİTALAR

AFAD Türkiye’de meydana gelen depremlerin ölçülmesi ve kayıt altında tutulması amacı ile geniş bir kuvvetli yer hareketi ağı oluşturarak, depremlerden sonra elde edilen ham ve işlenmiş deprem kayıtlarını bilimsel çevreler ve mühendislik camiası ile paylaşmaktadır. Kahramanmaraş depremlerinden sonra elde edilen deprem kayıtlarının paylaşımı, geniş bir alanı etkileyen depremler sonrası yapısal hasarın kestirimi açısından önemli katkılar sağlamıştır. Pazarcık depreminde kayıt istasyonlarının MMI şiddet haritasında dağılımı incelendiğinde bina hasarlarının yoğunlaştığı bölgelerde uyumlu olarak haritalandırılmış oldukları görülmektedir (Şekil 7, Şekil 8). Şiddet haritasında 6 Şubat 2023 Pazarcık depremi sonrasında Antakya merkezde 9.3 MMI şiddeti seviyelerine ulaşan değerler elde edilmiştir ve 6 Şubat Elbistan depremlerinde benzer şekilde Göksun civarında bu değerler MMI şiddeti cinsinden 9.2 seviyelerine ulaşmaktadır [19]. Benzer şekilde yazarın içerisinde bulunduğu araştırma ekibi tarafından geliştirilen ve Türkiye’de farklı kurumlar tarafından kullanılan ELER adlı program kullanılarak benzer sarsıntı haritaları da elde edilebilmektedir[20].

2018 yılında hazırlanan ve 2019 yılında yürürlüğe giren Türkiye Bina Deprem Yönetmeliği (TBDY-2018) için yenilenen deprem tehlike haritası ve Maden Tetkik Arama tarafından güncelenen diri fay haritası dikkate alınarak deprem istasyonlarının yerleri bölgenin depremselliğinin irdelenmesinde kullanılmıştır [5]. Deprem istasyonlarının yerel zemin koşullarına elde edilen elastik tasarım spektrumları Hatay, Kahramanmaraş ve Gaziantep illeri özelinde dikkate alınarak, deprem kayıtlarının davranış spektrumlarıyla kıyaslamalı olarak paylaşılmıştır. Fakat her iki depremden elde edilen deprem kayıtlarının sayısının oldukça fazla olmasından dolayı bu çalışma kapsamında 6 Şubat Pazarcık depreminde ağır hasarlı bina sayısının yüksek olduğu il ve ilçelerden seçilen sınırlı sayıda işlenmiş deprem



Şekil 7 - Merkez üssü Pazarcık ($M_w=7.8$) olan deprem sonrasında hesaplanan (a)MMI şiddet haritası, (b) PGA kontur haritası, (c) PSA1 kontür haritaları ve (d) PGV kontur haritası (<https://earthquake.usgs.gov>)[19]

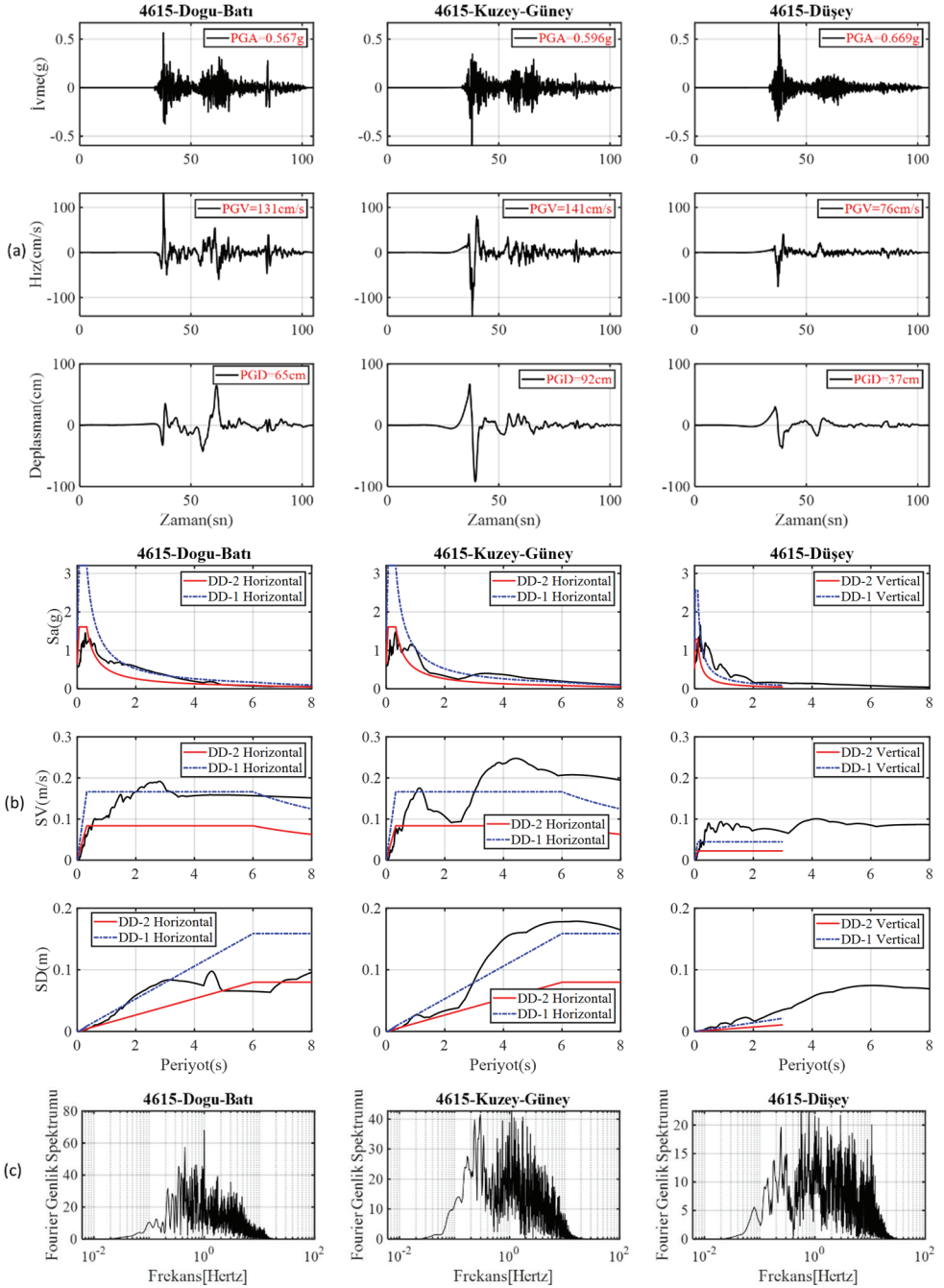


Şekil 8 - Merkez üssü Elbistan ($M_w=7.5$) depreminde güçlü yer hareketi istasyonlarının konumu ve hesaplanan (a) MMI şiddet haritası (b) PGA kontur haritası (c) Psalın için kontur (d) PGV kontur haritaları (<https://earthquake.usgs.gov>)[19]

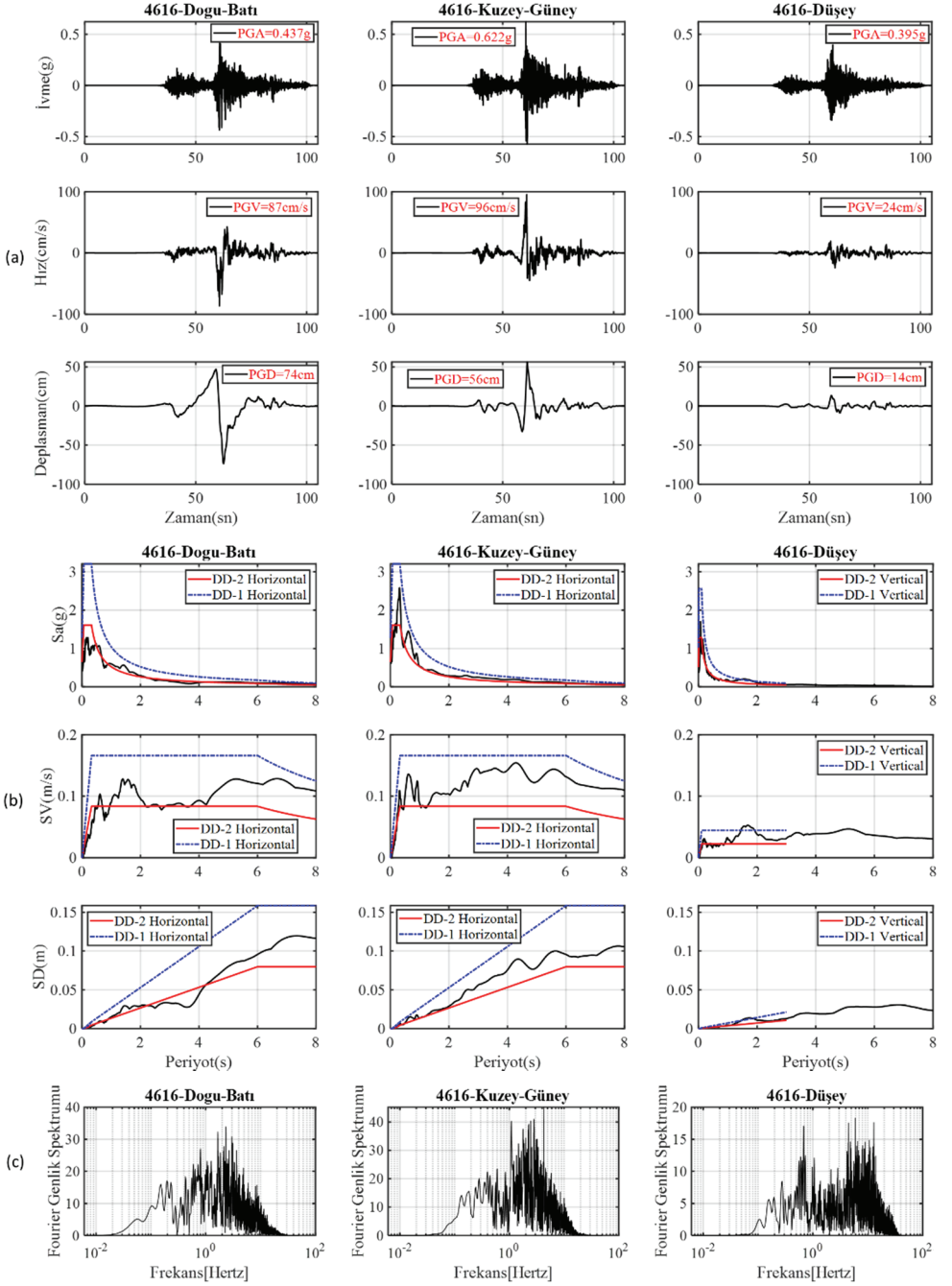
kayıtları kullanılarak güçlü yer hareketi parametreleri hesaplanmıştır. Yer hareketi kayıtlarının özellikleri zaman tanım alanında ve frekans tanım alanında gösterilmiştir. Deprem bölgesinde ağır hasar alan iller arasında yer alan Kahramanmaraş ilinde Pazarcık ve Türkoğlu istasyonları, Hatay ilinde yer alan Antakya, Hassa ve Kırıkhan istasyonlarının verileri ve Gaziantep ilinde yer alan Nurdağı, İslahiye istasyonlarının deprem kayıtları yıkımın şiddetini yansıtabilmesi için bu bölümde paylaşılmıştır (Şekil 9-18). Deprem kayıtlarının üç güçlü yer hareketi parametreleri Çizelge 3'te listelenmiştir. AFAD deprem istasyonlarından elde edilen AFAD tarafından işlenmiş olarak kullanıcılara sağlanan deprem kayıtları kullanılmıştır. Deprem kayıtlarının 6 Şubat Pazarcık depremi dikkate alındığında merkez üssüne olan uzaklıkları, yerel zemin koşulları, ve filtrelemede kullanılan bant aralığı ve filtre tipi Çizelge 3'te gösterilmiştir. Bütün kayıtlar için 17 farklı güçlü yer hareketi parametresi hesaplanmıştır. Hesaplanan 17 parametre arasında hasar durumunu yansıtanları seçilerek Çizelge 4'te listelenmiştir. Sunulan PGA ve PGV değerleri jeoteknik mühendisliğin ilgi alanında olan altyapı elemanlarında ortaya çıkacak hasar ve kayıp kestiriminin olasılıksal olarak hesaplanmasında kullanılmaktadır.

Güçlü yer hareketi parametrelerinden en büyük yer hızı (PGV) değeri deprem tehlike haritalarında hesaplanmasına rağmen bu parametre tasarım aşamasında Türk Deprem Yönetmeliğinde dikkate alınmamaktadır. Hasar kestiriminde yapısal özelliklere bağlı olarak en büyük yer hızı parametresinin (PGV) ilerleyen süreçlerde sünek taşıyıcı elemanların davranışında dikkate alınması, yazarın kişisel fikrine göre önemli katkılar sağlayacaktır. 6 Şubat deprem çifti incelenirken alışılmış yakın saha kaynak parametrelerinden olan yönelim (Direktivite), ve atım (Fling step) diye adlandırılacak yakın saha parametreleriyle kıyaslandığında tasarım mühendisleri tarafından süneklik taleplerine yönelik çalışmalarda bir girdi parametresi olarak kolaylıkla kullanılabilecektir. Hasar ve sünekliği dair benzer bulgular yazar tarafından gerçek ölçeklerinde test edilmiş yapısal ve yapısal olmayan sistemlerin performans değerlendirmesi için yürütülen sarsma masası testlerinde perde duvar ve yapısal olmayan eleman hasarlarında etkin rol oynamıştır [21]. 6 Şubat 2023 deprem çiftinin kayıtlarından elde edilen PGV değerleri deprem tehlike haritalarında ön görülen PGV değerleriyle kıyaslama yapma olanağı sunmaktadır. PGV değerleriyle ilgili Japon yönetmeliğinde yer alan tasarım kriterlerine atfen yapıların sünek tasarlanan elemanlarında ortaya çıkabilecek hasarlar hakkında fikir verebilmektedir. Deprem bölgesi incelendiğinde deprem yönetmeliğinde yer alan Seviye 1 ve Seviye-2 spektrumu hız değerleri ile uyumlu PGV kontur haritaları ortaya çıkmıştır.

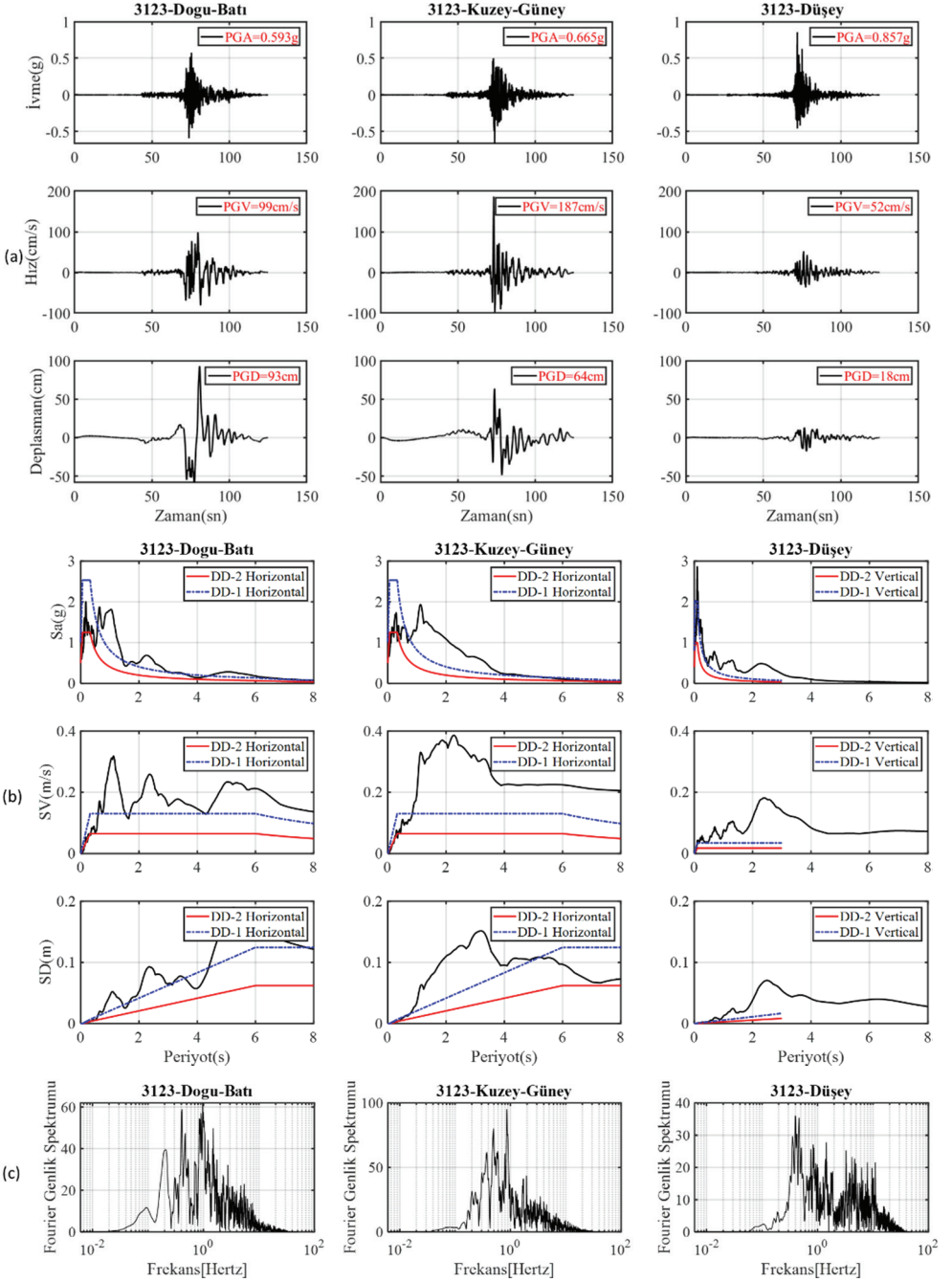
AFAD tarafından işlenmiş veriler kullanılarak spektral ivme, spektral hız ve spektral deplasman değerleri Türkiye Bina Deprem Yönetmeliğinde yer alan DD-1 ve DD-2 deprem yer hareketi düzeyleri için elde edilen tasarım spektrumları ile kıyaslanmıştır. Deprem kayıt istasyonlarından 4615 Pazarcık, 2712 nolu Nurdağı istasyonu deprem kayıtları spektral ivmeler cinsinden incelendiğinde DD-1 deprem yer hareketi seviyesini her üç bileşen için de belirli aralıklarla aştığı gözlemlenmiştir. Ağır hasarlı binalar ve toptan göçmenin yoğun gözlemlendiği Antakya il merkezinde 3123 Antakya istasyonu incelendiğinde spektral ivme, spektral hız ve spektral deplasman değerlerinin aşıldığı gözlemlenmiştir. Benzer çıkarımlar 3143 nolu Hatay Kırıkhan istasyonu içinde geçerlidir.



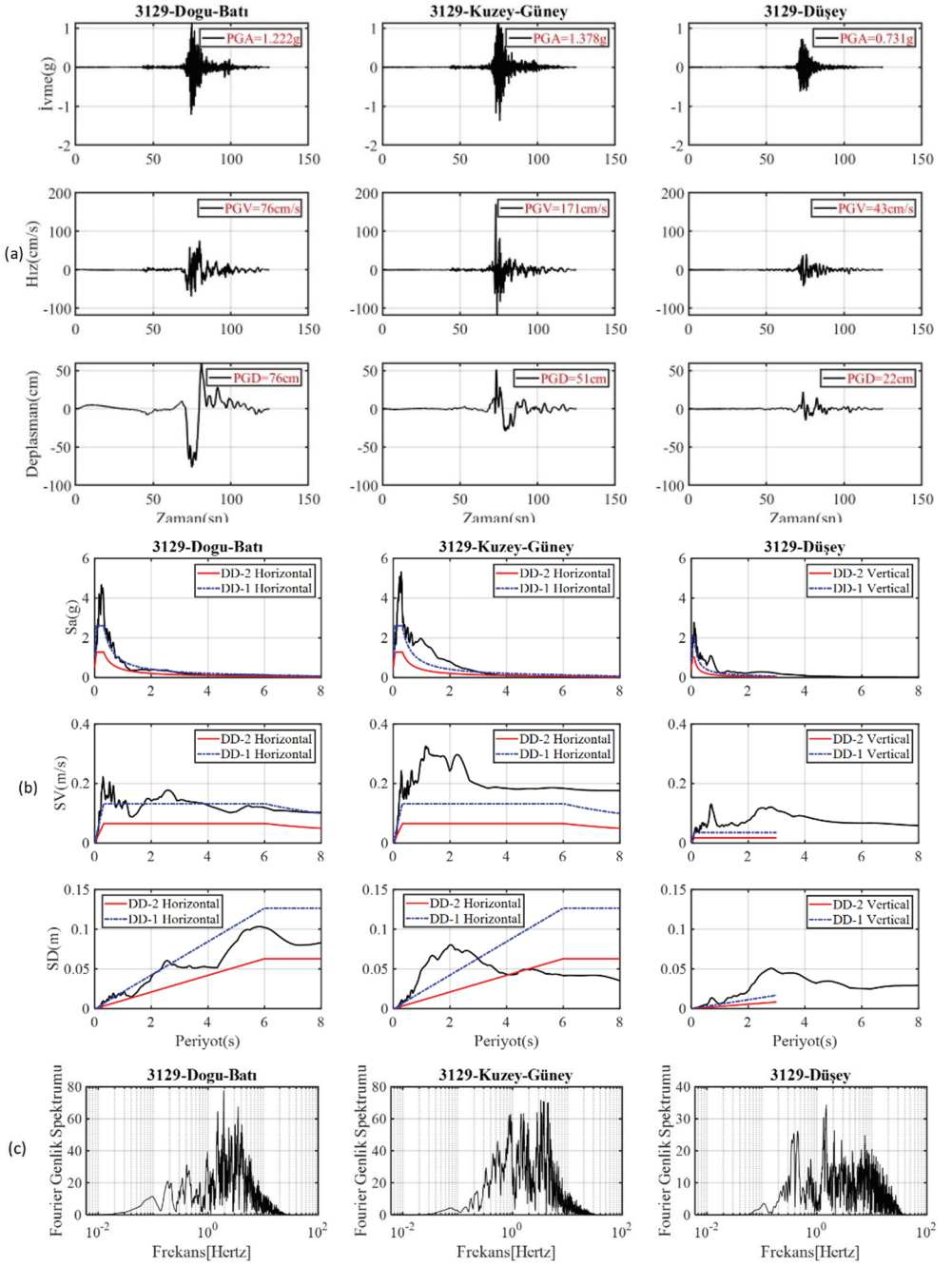
Şekil 9 - 4615 Pazarcık İstasyonu (a) İvme-Hız-Deplasman zaman tarihçesi (b) Sa-Sv-Sd Davranış Spektrumu (c) Frekans içeriği



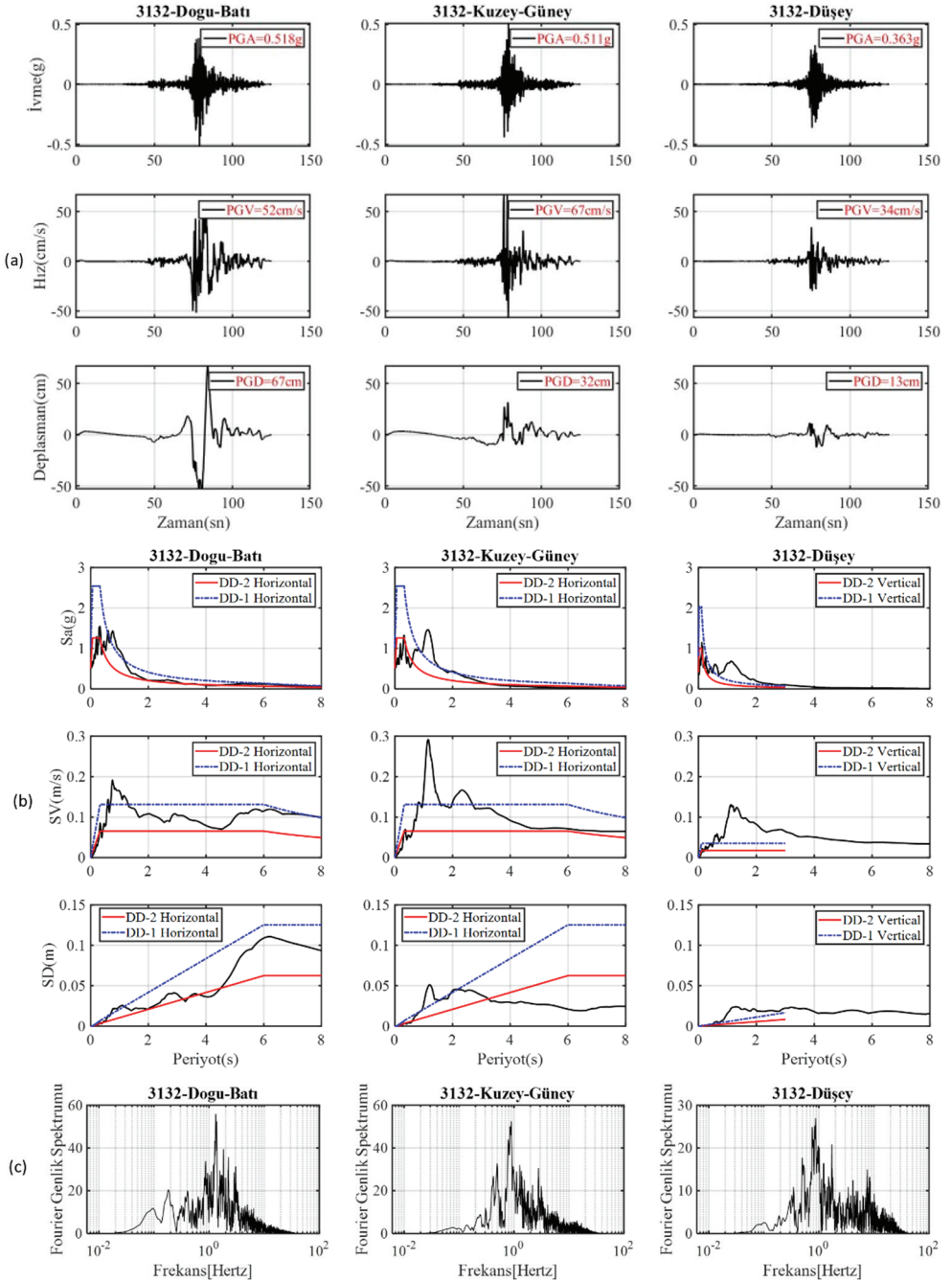
Şekil 10 - 4616 Türkoğlu istasyonu (a) İvme-Hız-Deplasman zaman tarihçesi (b) Sa-Sv-Sd Davranış Spektrumu (c) Frekans içeriği



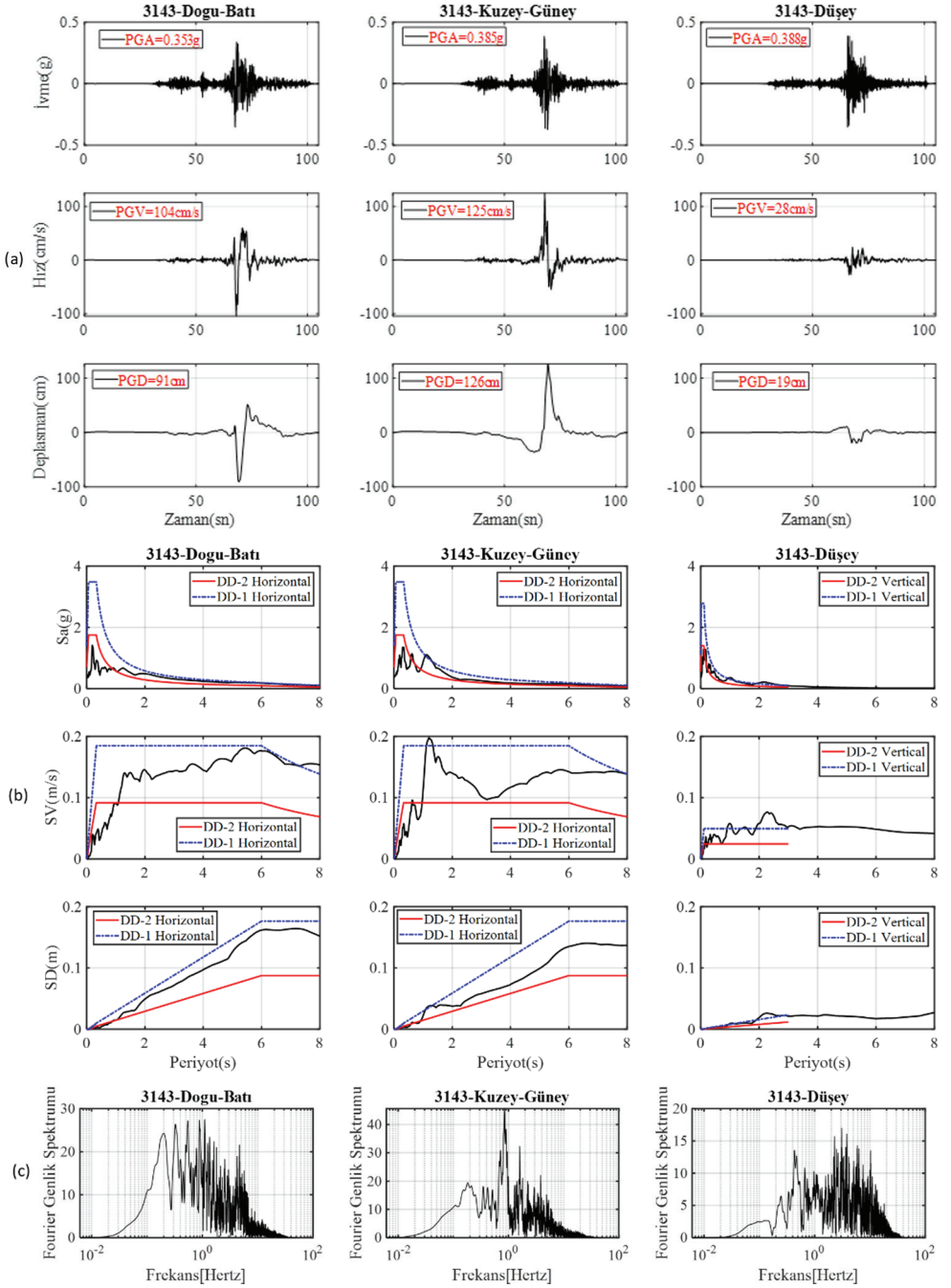
Şekil 11 - 3123 Antakya istasyonu (a) İvme-Hız-Deplasman zaman tarihçesi (b) Sa-Sv-Sd Davranış Spektrumu (c) Frekans içeriği



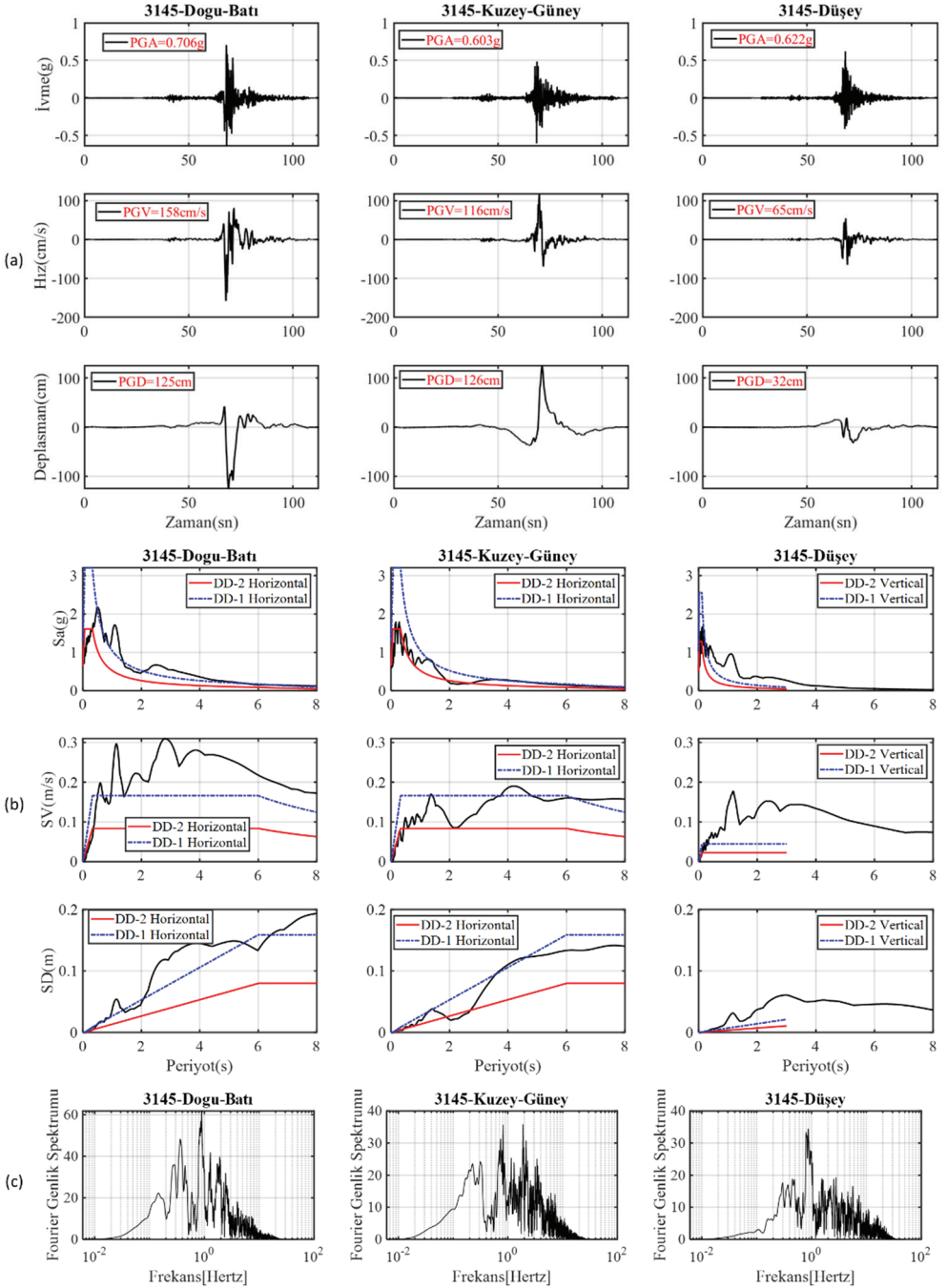
Şekil 12 - 3129 Hatay Defne istasyonu (a) İvme-Hız-Deplasman zaman tarihçesi (b) Sa-Sv-Sd Davranış Spektrumu (c) Frekans içeriği



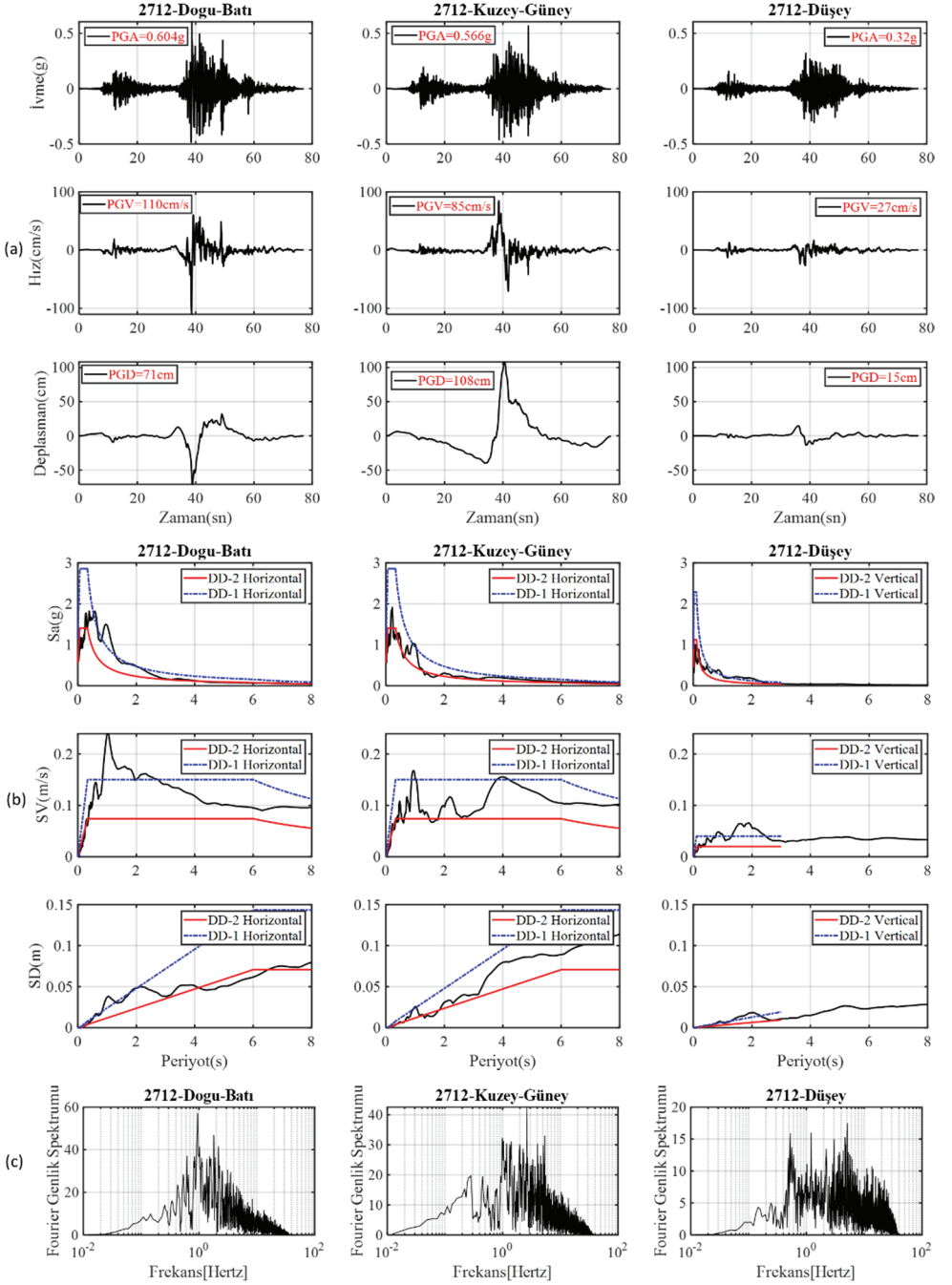
Şekil 13 - 3132 Antakya istasyonu (a) İvme-Hız-Deplasman zaman tarihçesi (b) Sa-Sv-Sd Davranış Spektrumu (c) Frekans içeriği



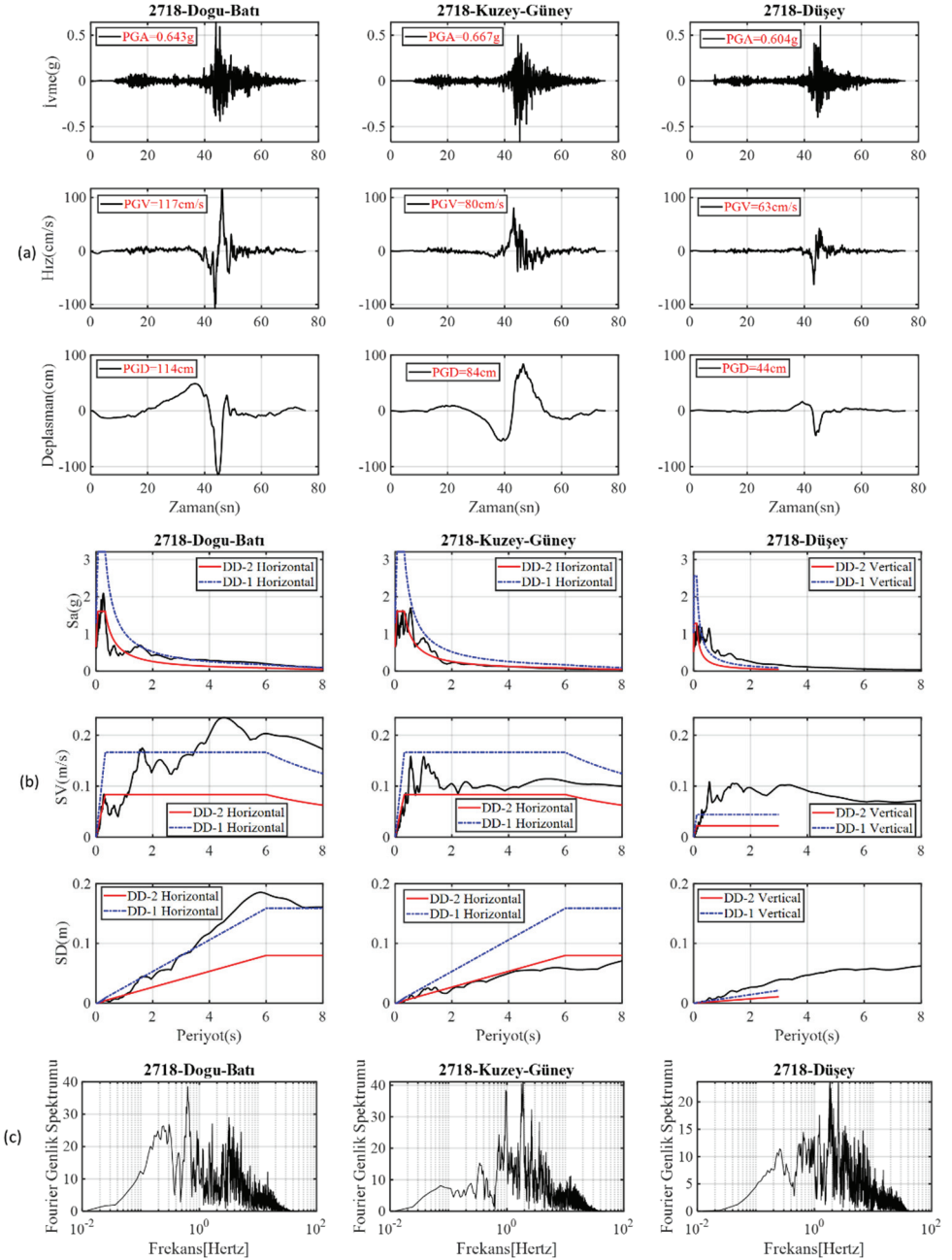
Şekil 14 - 3143 Hassa istasyonu (a) İvme-Hız-Deplasman zaman tarihçesi (b) Sa-Sv-Sd Davranış Spektrumu (c) Frekans içeriği



Şekil 15 - 3145 Kırıkhan istasyonu (a) İvme-Hız-Deplasman zaman tarihçesi (b) Sa-Sv-Sd Davranış Spektrumu (c) Frekans içeriği



Şekil 16 - Gaziantep 2712 Nurdağı istasyonu (a) İvme-Hız-Deplasman zaman tarihçesi (b) Sa-Sv-Sd Davranış Spektrumu (c) Frekans içeriği



Şekil 17 - Gaziantep 2718 İslahiye istasyonu (a) İvme-Hız-Deplasman zaman tarihçesi (b) Sa-Sv-Sd Davranış Spektrumu (c) Frekans içeriği

Çizelge 3 - İncelenen deprem kayıtlarının alındığı istasyonlar için elde edilen Vs30 kayma dalgası hızı, merkez üssüne olan uzaklık ve filtre tipi, mertebesi ve filtreleme bant aralıkları

AFAD Deprem İstasyonu Kodu	Enlem	Boylam	Repi Uzaklık (km)	Filtre Tipi	Mertebe	L-Cut Freq (Hz)	H-Cut Freq (Hz)	Vs30 (m/s)
4615-Doğu-Batı	37.138	37.387	13.83	Butterworth	2	0.026	15.01	484
4615-Kuzey-Güney				Butterworth	2	0.057	13.94	484
4615-Düşey				Butterworth	2	0.045	18.72	484
4616-Doğu-Batı	36.838	37.375	20.54	Butterworth	2	0.025	22.26	390
4616-Kuzey-Güney				Butterworth	2	0.057	19.21	390
4616-Düşey				Butterworth	2	0.070	34.68	390
3123-Doğu-Batı	36.160	36.214	143	Butterworth	1	0.025	40.00	470
3123-Kuzey-Güney				Butterworth	1	0.025	40.00	470
3123-Düşey				Butterworth	1	0.025	40.00	470
3129-Doğu-Batı	36.134	36.191	146.39	Butterworth	2	0.018	23.97	447
3129-Kuzey-Güney				Butterworth	2	0.033	27.79	447
3129-Düşey				Butterworth	2	0.055	34.68	447
3132-Doğu-Batı	36.172	36.207	143.12	Butterworth	1	0.025	40.00	377
3132-Kuzey-Güney				Butterworth	1	0.025	40.00	377
3132-Düşey				Butterworth	1	0.025	40.00	377
3143-Doğu-Batı	36.557	36.849	65.13	Butterworth	1	0.025	40.00	444
3143-Kuzey-Güney				Butterworth	1	0.025	40.00	444
3143-Düşey				Butterworth	1	0.025	40.00	444
3145-Doğu-Batı	36.406	36.645	91.13	Butterworth	2	0.013	20.68	533
3145-Kuzey-Güney				Butterworth	2	0.020	22.82	533
3145-Düşey				Butterworth	2	0.015	30.66	533
2712-Doğu-Batı	36.733	37.184	29.79	Butterworth	2	0.026	35.55	-
2712-Kuzey-Güney				Butterworth	2	0.014	34.68	-
2712-Düşey				Butterworth	2	0.025	35.55	-
2718-Doğu-Batı	36.627	37.008	48.3	Butterworth	2	0.021	34.68	-
2718-Kuzey-Güney				Butterworth	2	0.021	35.55	-
2718-Düşey				Butterworth	2	0.016	37.34	-

6 Şubat 2023 depremleri, çift yönlü yırtılmanın yarattığı yakın saha depremlerinin düşey ivmeler açısından etkileri deprem kayıtlarında kendisini göstermiştir. TBDY-2018 yönetmeliğinde düşey tasarım spektrumu sabit deplasman bölgesinin başladığı kısımdan itibaren değerlendirmeye alınmadığından, düşey yer hareketi ancak tasarım spektrumlarının 3sn değerine kadar çizdirilmiştir. Bu açıdan değerlendirildiğinde AFAD 2708 ve 2718 nolu İslahiye kayıtlarında yüksek yatay ivme değerlerinin sırasıyla yaklaşık olarak %90'ı ve %83'üne karşılık gelmektedir. Yüksek düşey yer ivmelerinin olumsuz etkileri bina hasarlarının yanı sıra prekast endüstriyel yapılarda saha incelemelerinde gözlemlenmiştir.

Bu çalışma kapsamında değerlendirilen bina tipi yapılar düşünüldüğünde spectral ivme değerleri yardımı ile çizilen tasarım spektrumu ve kayıtların davranış spektrumlarının kıyaslanması ise inşaat mühendisleri için 6 Şubat depremlerinin karmaşık yapısı düşünüldüğünde kısıtlı da olsa önemli bulgular sunmaktadır. Tasarım spektrumu değerlerinin DD-2 ve DD-1 seviyelerinde aşılması yaygın kanının aksine doğru bir plan düzeni ve kapasite spektrum prensiplerine göre tasarlandığında toptan göçmenin ortaya çıkmasının yaşanan kayıplara göre daha az olması gerektiğini işaret etmektedir.

Yerin en büyük hız değeri olarak ifade edilen (PGV) ve en büyük yer ivmesi (PGA) değerleri TBDY-2018 yönetmeliğinde lokasyon bazlı elde edilmesine rağmen bina tipi yapıların hiçbir tasarım aşamasında kullanılmamaktadır. Bu açıdan yazar güçlü yer hareketi parametreleri arasında yer alan bu iki parametreyi Avrupa deprem yönetmelikleri ve Japon deprem yönetmelikleriyle bir kıyaslama yapılabilmesi amacıyla Çizelge 4'te sunmuştur. Bir

algoritma eşliğinde daha önce paylaşılan PGV tabanlı sarsıntı haritalarında Japon deprem yönetmeliğinde yer alan ikinci deprem seviyesi olarak tanımlanan tasarım depremi değerine ulaştığı görülmektedir[21].

Çizelge 4 - Güçlü yer hareketi parametreleri

İstasyon	Parametre	'PGA(m/s ²)'	'PGV(cm/s)'	'PGD(cm)'	'Acc. RMS(cm/sec ²)'	'Arias Intensity(m/sec ²)'	'SI(cm)'	'Brack. Duration(sec)'
4615	Doğu-Batı	5.56	131.20	64.60	59.08	5.87	4653.35	32.11
	Kuzey-Güney	5.85	141.10	91.70	57.57	5.57	4475.45	32.11
	Düşey	6.56	75.80	37.40	40.12	2.71	2603.71	32.11
4616	Doğu-Batı	4.29	86.50	73.60	47.10	3.73	3311.96	20.68
	Kuzey-Güney	6.10	95.60	56.40	61.88	6.44	4988.08	20.68
	Düşey	3.88	24.20	13.60	35.38	2.10	2155.83	20.68
3123	Doğu-Batı	5.82	98.70	92.80	61.06	7.46	5333.57	40.85
	Kuzey-Güney	6.52	186.80	63.70	68.03	9.26	6272.72	40.85
	Düşey	8.41	52.40	17.80	48.05	4.62	3724.17	40.85
3129	Doğu-Batı	11.99	75.90	76.50	94.76	17.97	10312.03	29.28
	Kuzey-Güney	13.52	171.30	51.30	111.12	24.71	13095.61	29.28
	Düşey	7.17	42.60	22.40	57.18	6.54	4834.30	29.28
3132	Doğu-Batı	5.08	52.00	67.30	46.59	4.34	3554.91	22.57
	Kuzey-Güney	5.01	67.40	31.70	42.78	3.66	3128.62	22.57
	Düşey	3.56	34.40	12.50	30.25	1.83	1860.17	22.57
3143	Doğu-Batı	3.46	104.40	90.60	38.39	2.48	2437.62	25.72
	Kuzey-Güney	3.78	124.80	125.60	40.06	2.70	2597.51	25.72
	Düşey	3.81	27.70	19.30	31.12	1.63	1779.16	25.72
3145	Doğu-Batı	6.93	157.80	125.40	60.06	6.50	4936.21	40.64
	Kuzey-Güney	5.92	116.50	125.80	45.99	3.81	3307.39	40.64
	Düşey	6.10	65.20	32.00	41.16	3.05	2800.32	40.64
2712	Doğu-Batı	5.93	110.10	70.70	76.62	7.24	5887.46	33.90
	Kuzey-Güney	5.55	84.70	108.00	69.93	6.03	5133.45	33.90
	Düşey	3.14	26.70	14.60	40.44	2.02	2258.04	33.90
2713	Doğu-Batı	6.31	116.80	114.30	59.63	4.30	4000.33	26.05
	Kuzey-Güney	6.54	80.50	83.90	59.47	4.28	3984.74	26.05
	Düşey	5.93	62.80	44.30	42.57	2.19	2413.08	26.05

4. BİNA HASARLARINA YÖNELİK YAPILAN GÖZLEMLER

4.1. Betonarme Konut Tipi Binalar

Depreme dayanıklı binaların inşa edilmesine yönelik Türkiye’de yürütülen ilk çalışmalar 1939 Mw=7.8 olan Erzincan depremi sonrasında ortaya çıkmıştır. Son yüzyılda Türkiye Cumhuriyeti sınırları içerisinde meydana gelen en büyük depremler arasında yer alan 1939 Erzincan depremi yapıların belirli kurallar çerçevesinde tasarlanması gerekliliğini göstermiş ve hedeflenen amaçların sağlanması için asgari yasal sınırların belirtildiği yönetmelik Erzincan depreminden sonra 1940 yılında yayınlanmıştır. İlerleyen süreçlerde gerekli güncellemeler sonrasında Türk deprem yönetmeliği belirli aralıklar ile güncellenmiştir. Amerika’da bir milat olarak kabul edilen 1971 San Fernando depremi sonrasında gözlemlenen hasarlara yönelik betonarme yapılarda sünek davranış temelli tasarım ilkeleri için uyulması gerekli olan detaylandırma kuralları 1970’li yılların ortalarından başlayarak deprem yönetmelikleri ve ilgili standartlarda yerini almıştır [23]. Deprem yönetmeliklerinin içerikleri bilimsel araştırmalar ve gözlemler ışığında can ve mal kayıplarını azaltılırken, binlerce insanın hayatını kurtarmıştır. 1999 Kocaeli Depremi, 2011 Van Depremi, 2020 Elazığ ve İzmir Bayraklı depremlerinde yaşanan kayıplar ise karar verici mekanizmaya afet yönetimi ve zararların azaltılmasına yönelik alınması gerekli önlemler hakkında doneler

sunmuş ve daha büyük ölçekte yaşanabilecek kayıpların habercisi olmuştur. 6 Şubat 2023 depremleri sadece Türkiye’de değil dünyada etkilediği alan ve göstermiş olduğu karmaşık kaynak özelliklerinden dolayı son 35 yıl içerisinde yaşanan depremlerden farklı özellikler içermektedir.

Ana şok sonrası ortaya çıkan moment büyüklükleri yüksek değerlere sahip artçı depremler, hasar görmüş olan yapıları göçme olasılığı açısından riskli hale getirirken, toptan göçme performans seviyesine veya göçmenin önlenmesi performans seviyesine yaklaştırmıştır. Merkez üssü Kahramanmaraş Elbistan olan Mw=7.6 olan ikinci deprem can ve mal kaybının artışında etkin rol oynamıştır. Çalışmalar kapsamında ilk olarak sırasıyla hasar ve kayıpların yoğun olduğu Gaziantep’e bağlı olan Nurdağ, İslahiye ve Hatay’ın Kırıkhan ve Hassa ilçeleri saha incelemeleri yapmak için ziyaret edilmiştir. Takip edilen günlerde ise İskenderun, Antakya merkez, Gaziantep merkez, Kahramanmaraş’ın Pazarcık ve Kahramanmaraş merkezde incelemelerde bulunulmuştur. Gaziantep’in ilçelerinde yürütülen ilk gün çalışmalarında toptan göçmeye maruz kalan binalarda arama-kurtarma çalışmalarının öncelikli olarak Nurdağı ve İslahiye’de yürütüldüğü gözlemlenmiştir. Gaziantep’e bağlı Nurdağı ilçesinde yapısal sistemlerin benzer hasarlara sahip olduğu gözlenmiş ve kırsal kesimde yer alan az katlı binaların çoğunun mühendislik hizmeti almadığı, usta ve kalfalar tarafından inşa edildiği yerel halk tarafından bildirilmiştir. Bu çalışma kapsamında depremin ilk günlerinde ve sonrasında yazar tarafından çekilen fotoğraflar yardımıyla yapı hasarları irdelenecektir. Depremin ilk günlerinde yapılan saha gözlemleri Gaziantep’in Nurdağ ilçe merkezinde yer alan tekil ve mühendislik servisi almamış olan az katlı binalarda gerçekleştirilmiştir. Aynı bölgede çok katlı yapılarda yapısal ve yapısal olmayan hasarlar belirgin olarak gözlenmiştir. Kırsal kesimde yer alan deprem yönetmeliğinde aranan asgari donatı detayı koşullarını ve eleman boyutlarını yerine getirmeyen binalar toptan göçmeye maruz kalmıştır. Bina stoğunun yaşanmış olması, günümüz modern yönetmeliklerinde yer alan şartları sağlamayan kuvvetli kiriş zayıf kolon yaklaşımları ve kapasite korunumu ilkelerini dikkate almayan sistemler toptan göçmenin ortaya çıkmasına neden olmuştur.



Şekil 18 - Kırsal kesimde az katlı yapılarda gözlemlenen toptan göçme ve ilçe merkezinde sıklıkla rastlanan ağır hasarlı binalar

Betonarme yapılarda yer alan dış cephe kaplamaları ve dolgu duvarlar düzlem dışı davranışı nedeniyle deprem sırasında yaralanma, can ve mal kaybına sebep olmuştur. Dolgu duvar hasarları, çatılara montajlanmış su ısıtma sistemlerinin devrilmesinden dolayı cadde kenarlarına park edilmiş araçlar kullanılamaz hale gelerek ekonomik kayıpları arttırmıştır.

Kahramanmaraş Dulkadiroğlu ilçesinde dolgu duvar hasarları dar sokaklarda arama kurtarma faaliyetlerini sekteye uğratmıştır. Depremin ilk günlerinde fotoğraflanan bu durum, elektrik verilemeyen geç saatlerde arama kurtarma faaliyetlerinde ciddi problemler yaratmıştır.



Şekil 19 - Dolgu duvarların düzlem dışı davranışına bağlı yapısal olmayan hasarlar



Şekil 20 - Kahramanmaraş Dulkadiroğlu bölgesinde 2. gün sonunda mevcut durum ve arama-kurtarma faaliyetleri

Doğru bir taşıyıcı sistem düzenlemesinin önemi ve yapısal davranışına hakim yetkin mühendisler tarafından tasarlanan veya güçlendirilen binalar deprem bölgesinde ayakta kalmayı başardığı ve deprem yönetmeliğinde hedeflenen kontrollü hasar performans seviyesini sağlamıştır. Ağır hasarlı veya yıkılan binalar incelendiğinde ise mimari ve ticari kaygılarla doğru bir yapı düzenlemesinden uzak yapısal sistemler görülmüştür. Düşey taşıyıcı elemanlardan kolon ve perde duvarların kat planlarında geliş güzel yerleştirildiği, düzgün bir aks sistemine sahip olmayan sistemler ve kolonların uzun kenarlarının sadece belirli bir yöne doğrultulandırıldığı anlaşılmıştır. Bu durum planda düzensizlik sınıflandırması arasında yer alan burulma düzensizliğini yaratmış ve yapıların ileri seviyede hasar görmesine neden olmuştur. Uzun süre tekrarlı yüklere maruz kalan ve planda düzensizliklere sahip binalarda burulmanın yaratmış olduğu hasarın artışı veya büyüme etkileri çoklu deprem etkisi altında hasar durumunu arttırdığı düşünülmektedir. Bu durum Gemicic[27] tarafından da yapılan bir çalışmada düzgün bir grid sisteme sahip olmayan yapılara dair irdelemelerde de dile getirilmiştir.

Saha gözlemlerinde bu durumun en bariz halini yumuşak kat ve zayıf kat etkilerine bağlı ortaya çıkan yapısal hasarlar olarak belirlenmiştir. Deprem sırasında yassı kadayıf tarzı toptan göçme gösteren binalar detaylı olarak incelendiğinde deneyimli bir mühendislik bakış açısından ziyade taşıyıcı sistemin mimarların tercihleri doğrultusunda şekillendirilmesinin irdelenmesi gerekmektedir. Bu açıdan değerlendirildiğinde inşaat mühendislerinin inşaat sektöründe rekabetçi ticari ortamın bir sonucu olarak iş tanımlarının ve mesleki yetkinliklerini projelere yansıtamamalarının altında yatan nedenler karar verici mekanizma tarafından yeniden değerlendirilmelidir.



Şekil 21 - Kahramanmaraş Dulkadiroğlu ilçesinde yumuşak kat hasarı ve toptan göçme sonrası vatandaşlar tarafından yürütülen arama kurtarma faaliyetleri

Kırıkhan ve Hassa'da yürütülen saha ziyaretlerinde bölgede gözlemlenen bina hasarlarının afet bölgesinde hakim olan hasar dağılımına benzer bir eğilim gösterdiği belirlenmiştir. Betonarme binalarda yumuşak kat hasarı dışında farklı tipte taşıyıcı elemanlarda ve dolgu duvarlarda ağır hasarlar gözlemlenmiştir. Sahada yürütülen çalışmalarda toptan göçme sonucu önemli kayıplar yaşanmıştır (Şekil 25a).



Şekil 22 - Hassa bölgesinde (a) toptan göçmeye maruz kalmış bina (b) yumuşak kat hasarı



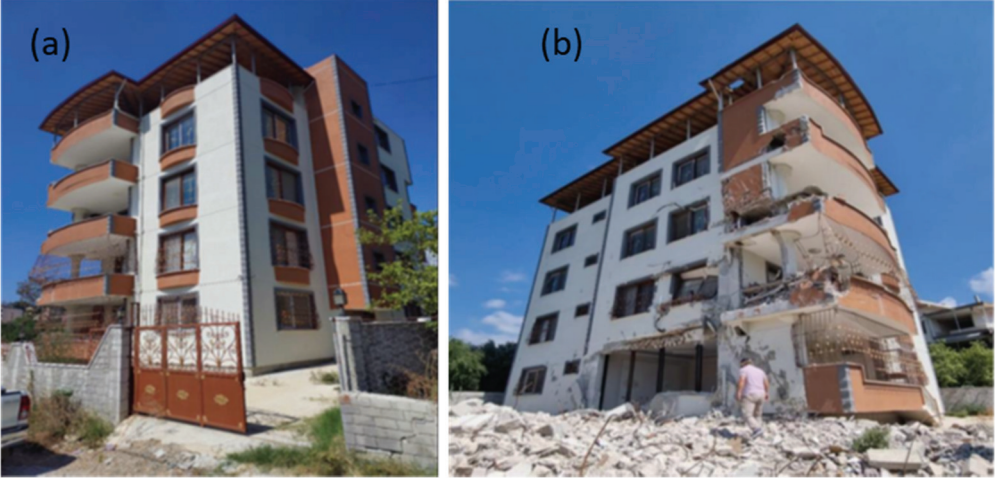
Şekil 23 - Hatay'ın Kırıkhan ilçesinde yumuşak kat hasarı ve binalarda toptan göçme

Kırıkmanda yürütülen saha ziyaretlerde afet bölgesinin genelinde gözlemlenen hasar dağılımına benzer bir dağılımın ortaya çıktığı belirlenmiştir. Betonarme binalarda yumuşak kat hasarı dışında farklı tipte taşıyıcı elemanlarda ve dolgu duvarlarda ağır hasarlar gözlemlenmiştir (Şekil 24).



Şekil 24 - Hatay Kırıkmanda yumuşak kat hasarı ve toptan göçmeye maruz kalan binalar

Hatay'ın Samandağ ilçesinde yazarında içerisinde bulunduğu saha inceleme ekibi tarafından yürütülen detaylı incelemelerde hafif hasarlı olarak sınıflandırılmış yapının yanında yıkılan yapının yaratmış olduğu giriş hasarı Şekil 25'te gösterilmiştir.



Şekil 25 - Samandağ ilçesinde hafif hasarlı binanın (a) ön cephesi ve (b) yan parselde yer alan binanın çarpması sonucu arka cephesinde yapısal elemanlarda oluşan hasarlar



Şekil 26 - (a) Asmolen döşeme hasarı (b) Yapısal düzenleme sonucu oluşan kolon hasarı

Döşemeler düzlem içi davranış açısından yeterli dayanıma sahip olurken deprem yüklerinin düşey taşıyıcı elemanlara taşınması ve dağıtılmasında önemli rol üstlenen yapısal elemanlardır. Deprem bölgesinde yaygınca kullanım alanı bulan döşeme tipleri arasında yaygın kullanılan asmolen döşemeler yer almaktadır. Asmolen döşemeler zayıf bağlantılara sahip olması yanında kat seviyelerinde yapım tekniğinden dolayı ince 5-7 cm aralığında döşeme kalınlığına sahip ve düzgün yük transferi için gerekli olan yeterli düzlem içi dayanım koşulunu sağlamakta problem yaratan sistemlerdir. Saha gözlemlerinde asmolen döşeme kaynaklı hasarlar yaygınca gözlemlenmiştir. Bölgede yer alan çekirdek perdelerin

kullanıldığı binalarda asmolen döşeme tabir edilen dişli döşemelerin kullanımından dolayı perdelerin çevrelerinde ciddi hasarlar gözlemlenmiştir. Deprem yönetmeliğinde her ne kadar tek doğrultuda çalışan asmolen döşemelerin kullanımı belirli koşullara bağlı olarak sınırlandırılmış olsada iki doğrultulu döşemelerde halen pratikte inşaat sektöründe yaygın kullanım alanı bulduğu deprem bölgesinde de gözlemlenmiştir. Asmolen döşemelerde ayrıca dar kolonlara geniş kirişlerin oturtulmasına çalışılmasının yaratmış olduğu olumsuz durumlar gözlemlenmiştir. (Şekil 26). Gaziantep Nurdağ ve İslahiye bölgelerinde döşeme hasarının gözlemlendiği binalarda ayrıca asma katın yaratmış olduğu olumsuzluklar göze çarpmaktadır.

Doğru bir şekilde düzenlenmemiş taşıyıcı sisteme sahip binalarda perdeler ve kolonlar taşıyıcı çerçevelerde geliş güzel olarak yerleştirilmekte ve düzgün bir aks yerleşimine sahip olmayan yapısal sistemler ortaya çıkmaktadır. Ayrıca kolonların uzun kenarlarının genellikle belirli bir doğrultuya baktığı binalarda benzer hasar eğilimleri gözlemlenmiştir (Şekil 26b).

4.2. Hastane Hasarları

4.2.1. Betonarme Hastane Binaları

Depremden sonra enkaz altından çıkarılan ve depremde yaralanmalar geçiren insanların kurtarılmasında sağlık hizmetlerinin eksiksiz verilmesi ve hastanelerin işlevselliğini koruması sayesinde sağlanabilir. Bu yüzden depreme dayanıklı hastane binalarının tasarımı için bina önem katsayısı konut tipi yapıların bir buçuk katı olarak deprem yönetmeliğinde yer almaktadır.

Yürütülen saha incelemelerinde bölgede bulunan geleneksel yöntemlere göre inşa edilmiş olan Kahramanmaraş, Antakya ve İskenderun illerinde bulunan özel hastanelerin birçoğu ileri seviyede hasar veya göçme bölgesi performans seviyesine ulaşmış olduğu belirlenmiştir. Kahramanmaraş bölgesinde yer alan özel hastanelerden Megapark ve Vatan hastaneleri depremin en kritik saatlerinde almış oldukları yapısal ve yapısal olmayan hasarlardan dolayı kullanılamaz hale gelmiştir (Şekil 27). Okuyucu daha detaylı resimler ve hasar değerlendirmesi için yazarın Hastaneler hakkında yayınlamış olduğu yayınlara başvurabilir. Ağır hasar alan illerden biri olan Kahramanmaraş'ta birçok özel hastane ağır hasar alıp hizmet veremezken tarihsel süreçte şehrin eski yerleşim yerlerinden olan Oniki Şubat ilçesi Mimaroba'da inşa edilmiş olan Kahramanmaraş Necip Fazıl Şehir Hastanesi Kadın Doğum ve Çocuk Ek Hizmet Binası ve Kadın Doğum ve Çocuk Hastalıkları Hastanesi ilk müdahalelerin yapıldığı hastaneler olmuştur

Erzin bölgesinde konut tipi yapılarda afet bölgesi ilan edilen diğer illere göre hasar sınırlı seviyelerde kalmasına rağmen Erzin Devlet Hastanesinde ortaya çıkan yapısal olmayan eleman hasarları hastanenin deprem sonrasında işlevselliğini kaybetmesine neden olmuştur. Geleneksel hastane binaları arasında olan Erzin ve Mustafa Kemal Üniversitesi Araştırma Hastanesinde gözlemlenen yapısal hasar yanında yapısal olmayan hasarlar geleneksel yöntemlere göre tasarlanmış bu iki hastanede işlevselliğin kaybına neden olmuştur. Bu iki hastanede hastalar depremin ilk gününde kurulan sahra hastanesine taşınmışlardır. İşlevsellik kaybına uğramış olan Mustafa Kemal Üniversitesi Araştırma Hastanesi ve Erzin Devlet Hastanesi herhangi bir yıkımın ortaya çıkmamasından dolayı deprem yalıtımlı Hatay Dörtyol Hastanesi ile birlikte acil müdahale anlamında önemli bir yükü üstlenmiştir. Hastanelerde

gözlemlenen yapısal hasarlardan çok yapısal olmayan hasarlar ve çalışanların deprem sonrası içerisinde buldukları psikoloji nedeniyle depremin ilk haftasında hastane personeli sahra hastanelerinde hizmet vermeye devam etmiştir. Erzin Hastanesinde kurulan sahra hastanesi şu anda konteyner hastane olarak bir dönüşüm yaşamıştır (Şekil 28).



Şekil 27 - 6 Şubat Pazarcık depreminden sonra kullanılamaz hale gelen (a) Megapark ve (b) Vatan Hastaneleri



Şekil 28 - Erzin Devlet Hastanesi (Sol) ve Mustafa Kemal Üniversitesi Eğitim Araştırma Hastanesi

4.2.2. Deprem Yalıtımlı Hastane Binaları

Deprem yalıtım sistemleri 1970 yılından bu yana teknolojinin geliştiricilerinden olan ülkeler arasında yer alan Japonya, Amerika, İtalya ve Yeni Zelanda'da yaygın kullanım alanı bulmuştur [28]. Ülkemizde ise son yıllarda kullanımı Sağlık Bakanlığının almış olduğu karar doğrultusunda 100 yatak veya üzeri inşa edilecek hastane binalarında deprem yalıtımının uygulanması şartı ile artış göstermiştir [29]. Deprem yalıtım sistemleri tek bir tip cihazın farklı boyut ve özelliklerde veya birkaç tip farklı yalıtım cihazının birlikte kullanılması ile uygulamada kullanılabilir. Deprem bölgesinde yer alan hastanelerde biri yerli olmak üzere üç farklı üretici tarafından 11 hastane binasında deprem yalıtım teknolojisinin uygulandığı belirlenmiştir. Deprem yalıtımlı hastanelere ziyaretler gerçekleştirilmiştir (Şekil 29). Ziyaret edilen deprem yalıtımlı hastane binarı arasında bazıları inşa aşamasında olan yapılar yer almıştır (Şekil 30). Bölgede meydana gelen depremleri deneyimlemiş bu hastanelerin deprem performansları da incelenmiştir. Tüm hastanelerde sarkaç tipi sürtünmeli deprem yalıtım cihazları kullanılmıştır. Toplamda 10 hastanede sürtünme yüzeyi sayısı iki olan cihazlar kullanılırken sadece Adana Şehir Hastanesinde dört yüzeyli sürtünme tipi sarkaç cihaz kullanılmıştır. Adana Şehir hastanesi bölgede yer alan en çok yatak kapasitesine sahip sağlık tesisidir. Adana'nın diğer afet bölgesinde yer alan Hatay, Kahramanmaraş ve Gaziantep'e nispeten daha az etkilenmesinden dolayı ağır hasarın odaklandığı şehirlerden Adana ve Kayseri'ye hasta transferleri gerçekleştirilmiştir.

Malatya Battalgazi, Hatay Dörtüyl ve Elbistan Devlet Hastanesinde kullanılan çift yüzeyli sürtünme tipi sarkaç deprem yalıtım cihazları başarılı uygulamaları ile hasarın kozmetik seviyelerde kalmasına neden olmuştur (Şekil 31). Fakat Doğanşehir ve Malatya Kadın Doğum Hastanelerinde yeterli sismik boşluğun sağlanmamasından dolayı binalarda yapısal olmayan hasarlar ortaya çıkmıştır.



Şekil 29 - Afet Bölgesi ilan edilen illerde ziyaret edilen deprem yalıtımlı hastanelerin yerleri ve ana şok olarak tanımlanan Şubat 2023 depremlerine göre haritalandırılması



Şekil 30 - Kahramanmaraş ilinde inşası devam eden deprem yalıtımlı hastane binasının inşaa süreci(Fotoğraflar TIS firması izniyle firmanın proje kataloglarından ve uydu görüntülerinden alınmıştır)



Şekil 31 - Malatya Battal Gazi(Sol), Hatay Dörtüyl (TIS firmasının izni ile resimler proje) ve Elbistan Devlet Hastanesi (Drone resimleri Kahramanmaraş Valiliğinin izni ile websitesinden alınarak kullanılmıştır)

4.3. Tescilli Kültür Varlığı Statüsünde Yapılarda Ortaya Çıkan Hasarlar

Gaziantep kalesi depremin ilk gününde konumundan dolayı hasar durumu kolaylıkla gözlemsel olarak tespit edilen kültür varlıklarından bir tanesi olmuştur. Yerel halk ile yürütülen görüşmelerde hasarın ağırlıklı olarak restorasyon ve yenileme çalışmaları yapılan bölgelerde ortaya çıktığı belirlenmiştir (Şekil 32).



Şekil 32 - Gaziantep Kalesi depremlerden sonra yaşanan hasarlar

Hatay ili sınırları içerisinde geçmişten günümüze tarihe ışık tutan bir çok tescilli ve Kültür Bakanlığı tarafından tescil edilmeyi bekleyen birçok yapı depremde ağır hasar görmüştür. Kültür varlıkları ile ilgili Hatay'da hasarın yoğunlaştığı bölgelerden bir tanesi Kurtuluş

Caddesidir. Kurtuluş Caddesinde ana yol dışında arka sokaklara erişim yığma binaların toptan göçmesinden dolayı sağlanamamıştır (Şekil 33).



Şekil 33 - Antakya Kurtuluş Caddesinde tescilli kültür varlıklarında yığma yapı hasarları

4.4. İbadethanelerde Gözlemlenen Hasarlar

Birçok depremde gözlemlendiği gibi narin yapısal sistemler olan cami minareleri ve taşıyıcı ve taşıyıcı olmayan yığma duvarlar hasarları depremlerin ve artçıların büyüklüklerinin etkisi ile Hatay Hassa, Kahramanmaraş ve Gaziantep illeri sınırlarında ibadethanelerde gözlemlenmiştir (Şekil 34).



Şekil 34 - İbadethanelerde gözlemlenen taşıyıcı ve taşıyıcı olmayan yığma duvar hasarları

4.5. Ulaştırma Ağlarında Ortaya Çıkan Hasarlar

Deprem bölgelerinde acil müdahalenin yapılabilmesi için şehirler arasında bağlantı yolları ve köprüler afet bölgesi için şehirlerin can damarlarını oluşturmaktadır. Depremi ilk günlerinde üst geçit olarak kullanılacak köprü tabliyesinin yolu kapatması ve karayollarında deprem sonrasında oluşan hasarlardan dolayı ulaşımda aksamalar meydana gelmiştir (Şekil 35).



Şekil 35 - Karayollarında depremin ilk günlerinde ortaya çıkan deprem hasarı

4.6. Deprem Sonrası Yapılan Geoteknik Değerlendirmeler

Sıvılaşma Adıyaman Gölbaşı ve Hatay'ın İskender'un ilçesinde özellikle Atatürk Bulvarı ve Çay mahallelerinde kum kaynamaları şeklinde gözlemlenmiştir. Limanda ayrıca gözlemlenen su taşkını, boru hatlarında yaşanan önemli hasarlarda alt yapı hizmetleri ile ilgili kesintiler ve salgın hastalık riski yaratmıştır. Adıyaman Gölbaşında yerel zemin koşulları nedeni ile yaşanan yapı temellerinde rijit dönmeler nedeni ile ortaya çıkan bina hasarları göze çarpmaktadır. Bölgede yer alan Kayı Apartmanında gözlemlenen rijit dönme nedeni ile diğer bir binanın üzerine yatması ile 6 Şubat deprem çiftinin yaşandığı bölgede geoteknik açıdan önemli sembol bina hasarlarından olmuştur (Şekil 36). Bölgede yer alan binalarda dikkatli incelemeler ve ölçümler ışığında birçok binada zemin kaynaklı dönme ve oturmalara bağlı hasarların ortaya çıktığı gözlemlenmiştir. Yan yatan ve ağır hasarlı binaların yıkım işlemleri Adıyaman Gölbaşı bölgesinde bu çalışma yayın sürecindeyken devam etmektedir.

İskenderun Bölgesinde liman tarafında yaşanan su taşkını ve yerel zemin koşulları nedeni ile kanalizasyon sisteminde ortaya çıkan hasarla kanalizasyon atıklarının suya karışmasının olumsuz etkileri gözlemlenmiştir (Şekil 37).



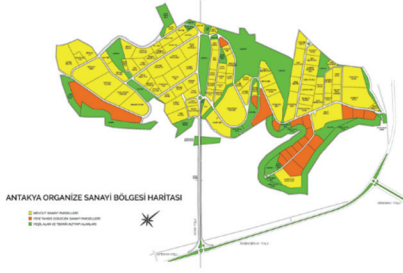
Şekil 36 - Adıyaman ilinde yerel zemin koşullarına bağlı ortaya çıkan hasar ve oturmalar(Anadolu Ajansı)



Şekil 37 - İskenderun'da konteyner bölgesindeki başlayan yangın ve İskenderun limanında oluşan su taşkını

4.7. Endüstriyel Yapı Tesislerinde Gözlemlenen Hasarlar

Deprem sonrasında bölgede yer alan endüstriyel tesisler belirli bir süre ile çalışanlarının veya çalışan yakınlarının kaybından dolayı Antakya ve Kahramanmaraş Organize Sanayi bölgelerinde üretime ara vermek zorunda kalmıştır. Çelik yapı sistemlerinde Antakya (Şekil 38). Yapısal hasar dışında yapısal olmayan ekipmanın hasar gördüğü ve fabrikanın ekipman kaynaklı üretime ara verildiği tespit edilmiştir. Kuru tahıl siloları ve sıvı yağ silolarına sahip firmalarda depolama tanklarında görülen farklı tipte hasarlar tespit edilmiştir (Şekil 39).



Şekil 38 - Antakya OSB içerisinde yapısal sistemi çelik olan hasarsız üretim tesisi ve depremde elemanları hasar almış olan precast endüstriyel tesis



Şekil 39 - Endüstriyel tesislerde silolar ve precast elemanlarda gözlemlenen deprem hasarları

5. SONUÇ

Türkiye depremselliğinin yüksek olduğu bir coğrafyada yer almasından dolayı 1939'dan bu yana yaşamış olduğu büyük depremlerde önemli kayıplar yaşayan bir ülkedir. Bir deprem ülkesi olmanın sorumluluğu ile doğru tasarım ve denetim mekanizmalarından geçmiş depreme dayanıklı yapıların bu coğrafyada inşa edilmesi bir zorunluluk olarak karşımıza çıkmaktadır. Merkez üssü Pazarcık ve Elbistan olan ve ardı sıra meydana gelen depremlerin ortaya çıkardığı deprem senaryosu, bugüne kadar üzerinde çalışılmış tehlike çalışmalarına göre beklenen depremin üzerinde bir büyüklükte ve karmaşık kaynak özelliklerinde meydana gelerek büyük can ve mal kayıpları ile sonuçlanmıştır.

- Yapısal tasarımda mimari ve ticari kaygılarla, mühendislik öngörüsünden uzak sadece program çıktılarından ve deprem yönetmeliği şartlarını tam anlamıyla anlamadan hareket eden, mühendislik muhakemesinden uzak yapısal tasarımlara odaklanmak, depreme dayanıklı yapı tasarımı ilkelerini gözardı edilmesine ve projelerin yetkin olmayan mühendisler tarafından yapılmasına neden olmuştur.
- Gelişmiş ülkelerde uygulanan yetkin mühendislik yasasının eksikliği ve denetim mekanizmasında yaşanan sorunlar bölgede inşa edilmiş olan binaların statik ve mimari projelerinde gün yüzüne çıkmıştır.
- 6 Şubat depremlerinde beklenenin üzerinde can kayıpları ve yapı hasarlarının ortaya çıkması gerçek bir laboratuvar olarak işlevselliğe sahip deprem bölgesinde önemli dersler çıkarılmasını sağlamıştır. Ortaya çıkan hasarlar kaynak özellikleri, enerjinin yayılımı, yapısal sistem sorunları, yerel zemin koşulları gibi birçok etkinin bir araya gelmesi ile yapıların toptan göçmesine veya ileri hasar seviyelerine ulaşmasına neden olmuştur.
- 6 Şubat 2023 depremlerinde yaşanan acı kayıplar ayrıca şehir planlanması, yapısal sistem tasarımında mimarlar ve mühendislerin iletişimi, projelerin inşa sürecinde bu iki meslek grubunun etkilerini, sahada denetim süreci ve onay aşamasının da içinde bulunduğu tüm paydaşların rollerinin karar verici mekanizma tarafından yeniden değerlendirilmesi gerektiğini göstermiştir.
- Bu çalışma kapsamında yapısal sistem hasarları incelendiğinde yönsellik, atım, deprem kaydının içerdiği itkiler, depremin süresi, betonarme binalarda basit detaylandırma problemleri, düşük kaliteli malzeme kullanımı, denetim ve lisanslama problemleri olarak özetlenebilir.
- 6 Şubat depremleri kaynak özellikleri ile yüzlerce istasyondan alınan deprem kayıtları yardımıyla dünya literatürüne önemli katkılarda bulunurken, çoklu fay kırılması, çoklu deprem etkisi ve tek depreme göre yürütülen sünek tasarım ilkelerinin bölgesel bazda değerlendirilmesi gerçeğini ve spektral parametreler dışında hızın dinamik davranışa katkısının parametrik etkilerinin ilişkilendirilmesi açısından mühendislik camiasına önemli soruları gündeme taşımıştır.
- 6 Şubat deprem çifti ve sonrasında bölgede yaşanan sismik aktivitede deprem yalıtımlı hastaneler geleneksel binalara göre uygulama hatalarına rağmen üstün performans göstererek pasif kontrol sistemleri anlamında toplumun artan ilgisi ile daha güvenli ve depremlere dirençli bir yapıya erişilmesinde etkin rol oynayabileceğini kanıtlamıştır. Bölgede toplamda 11 deprem yalıtımlı hastane, saha incelemeleri sırasında ziyaret edilmiştir. Deprem yalıtımlı hastane binalarında yalıtım sisteminden bağımsız olarak sahada yapılan uygulama hatalarından dolayı yapısal olmayan elemanlarda hasarlar gözlemlenmiştir. Yapısal olmayan hasarlar deprem yalıtımlı hastanelerin deprem sırasında en çok ihtiyaç duyulan zamanda tam kapasite çalışmasının önünde bir engel yaratarak, işlevsellik kaybına neden olmuştur.
- Güçlü yer hareketi istasyonlarında kaydedilen Kahramanmaraş depremlerinden elde edilen yer hareketleri çift yönlü yırtılmanın yaratmış olduğu oldukça karmaşık bir yapıya sahiptir. Türkiye Deprem Tehlike Haritalarından elde edilen tasarım spektrumu ve 6 Şubat depremlerinde 200'ün üzerinde AFAD istasyonunda kayıt altına alınan ivme

kayıtlarıyla davranış spektrumları kıyaslandığında spektrumun sabit hız bölgelerinde pratikte kayıt seçiminde beklenen yatay ivmelerin 2/3 katının üzerine çıktığı gözlemlenmiştir. Yer hareketi kayıtlarının itki içeriği ve yüksek değerlere sahip düşey bileşenleri hasarın artmasında ve hasarlı binaların yıkılmasında etkin rol oynamıştır.

Teşekkür

Bu çalışmanın gerçekleştirilmesinde farklı zamanlarda saha gezilerinde fikir alışverişinde bulunulan Japon araştırmacılarından Doç. Dr. Masahiro Kurata, Doç. Dr. Takuya Nagae, Prof. Yoshiaki Hisada, kıdemli araştırmacı Dr. Hirohisa Fukui, Azusa Sekkei Şef Mühendisi Mr. Kobayashi, Güney Kore takım lideri Prof. Sang-Hoon Oh, Kore saha gözlem ekibinden Prof. Jun Hee Kim, Prof. Jaebong Kim, Prof. Jaehyoun Choi, ve kıdemli araştırmacı Dr. Jaedo Kang'a, Taiwan takımının liderliğini yürüten Prof. George Yao, Prof. Jong-Dar Yau, Dr. Chung Hsien Shih, Dr. Peng Kuang Tsung ve Dr. Lin Yu-Chun'a teşekkürü borç bilirim. Depremden sonra hızlı bir aksiyon alınmasında ve depremin kritik ilk günlerinde yardımlarını esirgemeyen Yıldız Teknik Üniversitesi Rektörlüğüne şükranlarımı sunarım. Çalışmanın içeriğinin oluşturulmasında afet bölgesinde yer alan deprem yalıtımlı hastaneler ile ilgili bilgi paylaşımında bulunan yerli üreticilerden TİS firmasının genel müdürü Yüksek Mühendis Uğurcan Özçamur ve Proje Şefi Dr. Mühendis Sadun Tanışer'e ve İtalyan Deprem Yalıtım tedarikçisi FIP firmasının Türkiye temsilcisi Yüksek Mühendis Mircan Kaya'ya, saha gezilerinde bana eşlik eden, ekiplerin koordinasyonunda desteklerini esirgemeyen Dr. Öğretim Görevlisi Serhat Ulubay, Araştırma Görevlisi Yüksek Mimar Gamze Özmertyurt, İnşaat Mühendisi Şeçkin Baş ve Yüksek Mühendis Yaren Birşen'e yardımlarından dolayı teşekkür ederim.

Kaynakça

- [1] Afet ve Acil Durum Yönetimi Başkanlığı (AFAD) (2023) 06 Şubat 2023 Pazarcık (Kahramanmaraş) Mw 7.7 ve Elbistan (Kahramanmaraş) Mw 7.6 Depremlerine İlişkin Ön Değerlendirme Raporu
- [2] Strateji, TC Cumhurbaşkanlığı, and Bütçe Başkanlığı. "Kahramanmaraş ve Hatay depremleri raporu." (2023).
- [3] Atlas HGM (2023) General Directorate of Mapping <https://atlas.harita.gov.tr/>. Accessed multiple times between 7 to 20 February 2023
- [4] Soysal, H., Sipahioğlu, S., Kolçak, D., Altınok Y., 1981. Türkiye ve Çevresinin Tarihsel Deprem Kataloğu. TUBİTAK, Proje no. TBAG 341, İstanbul, 86.
- [5] Duman, T.Y., Emre, Ö., 2013. The East Anatolian Fault: Geometry, Segmentation and Jog Characteristics Geological Society, London, Special Publications, 372, 495-529, 615 s.
- [6] KRDAE, 2023. Kahramanmaraş - Gaziantep Türkiye M7.7 Earthquake, 6 February 2023 (04:17 GMT+03:00) Strong Ground Motion and Building Damage Estimations Preliminary Report (v6), 42.

- [7] Arpat, E. ve Şaroğlu, F., (1972). Doğu Anadolu Fayı ile ilgili bazı gözlemler ve düşünceler. Maden Tetkik ve Arama Enstitüsü. Ankara ss:44-50
- [8] Emre, Ö., Duman, T. Y., Özalp, S., Şaroğlu, F., Olgun, Ş., Elmacı, H., Çan, T., 2016. Active Fault Database of Turkey. Bulletin of Earthquake Engineering, 1-47.
- [9] Herece, E., 2008. Doğu Anadolu Fayı (DAF) Atlası. General Directorate of Mineral Research and Exploration. Special Publications. Ankara, Serial Number, 13, 359.
- [10] Şaroğlu, F., Emre, Ö., Kuşçu, I., 1992. The East Anatolian fault zone of Turkey. Ann. Tecton.6, 99–125.
- [11] Şengör, A.M.C., Görür, N., Şaroğlu, F., 1985. Strike-slip faulting and related basin formation in zone of tectonic escape: Turkey as a case study. In: Biddle, K.T., Christie-Blick, N. (Eds.), Strike-Slip Deformation, Basin Deformation and Sedimentation. In: Spec. Publ., Soc. Econ. Paleontol. Mineral., vol.37, pp.227–264.
- [12] Barka A, Reilinger R (1997) Active tectonics of the Eastern Mediterranean region: deduced from GPS, neotectonic and seismicity data.
- [13] Ambraseys, N.N., 1989. Temporary seismic, quiescence: SE Turkey. Geophys. J.96, 311–331.
- [14] Ambraseys, N.N. and Melville, C.P., 1995. Historical evidence of faulting in eastern Anatolia and northern Syria, Ann. Geophys. 38(3–4), 337–343.
- [15] Ambraseys, N.N., 2004. The 12th century seismic paroxysm in the Middle East: a historical perspective. Annals of Geophysics, Vol. 47, N. 2, 1-26.
- [16] Arpat, E., Şaroğlu, F., 1975. Türkiye'deki bazı önemli genç tektonik olaylar. TJK Bül.18, 91–101.
- [17] Aksoy, E., İnceöz, M., Koçyiğit, A., (2007). Lake Hazar Basin: a Negative Flower Structure on the East Anatolian Fault System (EAFS), SE Turkey. Turkish Journal of Earth Sciences Vol.16, 2007, pp. 1- TÜBİTAK
- [18] Hussain, E., Kalaycıoğlu, S., Milliner, C.W.D. et al. Preconditioning the 2023 Kahramanmaraş (Türkiye) earthquake disaster. Nat Rev Earth Environ 4, 287–289 (2023). <https://doi.org/10.1038/s43017-023-00411-2>
- [19] AFAD Deprem Kataloğu (2013-Günümüz), T.C. İçişleri Bakanlığı, Afet ve Acil Durum Yönetimi Başkanlığı, Deprem ve Risk Azaltma Genel Müdürlüğü, Deprem Dairesi Başkanlığı, Çevrimiçi Deprem Kataloğu, <https://deprem.afad.gov.tr/event-catalog>.
- [20] Worden, C.B., E. M. Thompson, M. Hearne, and D.J. Wald (2020). ShakeMap Manual Online: technical manual, user's guide, and software guide, U. S. Geological Survey. <http://cbworden.github.io/shakemap/>.DOI: <https://doi.org/10.5066/F7D21VPQ>
- [20] Hancılar, U., C.Tüzün, C.Yenidoğan, M.Erdik, 2010. ELER Software-A new tool for urban loss assessment, Natural Hazards and Earth System Sciences, December 2010

- [21] Yenidogan, C.; Yokoyama, R.; Nagae, T.; Tahara, K.; Tosauchi, Y.; Kajiwara, K.; Ghannoum, W. Shake table test of a full-scale four-story reinforced concrete structure and numerical representation of overall response with modified IMK model. *Bull. Earthq. Eng.* 2018, 16.
- [22] İçişleri Bakanlığı, Afet ve Acil Durum Yönetimi Başkanlığı. Türkiye bina deprem yönetmeliği, TBDY-2018, Ankara, 2018.
- [23] Bertero, V. V., Mahin, S. A., & Herrera, R. A. (1978). Aseismic design implications of near-fault San Fernando earthquake records. *Earthquake engineering & structural dynamics*, 6(1), 31-42.
- [24] Park, Y. J., Ang, A. S., & Wen, Y. K. (1984). Seismic damage analysis and damage-limiting design of RC buildings. *Civil Engineering Studies SRS-516*.
- [25] Bertero, Vitelmo V. "Lessons learned from recent earthquakes and research and implications for earthquake-resistant design of building structures in the United States." *Earthquake spectra* 2, no. 4 (1986): 825-858.
- [26] Park, Young-Ji, AH-S. Ang, and Yi-Kwei Wen. "Seismic damage analysis and damage-limiting design of RC buildings." *Civil Engineering Studies SRS-516* (1984).
- [27] Gemici B (2019) Investigation of the effect of structural grid discontinuity on the earthquake behavior of midrise RC moment frames. Master of Science Thesis. Izmir Institute of Technology (IYTE), Izmir, Turkey
- [28] Yenidogan, C., & Erdik, M. (2016). A comparative evaluation of design provisions for seismically isolated buildings. *Soil Dynamics and Earthquake Engineering*, 90, 265-286.
- [29] Yenidogan, C., 2021. Earthquake-resilient design of seismically isolated buildings: A review of technology. *Vibration*, 4(3), 602-647.
- [30] Yenidogan, C. Karma Deprem Yalıtım Sistemlerinin Deneysel Performans Değerlendirmesi. *Dokuz Eylül Üniversitesi Mühendislik Fakültesi Fen ve Mühendislik Dergisi*, 23(69), 767-779

A Receding Contact Problem of Two Layers one of Functionally Graded, Loaded by Circular Rigid Block and Resting on a Pasternak Foundation

Aleyna YAZICIOĞLU^{1*}
Ahmet BİRİNCİ²
Gökhan ADIYAMAN³



ABSTRACT

In this study, frictionless receding contact problem of two elastic layers which one is functionally graded material (FGM) resting on a Pasternak foundation is considered. The external load is applied to the homogeneous elastic layer by means of a circular rigid block and the functionally graded layer rests on a Pasternak foundation. The effect of gravity forces is neglected, and only compressive normal tractions can be transmitted through the interfaces. Displacement and stress expressions for the layers are obtained using the theory of elasticity and integral transformation technique. By applying the boundary conditions for the problem, reduced to two integral equations in which the contact stresses and contact lengths are unknown. The system of integral equations is numerically solved by making use of appropriate Gauss Chebyshev integration formulas. The equilibrium conditions are satisfied in the solution and the contact stresses and contact distances related to the problem are obtained for various dimensionless quantities.

Keywords: Contact problem, functionally graded material, Pasternak foundation.

1. INTRODUCTION

In everyday life, objects are commonly in contact with one other, resulting in displacements and deformations within these objects. To calculate these displacements and deformations, the field of mechanics has transformed such objects into ideal problems that can be solved.

Note:

- This paper was received on November 19, 2023 and accepted for publication by the Editorial Board on May 22, 2024.
- Discussions on this paper will be accepted by November 30, 2024.

• <https://doi.org/10.18400/tjce.1392997>

1 Akdeniz University, Civil Engineering Department, Antalya, Türkiye
aleynayazicioglu@akdeniz.edu.tr - <https://orcid.org/0009-0000-1794-5164>

2 Karadeniz Technical University, Civil Engineering Department, Trabzon, Türkiye
birinci@ktu.edu.tr - <https://orcid.org/0000-0002-5913-7699>

3 Karadeniz Technical University, Civil Engineering Department, Trabzon, Türkiye
gadiyaman@ktu.edu.tr - <https://orcid.org/0000-0002-3076-4090>

* Corresponding author

In the literature, these issues are commonly referred to as contact problems. Throughout history, numerous contact problems requiring complex and lengthy procedures in various geometries have been studied by numerous researchers.

The contact of a layer resting on an elastic half-plane and loaded by a rigid circular block was examined by Dhaliwal [1]. The problem was reduced to a Fredholm integral equation and was solved using power series and numerical methods. The frictionless contact problem of an elastic sheet resting on an elastic half-plane with a spring load applied to the entire surface except for a specific length of the sheet was investigated by Keer and Chantaramungkorn [2]. The contact situation of the elastic layer pressed against a block with different profiles was addressed by Ratwani and Erdogan [4]. Both frictional and frictionless contact of a layer resting on an elastic half-plane and loaded from above by a rigid flat block were explored by Cakiroglu [5]. A contact problem for an elastic layer supported by two elastic quarter planes was analyzed by Aksogan [6]. The contact problem of a composite layer consisting of two elastic beams resting on an elastic base according to the theory of elasticity was solved by Birinci and Erdöl [7]. The contact problem involving two infinite elastic layers resting on the Winkler foundation and subjected to symmetrical distributed loads was studied by Birinci and Erdöl [8]. Frictionless double contact problem for two elastic layers which the lower one is entirely bonded to a rigid support was investigated by Comez [9]. A double receding contact problem involving a rigid stamp and two layers was explored by Comez *et al.* [10]. The plane problem of a frictionless receding contact between an elastic functionally graded (FG) layer and a homogeneous half-space when the two bodies were pressed together was investigated by El-Borgi *et al.* [11]. A frictionless receding contact problem between an anisotropic elastic layer and an anisotropic elastic half plane, with both bodies pressed together by means of a rigid circular stamp, was analyzed by Kahya *et al.* [12]. The frictionless contact problem of two elastic layers with different elastic properties and heights, resting on two homogeneous, isotropic, and symmetric elastic quarter planes according to the theory of elasticity, was examined by Yaylacı and Birinci [13]. A contact model between a homogeneous half-space with a linearly graded layer and a rigid punch was examined by Chen and Chen [14]. The plane problem of a smooth double receding contact between an FG layer and an elastic layer when pressed together was studied by Yan and Li [15]. The moving contact problem for a rigid cylindrical punch and a functionally graded layer was solved by Comez [16]. Continuous contact on a functionally graded layer was analyzed using the finite element method by Polat *et al.* [17]. The plane contact problem based on the theory of elasticity following indentation into an elastic transversely isotropic half-plane with a transversely isotropic FG coating using a non-deformable punch with a flat base was examined by Vasiliev *et al.* [18]. The discontinuous contact problem between a functionally graded (FG) layer, loaded symmetrically with a point load P through a rigid block, and a homogeneous half-space was addressed by Oner and Birinci [19]. The quasi-static frictional contact problem of a rigid rounded punch sliding over a bi-directionally graded half-plane within the framework of plane strain elasticity was examined by Arslan [20]. A method for determining the parameters of the exponentially varying shear modulus of an FG half-space was proposed by Zelentsov *et al.* [21]. The effect of punch speed on frictional contact mechanics of finite-thickness graded layer resting on the rigid foundation researched by Balcı [22]. A double receding contact problem of a functionally graded layer and a homogeneous elastic layer resting on a Winkler foundation was investigated by Birinci *et al.* [23]. Contact analysis of an elastic layer supported by a

wedge in plane was investigated by Bakioğlu *et al.* [24]. The problem was formulated with closed-form integral equations. An analysis of a contact problem using analytical, finite element method (FEM), and multilayer perceptron (MLP) approaches was conducted by Yaylacı *et al.* [25]. The main objective of this study was to assess the applicability of MLP analysis for the frictionless contact problem of an FG layer bonded to a rigid foundation. An analytical approach to solving the continuous and discontinuous contact problems of a functionally graded (FG) layer subjected to a distributed load was proposed by Adiyaman *et al.* [26]. The problem was analytically solved by applying boundary conditions for both continuous and discontinuous contact cases.

In this paper, the frictionless contact problem of two infinite layers resting on a Pasternak foundation and loaded by a circular rigid block is considered according to theory of Elasticity. The layers have different material properties and heights, with the upper layer being homogeneous and the lower layer functionally graded. The problem is assumed that contact along the interface is frictionless, and the effect of gravity force is neglected. By applying the boundary conditions for the problem, reduced to two integral equations in which the contact stresses and contact lengths are unknown. Solving the integral equations numerically by using appropriate Gauss Chebyshev integration formulation, and the contact stresses and contact lengths are investigated for various dimensionless values in the problem.

1.1. Formulation of the Problem

Consider the receding contact problem between a homogeneous elastic layer and an FG layer resting on a Pasternak foundation and loaded by a circular rigid block, as shown in Fig.1.

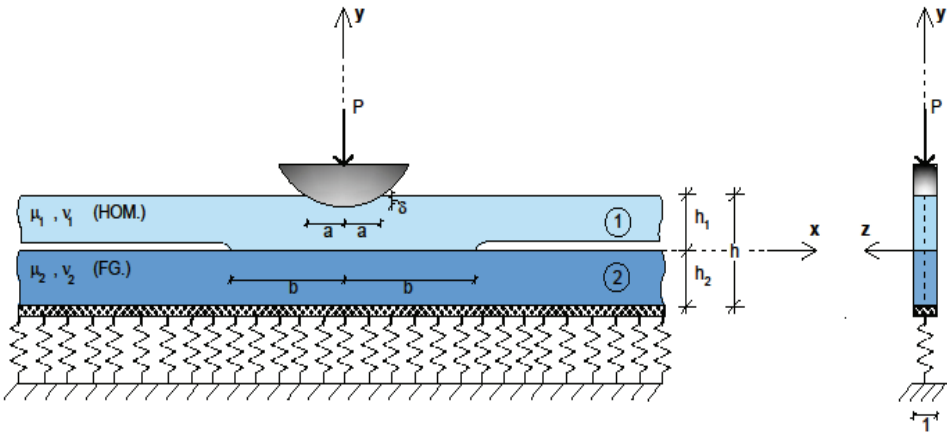


Fig. 1 - Geometry and loading of contact problem.

Observing that a circular rigid block with radius R transmits a concentrated normal force to a homogeneous layer of thickness h_1 , and an FG layer of thickness h_2 rests on a Pasternak foundation having an elastic spring constant k_0 and G Pasternak foundation moduli.

The circular rigid block and homogeneous layer are in contact with each other on the interval $(-a, a)$, and the homogeneous layer and FG are in contact with each other on the interval $(-b, b)$. The thickness in the z -direction is unity. For the graded layer, the material was modeled as an inhomogeneous isotropic material with a gradient oriented along the y direction. The Poisson's ratio, ν_2 , was assumed constant, and the shear modulus, μ_2 , depended on the y -coordinate only and is expressed as the following exponential function:

$$\mu_2 = \mu_0 \cdot e^{\beta y}, (-h_2 \leq y \leq 0), \quad (1)$$

where μ_0 is the shear modulus on the top surface of the FG layer (for $y = 0$), and β is the stiffness parameter controlling the shear modulus variations in the graded medium. For the homogeneous layer, the shear modulus and Poisson's ratio are, μ_1 and ν_1 , respectively.

It is assumed that the contact surfaces are frictionless and only compressive normal tractions can be transmitted through the contact interfaces. Observing that $x = 0$ is a plane symmetry, it is sufficient to consider the problem in the regions $(0 \leq x < \infty)$. The displacement $u(x, y)$, $v(x, y)$ and stress components $\sigma_x(x, y)$, $\sigma_y(x, y)$ and $\tau_{xy}(x, y)$ for the layers have been obtained using the basic equations of Elasticity and the Fourier transform techniques as follows [27]:

For the homogeneous layer;

$$u_1(x, y) = \frac{2}{\pi} \int_0^\infty [(A_1 + A_2 y)^{-\xi y} + (A_3 + A_4 y)^{\xi y} \sin(\xi x)] d\xi \quad (2a)$$

$$v_1(x, y) = \frac{2}{\pi} \int_0^\infty \left\{ [A_1 + \left(\frac{\kappa_1}{\xi} + y\right)A_2] e^{-\xi y} + [-A_3 + \left(\frac{\kappa_1}{\xi} - y\right)A_4] e^{\xi y} \right\} \cos(\xi x) d\xi \quad (2b)$$

$$\frac{1}{2\mu_1} \sigma_{x_1}(x, y) = \frac{2}{\pi} \int_0^\infty \left\{ \left[\xi(A_1 + A_2 y) - \left(\frac{3-\kappa_1}{2}\right)A_2 \right] e^{-\xi y} + \left[\xi(A_3 + A_4 y) + \left(\frac{3-\kappa_1}{2}\right)A_4 \right] e^{\xi y} \right\} \cos(\xi x) d\xi \quad (2c)$$

$$\frac{1}{2\mu_1} \sigma_{y_1}(x, y) = \frac{2}{\pi} \int_0^\infty \left\{ \left[-\xi(A_1 + A_2 y) - \left(\frac{\kappa_1+1}{2}\right)A_2 \right] e^{-\xi y} + \left[-\xi(A_3 + A_4 y) + \left(\frac{\kappa_1+1}{2}\right)A_4 \right] e^{\xi y} \right\} \cos(\xi x) d\xi \quad (2d)$$

$$\frac{1}{2\mu_1} \tau_{xy_1}(x, y) = \frac{2}{\pi} \int_0^\infty \left\{ \left[-\xi(A_1 + A_2 y) - \left(\frac{\kappa_1-1}{2}\right)A_2 \right] e^{-\xi y} + \left[\xi(A_3 + A_4 y) - \left(\frac{\kappa_1-1}{2}\right)A_4 \right] e^{\xi y} \right\} \sin(\xi x) d\xi \quad (2e)$$

For the FG layer;

$$u_2(x, y) = \frac{2}{\pi} \int_0^\infty \sum_{j=1}^4 B_j e^{s_j y} \sin(\xi x) d\xi \quad (3a)$$

$$v_2(x, y) = \frac{2}{\pi} \int_0^\infty \sum_{j=1}^4 B_j m_j e^{s_j y} \cos(\xi x) d\xi \quad (3b)$$

$$\sigma_{x_2}(x, y) = \frac{2\mu_0 e^{\beta y}}{\pi(\kappa_2 - 1)} \int_0^\infty \sum_{j=1}^4 B_j [(3 - \kappa_1)m_j n_j + \xi(\kappa_1 + 1)] e^{s_j y} \cos(\xi x) d\xi \quad (3c)$$

$$\sigma_{y_2}(x, y) = \frac{2\mu_0 e^{\beta y}}{\pi(\kappa_2 - 1)} \int_0^\infty \sum_{j=1}^4 B_j C_j e^{s_j y} \cos(\xi x) d\xi \quad (3d)$$

$$\tau_{xy_2}(x, y) = \frac{2\mu_0 e^{\beta y}}{\pi} \int_0^\infty \sum_{j=1}^4 B_j D_j e^{s_j y} \sin(\xi x) d\xi \quad (3e)$$

where $A_j, B_j (j = 1, \dots, 4)$ are the unknown functions which will be determined from boundary conditions prescribed on $y = h_1, y = 0$ and $y = -h_2$. $\kappa_i = \frac{3-\nu_i}{1+\nu_i}$ for plane stress and $\kappa_i = 3 - 4\nu_i$ for plane strain. C_j, D_j, m_j and $s_j (j = 1, \dots, 4)$ in the equations for the FG layer are as follows:

$$C_j = [(\kappa_2 + 1)m_j s_j + \xi(3 - \kappa_2)] \quad (4)$$

$$D_j = [s_j - \xi m_j] \quad (5)$$

$$m_j = \frac{(3\beta + 2s_j - \beta\kappa_2)[s_j(\beta + s_j)(\kappa_2 + 1) - \xi^2(\kappa_2 + 3)]}{\xi[4\xi^2 - \beta^2(\kappa_2 - 3)(\kappa_2 + 1)]} \quad (6)$$

$$s_1 = -\frac{1}{2} \left(\beta + \sqrt{4\xi^2 + \beta^2 - 4\xi\beta i \sqrt{\frac{3-\kappa_i}{\kappa_2+1}}} \right), s_2 = -\frac{1}{2} \left(\beta - \sqrt{4\xi^2 + \beta^2 - 4\xi\beta i \sqrt{\frac{3-\kappa_i}{\kappa_2+1}}} \right) \quad (7a)$$

$$s_3 = -\frac{1}{2} \left(\beta + \sqrt{4\xi^2 + \beta^2 + 4\xi\beta i \sqrt{\frac{3-\kappa_i}{\kappa_2+1}}} \right), s_4 = -\frac{1}{2} \left(\beta - \sqrt{4\xi^2 + \beta^2 + 4\xi\beta i \sqrt{\frac{3-\kappa_i}{\kappa_2+1}}} \right) \quad (7b)$$

1.2. Boundary Conditions and Integral Equations

The contact problem must be solved under the following boundary conditions:

$$\sigma_{y_1}(x, h_1) = \begin{cases} -p_1(x) & ; & (0 \leq x \leq a) \\ 0 & ; & (a \leq x < \infty) \end{cases} \quad (8a)$$

$$\tau_{xy_1}(x, h_1) = 0, \quad (0 \leq x < \infty) \quad (8b)$$

$$\sigma_{y_2}(x, 0) = \begin{cases} -p_2(x) & ; & (0 \leq x \leq b) \\ 0 & ; & (b \leq x < \infty) \end{cases} \quad (8c)$$

$$\sigma_{y_1}(x, 0) = \sigma_{y_2}(x, 0), \quad (0 \leq x < \infty) \quad (8d)$$

$$\tau_{xy_1}(x, 0) = 0, \quad (0 \leq x < \infty) \quad (8e)$$

$$\tau_{xy_2}(x, 0) = 0, \quad (0 \leq x < \infty) \quad (8f)$$

$$\sigma_{y_2}(x, -h_2) = k_0 v_2(x, -h_2) - G \frac{\partial^2 v_2(x, -h_2)}{\partial x^2}, \quad (0 \leq x \leq \infty) \quad (8g)$$

$$\tau_{xy_2}(x, -h_2) = 0, \quad (0 \leq x \leq \infty) \quad (8h)$$

$$\frac{\partial}{\partial x} [v_1(x, h_1)] = \frac{\partial F(x)}{\partial x} \quad (0 \leq x \leq a) \quad (8i)$$

$$\frac{\partial}{\partial x} [v_1(x, 0) - v_2(x, 0)] = 0, \quad (0 \leq x \leq b) \quad (8j)$$

The equilibrium conditions of the problem are written as follows:

$$\int_{-a}^{+a} p_1(x) dx = P, \int_{-b}^{+b} p_2(x) dx = P \quad (9)$$

Here, a and b are the half contact lengths between the circular rigid block and homogeneous layer, and between the homogeneous layer and FG layer, respectively; $p_1(x)$ and $p_2(x)$ are the primary unknown contact pressures on the contact surfaces; k_0 and G are the Winkler and Pasternak foundation moduli, P represents the singular load applied through the circular rigid block. $F(x)$ is a known function denoting the profile of the circular rigid block and is expressed as follows:

$$F(x) = R + h_2 + \delta - (R^2 - x^2)^{0.5} \quad (10)$$

Derivative of this function with respect to x ,

$$\frac{\partial F(x)}{\partial x} = \frac{x}{(R^2 - x^2)^{0.5}} \cong \frac{x}{R} \quad R \gg x \quad (11)$$

In these expressions, δ is the maximum vertical displacement of the layer on the symmetry axis and R is the radius of the circular block. Using the boundary conditions in Eqs. (8a-8h), the unknown coefficients $A_j, B_j (j = 1, \dots, 4)$ appearing in equations (2a-3e) are determined in the terms of the primary unknown contact pressures, $p_1(x)$ and $p_2(x)$. Thus, the stresses and displacements can be expressed depending on the unknown contact pressures.

The unknown contact pressures, $p_1(x)$ and $p_2(x)$ are determined from the mixed conditions in Eqs. (8i-8j), which have not yet been satisfied. After some routine manipulations and using the symmetry property, these mixed conditions gave the following system of integral equations depending on $p_1(x)$ and $p_2(x)$.

$$\frac{2}{\pi} \int_{-a}^a p_1(t_1) \left\{ F_1(x_1, t_1) - \frac{\kappa_1 + 1}{8} \left[\frac{1}{t_1 - x_1} \right] \right\} dt_1 + \frac{2}{\pi} \int_{-b}^b p_2(t_2) F_2(x_1, t_2) dt_2 = \frac{x}{R} \quad (11a)$$

$$\frac{2}{\pi} \int_{-a}^a p_1(t_1) T_1(x_2, t_1) dt_1 + \frac{2}{\pi} \int_{-b}^b p_2(t_2) \left\{ T_2(x_2, t_2) - T_3(x_2, t_2) + \left[\left(\frac{\kappa_1 + 1}{8\mu_1} + \frac{\kappa_2 + 1}{8\mu_0} \right) \left(\frac{1}{t_2 - x_2} \right) \right] \right\} dt_2 = 0 \quad (11b)$$

Integral kernels as given F_1, F_2, T_1, T_2 and T_3 have not been included in the paper due to the extensive and intricate nature of their expressions.

1.3. Numerical Solution of the System of Integral Equations

Dimensionless quantities can be introduced to simplify the numerical solution to integral equations,

$$s_1 = x_1/a \quad s_2 = b/x_2 \tag{12a}$$

$$r_1 = t_1/a, \quad r_2 = t_2/b \tag{12b}$$

$$G_1(r_1) = \frac{h_1}{p} p_1(t_1), \quad G_2(r_2) = \frac{h_1}{p} p_2(t_2) \tag{12c}$$

$$k_w = \frac{k_0}{\mu_0}, \quad k_p = \frac{G}{\mu_0} \tag{12d}$$

where k_w and k_p non-dimensional foundation moduli.

The normalized form of the integral Equations (11a-11b) and equilibrium conditions (9) may be written as follows:

$$\int_{-1}^1 G_1(r_1) \left\{ \frac{a}{h_1} \overline{F}_1(s_1, r_1) - \frac{\kappa_1+1}{8\mu_1} \left[\frac{1}{r_1-s_1} \right] \right\} dr_1 \dots$$

$$\dots + \frac{b}{h_1} \int_{-1}^1 G_2(r_2) \overline{F}_2(s_1, r_2) dr_2 = \frac{\pi}{2} \mu_1 \frac{a/h_1}{p/h_1} \tag{13a}$$

$$\frac{a}{h_1} \int_{-1}^1 G_1(r_1) \overline{T}_1(s_2, r_1) dr_1 \dots$$

$$\dots + \int_{-1}^1 G_2(r_2) \left\{ \frac{b}{h_1} \left(\overline{T}_2(s_2, r_2) + \overline{T}_3(s_2, r_2) \right) + \left[\left(\frac{\kappa_1+1}{8\mu_1} + \frac{\kappa_2+1}{8\mu_0} \right) \left(\frac{1}{r_2-s_2} \right) \right] \right\} dr_2 = 0 \tag{13b}$$

$$\frac{a}{h_1} \int_{-1}^1 G_1(r_1) dr_1 = 1, \quad \frac{b}{h_1} \int_{-1}^1 G_2(r_2) dr_2 = 1 \tag{13c}$$

Because of the smooth contact at the end points a and b, the contact pressures $p_1(x)$ and $p_2(x)$ are zero at the edges. Thus, the integral equation (13) has an index of -1, and the following expressions can be obtained [3]:

$$G_1(r_{1i}) = w_1(r_{1i}) g_1(r_{1i}), \quad w_1(r_{1i}) = (1 - r_{1i})^{0.5} (1 + r_{1i})^{0.5}, \quad (i = 1, \dots, N) \tag{14a}$$

$$G_2(r_{2i}) = w_2(r_{2i}) g_2(r_{2i}), \quad w_2(r_{2i}) = (1 - r_{2i})^{0.5} (1 + r_{2i})^{0.5}, \quad (i = 1, \dots, N) \tag{14b}$$

where $g_1(r_1)$ and $g_2(r_2)$ are continuous and bounded functions in the interval $[-1, 1]$, respectively. Using Gauss-Chebyshev integration formulas [3], equation (13) can be converted to a system of algebraic equations as follows:

$$\begin{aligned} \sum_{i=1}^N W_{1i} g_{1i}(r_{1i}) \left\{ \frac{a}{h_1} \overline{F}_1(n_{1k}, r_{1i}) - \frac{\kappa_1+1}{8} \left[\frac{1}{r_{1i}-n_{1k}} \right] \right\} \dots \\ \dots + \frac{b}{h_1} \sum_{i=1}^N W_{2i} g_{2i}(r_{2i}) \overline{F}_1(n_{1k}, r_{2i}) = \frac{\pi}{2} \frac{\mu_1}{P/h_1} \frac{a/h_1}{R/h_1} n_{1k} \end{aligned} \quad (15a)$$

$$\begin{aligned} \frac{a}{h_1} \sum_{i=1}^N W_{1i} g_{1i}(r_{1i}) \overline{T}_1(s_{2k}, r_{1i}) \dots \\ + \sum_{i=1}^N W_{2i} g_{2i}(r_{2i}) \left[\frac{b}{h_1} \left(\overline{T}_2(s_{2k}, r_{2i}) - \overline{T}_3(s_{2k}, r_{2i}) \right) + \left(\left(\frac{\kappa_1+1}{8\mu_1} + \frac{\kappa_2+1}{8\mu_0} \right) \left(\frac{1}{r_{2i}-s_{2k}} \right) \right) \right] = 0 \end{aligned} \quad (k = 1, \dots, N+1) \quad (15b)$$

$$\frac{a}{h_1} \sum_{i=1}^N W_{1i} g_1(r_{1i}) = 1 \quad (i = 1, \dots, N) \quad (15c)$$

$$\frac{b}{h_1} \sum_{i=1}^N W_{2i} g_2(r_{2i}) = 1 \quad (i = 1, \dots, N) \quad (15d)$$

where r_i and s_k are the zeros of the related Chebyshev polynomials and W_i^N is the weighting constant, expressed as follows:

$$W_i^N = \pi \left(\frac{1-r_i^2}{N+1} \right) \quad (i = 1, \dots, N) \quad (16a)$$

$$r_i = \cos \left(\frac{i\pi}{N+1} \right) \quad (i = 1, \dots, N) \quad (16b)$$

$$s_k = \cos \left(\frac{\pi}{2} \frac{2k-1}{N+1} \right) \quad (k = 1, \dots, N+1) \quad (16c)$$

It can be demonstrated that the $\left(\frac{N}{2} + 1\right)$ -th equations in (15a) and (15b) are automatically satisfied. Thus equation (15) $2N+2$ algebraic equations to determine the $2N+2$ unknowns, namely $g_1(r_{1i})$, $g_2(r_{2i})$ ($i = 1, \dots, N$), a and b . The system of equations is linear in $g_1(r_{1i})$ and $g_2(r_{2i})$, but nonlinear in a and b . Therefore, an iteration scheme should be used to determine these two unknowns. This iteration scheme for the problem was created with a code by using MATLAB program. Twenty Gauss points and Chebyshev function ($N=20$) are used for the solution in the MATLAB code. Until the equilibrium conditions are satisfied, iteration continue to verify the obtained contact stresses. Once the equilibrium conditions are met with the desired precision, a solution is considered achieved. Figure 2 shows the flowchart of the iterative MATLAB code.

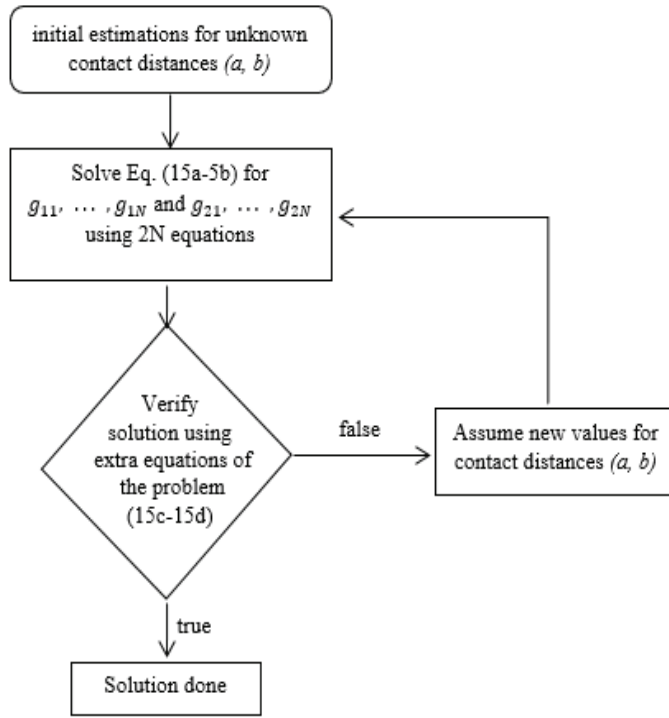


Fig. 2 - Flowchart of the iterative algorithm

1.4. Numerical Results

This section presents numerical results and discussion for the contact pressures and contact lengths at both interfaces of contact. Therefore, the effects of the different shear modulus ratios of the layers (μ_0/μ_1) different radius of circular rigid block (R/h_1), non-dimensional Pasternak foundation parameter (k_p) and different material properties (κ_i) the data obtained from numerical applications are presented with the help of graphs.

Table 1 presents the number of iterations involving the equilibrium condition conducted to achieve a solution for the receding contact problem. Iteration resultant the equilibrium conditions should be equal to 1. Columns (1)–(4) of Table 1 correspond, respectively, to the iteration number, value of the equilibrium condition $(\frac{a}{h_1} \int_{-1}^1 G_1(r_1) dr_1, \frac{b}{h_1} \int_{-1}^1 G_2(r_2) dr_2)$, the normalized receding contact length ($a/h_1, b/h_1$) and the relative error of the normalized receding contact length between two successive iterations ($E(\%)$).

Table 2-3 illustrates that for significantly high values of the spring constant in our study, the foundation was assumed to be rigid and compared with a prior study conducted by Comez [9]. As shown in the table, the results are consistent.

Table 1 - Solution iteration of the receding contact problem including the equilibrium condition for initial value $a/h_1 = b/h_1 = 1$.

Iteration no.	$\frac{a}{h_1} \int_{-1}^1 G_1(r_1) dr_1$	a/h_1	$E(\%)$	$\frac{b}{h_1} \int_{-1}^1 G_2(r_2) dr_2$	b/h_1	$E(\%)$
(1)	(2)	(3)	(4)	(2)	(3)	(4)
	1.0	1.0		1.0	1.0	
1	-0.4556759	1.0000	...	-0.4583063	1.0000	...
2	-0.3024829	0.8922	-12.08	-0.3025341	1.5572	35.78
3	0.0331262	1.0986	18.78	0.0331247	1.7018	8.49
4	0.0004239	1.0802	-1.70	0.0004238	1.6904	-0.67
5	0.0000011	1.0799	-0.03	0.0000011	1.6903	0
6	0.9999999	1.0799	0	0.9999999	1.6903	0

Table 2 - Comparison of the half contact length (a/h_1) between the values reported in the literature and obtained in this study for various. ($h_1/h_2 = 2, \mu_1/\mu_2 = 1, \kappa_1 = \kappa_2 = 2, k_w = \infty$)

$\frac{\mu_1}{P/h_1}$	100	250	500
	$R/h_1 = 10$	$R/h_1 = 10$	$R/h_1 = 10$
Comez (2003)	0.2202	0.1386	0.0978
This study	0.2204	0.1386	0.0978

Table 3 - Comparison of the half contact length (b/h_1) between the values reported in the literature and obtained in this study for various. ($h_1/h_2 = 2, \mu_1/\mu_2 = 1, \kappa_1 = \kappa_2 = 2, k_w = \infty$)

$\frac{\mu_1}{P/h_1}$	100	250	500
	$R/h_1 = 10$	$R/h_1 = 10$	$R/h_1 = 10$
Comez (2003)	1.2534	1.2446	1.2421
This study	1.2691	1.2599	1.2568

The reason for the 0.01 error rate in Table 3 is attributed to the stiffness parameter controlling the shear modulus variations in the graded medium (βh_1) in the FG layer.

Table 4-5 is compared with a previous study by Eyüpoğlu [28], where the stiffness parameter of the FG layer is assumed to be homogeneous for a value of $\beta h_1=0.01$ in our study. As shown in the tables, the results agree.

Table 4 - Comparison of the half contact length (a/h_1) between the values reported in the literature and obtained in this study for various. ($h_1/h_2 = 1, \mu_0/\mu_1 = 1, \kappa_1 = \kappa_2 = 2, k_w = 1$)

$\beta h_1 = 0.01$	$R / h_1 = 10$	$R / h_1 = 50$	$R / h_1 = 100$
Eyüpoğlu [28]	0.0975	0.2210	0.3173
This study	0.0980	0.2219	0.3177

Table 5 - Comparison of the half contact length (b/h_1) between the values reported in the literature and obtained in this study for various. ($h_1/h_2 = 1, \mu_0/\mu_1 = 1, \kappa_1 = \kappa_2 = 2, k_w = 1$)

$\beta h_1 = 0.01$	$R / h_1 = 10$	$R / h_1 = 50$	$R / h_1 = 100$
Eyüpoğlu [28]	1.4454	1.4553	1.4684
This study	1.4450	1.4550	1.4680

Table 6, values of the half contact lengths are provided for various dimensionless values of β and the ratio of the circular rigid block radius to (R/h_1). In Figure 3, the values are presented graphically.

Table 6 and figure 3 illustrates that as the radius of the circular rigid block increases, the contact distances between the two contact surfaces also increase. Due to the FGM layer being located at the lower part of the x-axis, an increase in the stiffness of the FGM layer leads to an increase in the contact distance between the rigid block and the homogeneous layer, as well as between the homogeneous layer and the FGM layer.

Table 6 - The variation of half-contact lengths with respect to values of circular rigid block and βh_1 . ($h_1/h_2 = 1, \mu_1/\mu_0 = 1, \kappa_1 = \kappa_2 = 2, k_w = 1, k_p = 1$)

βh_1	$R/h_1 = 10$		$R/h_1 = 50$		$R/h_1 = 100$	
	a/h_1	b/h_1	a/h_1	b/h_1	a/h_1	b/h_1
-1	0.219854	1.251549	0.500749	1.323122	0.717755	1.413195
0.01	0.220851	1.332804	0.510805	1.397999	0.741781	1.485439
1	0.222252	1.437649	0.525736	1.496970	0.778251	1.584113

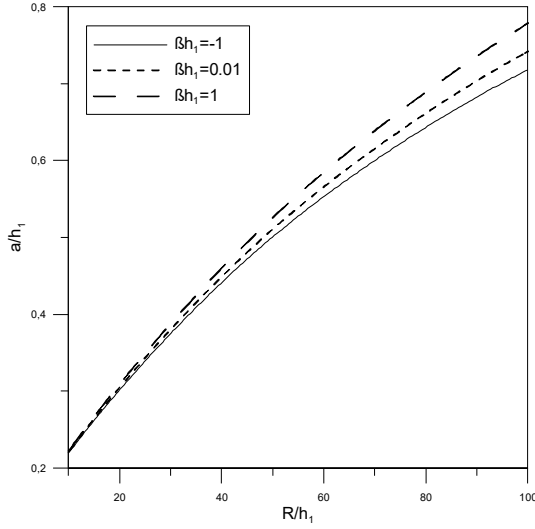


Fig. 3a - The variation of half-contact lengths (a/h_1) with respect to values of circular rigid block and βh_1 . ($h_1/h_2 = 1$, $\mu_1/\mu_0 = 1$, $\kappa_1 = \kappa_2 = 2$, $k_w = 1$, $k_p = 1$)

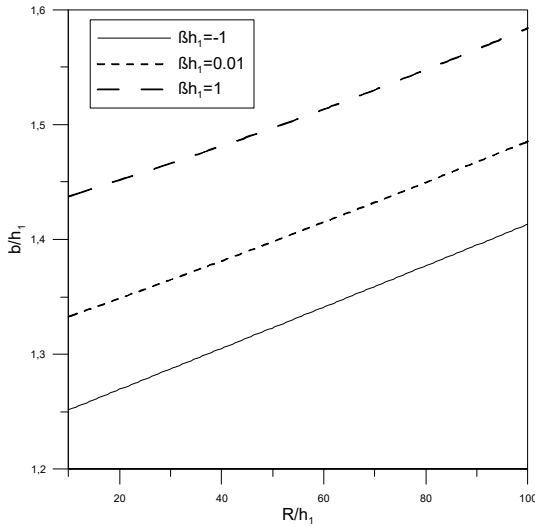


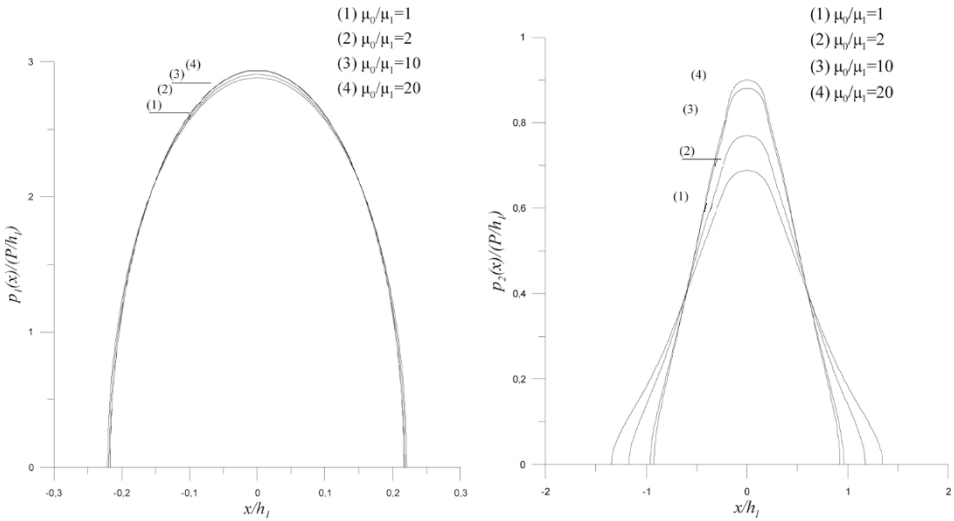
Fig. 3b - The variation of half-contact lengths (b/h_1) with respect to values of circular rigid block and βh_1 . ($h_1/h_2 = 1$, $\mu_1/\mu_0 = 1$, $\kappa_1 = \kappa_2 = 2$, $k_w = 1$, $k_p = 1$)

Table 7 show the variation of half contact lengths for various non-dimensional Pasternak foundation spring constant k_w and shear layer k_p . For very large values of the Pasternak basic modulus (G), k_p is taken to infinity and the contact lengths are shown in Table 7 for both contact surfaces.

Table 7 - The variation of half-contact lengths with respect to dimensionless Pasternak foundation spring constant k_w and shear layer k_p values.
 $(h_1/h_2 = 1, \mu_1/\mu_0 = 1, \kappa_1 = \kappa_2 = 2, \beta h_1 = 0.01)$

k_p	$k_w = 1$		$k_w = 5$		$k_w = 10$	
	a / h_1	b / h_1	a / h_1	b / h_1	a / h_1	b / h_1
10	0.219914	1.209245	0.219833	1.196974	0.219794	1.191304
100	0.219693	1.179251	0.219689	1.178665	0.219687	1.178266
∞	0.219661	1.174866	0.219661	1.174865	0.219661	1.174868

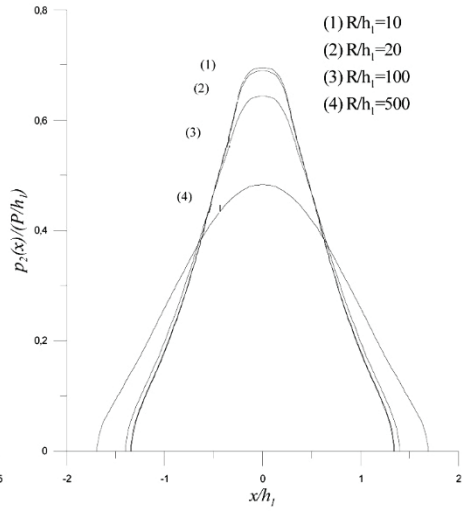
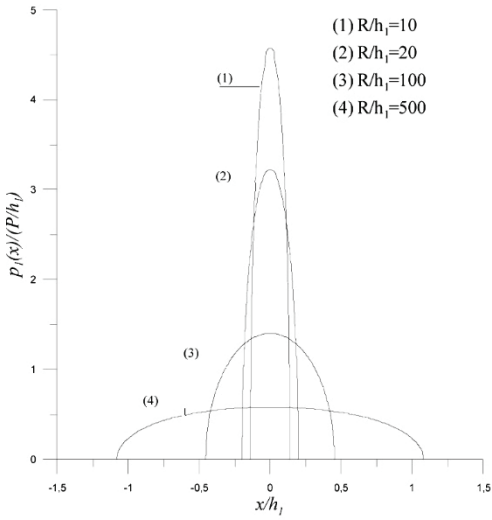
Figure 4a illustrates the distribution of contact stress along the contact distance between the circular rigid block and the homogeneous layer for different dimensionless μ_0/μ_1 values. In Figure 4b, similar stress distributions are presented along the contact distance between the homogeneous layer and the FG layer. Figure 5 illustrates the distribution of contact stresses along the contact distance between the circular rigid block and the homogeneous layer, as well as between the homogeneous layer and the FG layer. These distributions are observed with respect to the increasing radius of various circular blocks (R/h_1).



$(h_1/h_2 = 2, \beta h_1 = 0.01, \kappa_1 = \kappa_2 = 2, k_w = 1, k_p = 1)$

Fig. 4a - Contact stress distribution between circular rigid block and homogeneous layer for various values of μ_1/μ_0

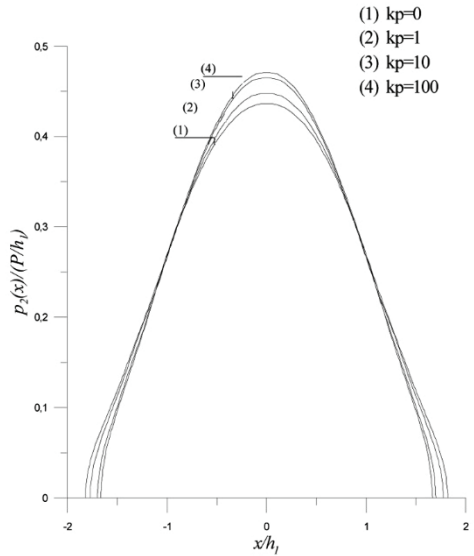
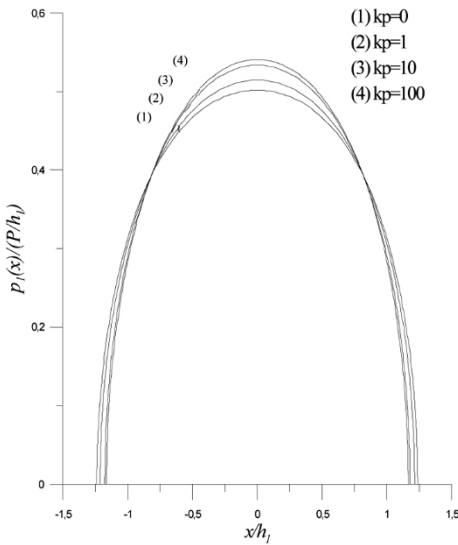
Fig. 4b - Contact stress distribution between homogeneous layer and FGM layer for various values of μ_1/μ_0



$$(h_1/h_2 = 2, \beta h_1 = 0.01, \kappa_1 = \kappa_2 = 2, k_w = 1, k_p = 1)$$

Fig. 5a - Contact stress distribution between circular rigid block and homogeneous layer for various values of R/h_1

Fig. 5b - Contact stress distribution between homogeneous layer and FGM layer for various values of R/h_1



$$(h_1/h_2 = 2, \mu_1/\mu_0 = 1, \kappa_1 = \kappa_2 = 2, \beta h_1 = 0.01, k_w = 1)$$

Fig. 6a - Contact stress distribution between circular rigid block and homogeneous layer for various values of k_p

Fig. 6b - Contact stress distribution between homogeneous layer and FGM layer for various values of k_p

Figure 6 illustrates the distribution of contact stresses along the contact distance between the rigid block and the homogeneous layer, as well as between the homogeneous layer and the functionally graded layer. These distributions are presented for varying values of the Pasternak foundation parameter k_p within a specified range from zero to infinity.

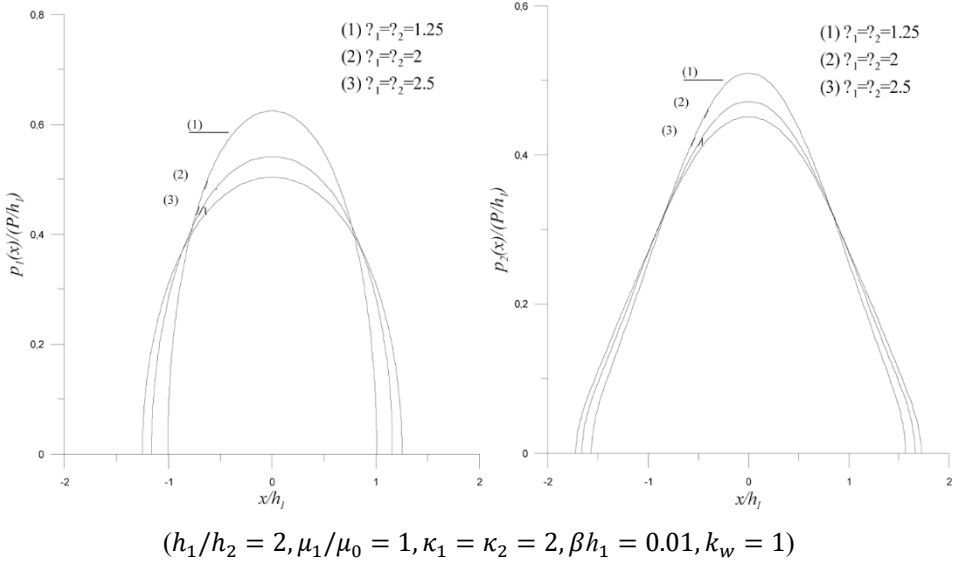


Fig. 7a - Contact stress distribution between circular rigid block and homogeneous layer for various values of κ_1 and κ_2

Fig. 7b - Contact stress distribution between homogeneous layer and FGM layer for various values of κ_1 and κ_2

Figure 7 presents the distribution of contact stresses along the contact distance between the rigid block and the homogeneous layer as well as the homogeneous layer and the functionally graded layer. The variations in these distributions are observed for different values of material properties.

The results of the study can be summarized as follows:

- As the ratio μ_0/μ_1 increases, minimal variations are observed in contact stresses along the contact distance between the circular rigid block and the homogeneous layer, consistent with expectations. However, between the homogeneous layer and the FGM, there is a reduction in the contact distance and a corresponding increase in contact stresses.
- With an increase in the radius of the circular rigid block, the contact distance between the block and the homogeneous layer, as well as between the homogeneous layer and the FGM, grows, leading to a decrease in contact stresses.
- As the value of Pasternak foundation moduli (k_p) increases, contact stresses increase and contact distances decrease. When compared with the study demonstrated in [23],

the results indicate that the Pasternak foundation behaves more rigidly. Consequently, contact distances decrease, leading to an increase in contact stresses.

- As the material properties (κ_1, κ_2) of the homogeneous and FD layer increase, the contact distance increase and the contact stresses decrease.
- In this study, unlike previous studies in the literature, the FG layer was brought into contact with the foundation and the results are presented in detail.
- The influence of the Pasternak foundation on contact problems has been demonstrated.

Symbols

a	: Circular rigid block half contact length
b	: Half contact length between layers.
P	: Singular load
$F(x)$: A function defining the profile of a circular rigid block.
$p_1(x)$: Contact stress beneath the circular rigid block.
$p_2(x)$: Interlayer contact stress.
β	: Rigidity parameter.
μ_0	: Shear modulus on the bottom surface of the FG layer
μ_1	: Shear modulus of homogeneous layer
$\mu_2(y)$: Shear modulus of FG layer
κ_1, κ_2	: Material constant of homogeneous and FG layer
u, v, w	: Displacement components in x, y and z directions
$\sigma_x, \sigma_y, \sigma_z$: Normal stress components in x, y and z directions
$\tau_{xy}, \tau_{xz}, \tau_{yz}$: Shear stress components
h_1	: FD layer height
h_2	: Homogeneous layer height
h	: Total height of the layers
R	: Radius of the circular rigid block
k_w	: Non-dimensionless Winkler foundation moduli
k_p	: Non-dimensionless Pasternak foundation moduli

Note: Some symbols not given in this list are defined in the text where they are used.

References

- [1] Dhaliwal, R.S., Punch Problem for an Elastic Layer Overlying an Elastic Foundation. *International Journal of Engineering Science*, 8, 273–288, 1970.
- [2] Keer, L.M., Chantaramungkorn K., Loss of contact Between an Elastic Layer and Half-Space. *ASME Journal of Applied Mechanics*, 39, 1115–1120, 1972.
- [3] Erdogan, F., Gupta, G.D., On the numerical solutions of singular integral equations. *Quarterly Journal of Applied Mathematics*, 29, 525–534, 1972.
- [4] Ratwani, M., Erdoğan, F., On the Plane Contact Problem for a Frictionless Elastic Layer. *International Journal of Solids and Structures*, 9,921-936, 1973.
- [5] Cakıroğlu, A.O., Elastik Yarım Düzleme Oturan Plakalarda Temas Problemi. PhD Dissertation, K.T.Ü., 1979.
- [6] Aksoğan, O., Akaycı, S.S., Becker, A.A., A Comparative Study of the Contact Problem of for an Elastic Layer Supported by two Elastic Quarter Planes *J. Fac. Engreg. Architecture Cukurova Univ*, 11,25-35, 1996.
- [7] Birinci, A., Erdöl, R., Continuous and Discontinuous Contact Problem for a Layered Resting on Simple Supports. *Structural Engineering and Mechanics*, 12,1,17-34, 2001.
- [8] Birinci, A., Erdöl, R., A Frictionless Contact Problem for Two Elastic Layers Supported by a Winkler Foundation. *Structural Engineering and Mechanics*, 15,331-344, 2003.
- [9] Comez, I., Rijit bir Panç ile Bastırılmış ve Tabanda Tam Olarak Bağlı Ağırlicısız çift Şerit Problemi. PhD Dissertation, K.T.Ü., 2003.
- [10] Comez, I., Birinci, A., Erdöl, R., Double receding contact problem for a rigid stamp and two elastic layers. *European Journal of Mechanics-A/Solids*, 23,2,301-309, 2004.
- [11] El-Borgi, S., Abdelmoula, R., Keer, L., A receding contact plane problem between a functionally graded layer and a homogeneous substrate. *Int. J. Solid Struct.* 43 (3–4), 658–674, 2006.
- [12] Kahya, V., Özşahin, T., Birinci, A., Erdöl, R., A Receding Contact Problem for an Anisotropic Elastic Medium Consisting of a Layer and a Half Plane. *International Journal of Solids and Structures*, 44,5695-5710, 2007.
- [13] Yaylacı, M., Birinci, A., İki Elastik Çeyrek Düzleme Oturan Elastik iki Tabakanın Temas Problemi. XVII. National Mechanics Congress Fırat University, Elazığ, 2011.
- [14] Chen, P.J., Chen, S.H M., Contact behaviors of a rigid punch and a homogeneous half space coated with a graded layer. *Acta Mech*, 223 (3), 563–577, 2012.
- [15] Yan, J., Li, X., Double receding contact plane problem between a functionally graded layer and an elastic layer. *Eur. J. Mech. Solid*, 53, 143–150, 2015.
- [16] Comez, I., Contact Problem for a Functionally Graded Layer Intended by a Moving Punch. *International Journal of Mechanical Sciences*, 100, 339-344, 2015.

- [17] Polat, A., Kaya, Y., Özşahin, T.Ş., Fonksiyonel Derecelendirilmiş Tabakada Sürekli Temas Probleminin Sonlu Elemanlar Yöntemi ile Analizi. XX. National Mechanics Congress Uludağ, Bursa, 2017.
- [18] Valiliev, A.S., Volkov, S.S., Aizikovich, S.M., Mitrin, B.I., Plane contact problem on indentation of a flat punch into a transversely isotropic half-plane with functionally graded transversely-isotropic coating. *Z. Angew. Math. Phys.*, 68 (1), 4, 2017.
- [19] Oner, E., Birinci, A., Investigation of the solution for discontinuous contact problem between a functionally graded (FG) layer and homogeneous half-space. *Archive of Applied Mechanics* 90, 2799-2819, 2020.
- [20] Arslan, O., Hertz-type frictional contact problem of a bidirectionally graded halfplane indented by a sliding rounded punch. *Mech. Mater.* 149, 1–11, 2020.
- [21] Zelentsov, V.B., Lapina, P.A., Mitrin, B.I., Eremeyev, V.A., Characterization of the functionally graded shear modulus of a half-space. *Mathematics* 8 (4), 640, 2020.
- [22] Balcı, N.M., The effect of punch speed on frictional contact mechanics of finite-thickness graded layer resting on the rigid foundation. *Journal of the Brazilian Society of Mechanical Sciences and Engineering*, 42(6),343, 2020.
- [23] Birinci, A., Eyüpoğlu, A., A double receding contact problem of a functionally graded layer and a homogeneous elastic layer resting on a Winkler foundation. *Sigma Journal of Engineering and Natural Sciences*, 38(2),667-686, 2021.
- [24] Bakioğlu, M., Yanık A., Aldemir, Ü., Contact Analysis of Elastic Layer Supported by a Wedge. *European Journal of Science and Technology*, 40,1-6, 2022.
- [25] Yaylacı, M., Abanoz, M., Yaylacı, E., Olmez H., Sekban, D.M., Birinci, A., Evaluation of the contact problem of functionally graded layer resting on rigid foundation pressed via rigid punch by analytical and numerical (FEM and MLP) methods. *Archive of Applied Mechanics*, 92,1953-1971, 2022.
- [26] Adıyaman, G., Oner, E., Yaylacı, M., Birinci, A., A study on the Contact Problem of a Layer Consisting of Functionally Graded Material (FGM) in the Presence of Body Force. *Journal of Mechanics of Materials and Structures*, 1,18, 125-141, 2023.
- [27] Adıyaman, G., Tabakalı Ortamlarada Temas Problemlerinin Genel Çözümü ve bu Çözüme İlişkin bir Bilgisayar Programının Geliştirilmesi. PhD Dissertation, K.T.Ü., 2019.
- [28] Eyüpoğlu, A., Winkler Temele Oturan ve Rijit Dairesel Blok Aracılığıyla Yüklenen biri Fonksiyonel Derecelendirilmiş iki Tabakanın Temas Problemi. Master Thesis, K.T.Ü., 2019.

Flexural Experiments on B58 Type Railway Sleepers with Different Dosages of Steel Fibers

Ercan KASAPÖĐLU¹
Tefaruk HAKTANIR^{2*}



ABSTRACT

The flexural strengths and toughnesses of 15 post-tensioned B58 type railway sleepers produced at the Turkish State Railroads Sivas Plant using C40 class concrete with addition of hooked steel fibers at dosages of 0, 20, 30, 40, 50 kg/m³ were experimentally determined. Four-point flexural experiments were applied to them in one month after their production and proper curing. Three cylindrical samples of 15×30 cm dimensions taken from the first and the fourth batches apiece were subjected to standard compression tests with compressometer rings mounted on each sample after having been cured in 21 °C water tank for 28 days, resulting in their compressive strength and modulus of elasticity. Modeling a railway sleeper as a post-tensioned reinforced-concrete beam, the maximum load it can resist in the experimented configuration was calculated by the ultimate-strength method using its dimensions and material properties. The experimentally-measured maximum load carried by the reference sleeper without any steel fibers was found to be 1.34 times the theoretically-calculated value, and the same ratio was found to be 1.59 for the sleepers having steel fibers of 40 kg/m³ dosage, accounting for an increase of 18%. And, the experimentally-measured toughness of the sleepers with 40 kg/m³ dosage steel fibers was found to be 23% greater than that of the reference sleepers.

Keywords: Concrete railway sleepers, steel fibers, flexural strength, toughness.

1. INTRODUCTION

Addition of steel fibers to structural concrete with dosages of about 30 ~ 50 kg/m³ improves its crack behavior and its tensile strength by making it less brittle at the expense of a small increase in its cost. There are standards, regulations and technical publications about steel-fiber-added concrete [e.g. 1, 2, 3]. Experimental studies were done at the Civil Engineering

Note:

- This paper was received on November 24, 2023 and accepted for publication by the Editorial Board on April 5, 2024.
 - Discussions on this paper will be accepted by November 30, 2024.
- <https://doi.org/10.18400/tjce.1394166>

1 Directorate General of Turkish State Railroads, Ankara, Türkiye
kasapogluercan@gmail.com - <https://orcid.org/0009-0004-3383-6530>

2 Erciyes University, Department of Civil Engineering, Kayseri, Türkiye
thaktan@erciyes.edu.tr - <https://orcid.org/0000-0002-8111-4557>

* Corresponding author

Department of Erciyes University in 2000s about the effect of steel fibers on the flexural strength of reinforced-concrete (RC) beams, RC box beams [4, 5], and on the bearing strength of concrete sewer pipes [6]. Tangible improvements were observed in these elements using standard hooked steel fibers [7] having a tensile strength of 1050 N/mm^2 , each having a length of 60 mm and a diameter of 0.75 mm. Having been influenced by these positive results, the same type of steel fibers were also tried in RC railway sleepers. They were produced as post-tensioned precast RC beams of 240 cm lengths by Sivas Plant of Directorate General of Turkish State Railroads (known by the acronym TCDD), as part of a M.Sc. thesis study [8]. Later, a few more experimental studies were done by other researchers about the effect of steel fibers on various mechanical properties of prestressed RC sleepers [e.g. 9, 10, 11, 12, 13, 14].

The report by Weisheit and Metzler [9] presents the results of a comprehensive experimental study which performed (1) compressive tests on 15 cm cubic samples, (2) four-point flexural tests on RC sleepers produced with a hybrid combination of fibers of steel, of plastic, and of glass as an admixture to high-strength concrete of C70 class, and (3) dynamic fatigue tests on these sleepers. Significant improvements in cracking behavior and in flexural and fatigue strengths were observed; however, no information about the cost of such modified sleepers was given [9].

Sadeghi et al [10] did detailed static and dynamic tests on prestressed RC sleepers with various amounts of a mixture of short and long steel fibers and different numbers of prestressing steel wires whose results indicated that the use of hybrid steel fibers in the sleepers led to tangible increases in their load-carrying capacity and flexural toughness while having almost the same natural dynamic frequency and damping ratios as the conventional ones. Sadeghi et al [10] concluded that such modified sleepers were more effective and cost efficient for high-speed tracks when compared with the conventional ones.

Parvez and Foster [11] did flexural and fatigue experiments on eight prestressed RC sleepers with steel fibers of dosages of 20 kg/m^3 and 40 kg/m^3 and concluded that the cracking behavior, the flexural and fatigue strengths of steel-fiber added sleepers improved; and, they recommended the dosage of 40 kg/m^3 as its performance was better than that of 20 kg/m^3 .

Bae and Pyo [12] carried out flexural tests on post-tensioned RC sleepers produced by ultra-high performance concrete with steel fibers added at dosages of 0.5%, 1%, 1.5% by volume and recommended dosages of 1% and 1.5% for better flexural strength.

Wang et al [13] produced prestressed RC sleepers with four different combinations of steel fibers, which had volumetric dosages of 0.5% straight plus 1.5% hooked, 1.0% straight plus 1.0% hooked, 1.5% straight plus 1.0% hooked, the diameters and the lengths of straight and hooked fibers being 0.2, 13; 0.3, 22 mm. The tensile strength of these fibers were 2850 N/mm^2 . The dimensions of these fibers are much smaller than 0.75 mm and 60 mm and the strength is much higher than 1050 N/mm^2 which are those of the hooked steel fibers used in our study [8]. Compressive and split tensile tests on 15 cm cubic samples and three-point flexural experiments yielded improved compressive, tensile and flexural strengths in all combinations; yet, 1.0% straight plus 1.0% hooked combination slightly outperformed the others, which revealed increases of 45% and 55% in compressive and flexural strengths as compared to the reference concrete mixes used in sleeper production [13].

In years 2021 and 2022, Çeçen and Aktaş published a few papers summarizing comprehensive experimental and theoretical studies on innovative concrete railway sleepers of the same dimensions as B70 type. Their developmental sleepers contained carbon-fiber-reinforced polyurethane laminates embedded in them instead of the post-tensioned steel bars. And, they asserted that these sleepers with no steel reinforcement bars had improved peculiarities over prestressed RC B70 type sleepers produced at Sivas Plant of TCDD. Those studies resulted in a novel patented non-prestressed product with a higher flexural strength, a highly improved fatigue behavior, much smaller probability of resonance with moving rail cars, smaller size crack formations, and much better damping ratios even after 50 cycles of 330 kN impact loadings than those of standard prestressed B70 type sleepers [15, 16, 17, 18, 19, 20, 21]. The post-tensioned steel tendons used in the conventional B70 sleepers are imported while the carbon-fiber-reinforced polyurethane (CFRP) laminates are produced in Türkiye. The cost of these new sleepers comprising CFRP laminates is just a little higher than that of the B70 types, but, the benefits such as no steel reinforcement and hence no post-tensioning, shorter manufacturing time, better fatigue strength, and longer service life will outweigh the B70 type sleepers. Although this newly put forth L-CFRP sleeper was shown to outperform the commonly used B70 type in many relevant peculiarities, it is yet to be verified in actual field applications.

Ahmed et al [14] applied static bending tests on B70 type of prestressed RC sleepers produced with C50 class of concrete in which steel fibers at volumetric dosages of 0%, 0.5%, 1%, and 1.5% were added, and they found that the first cracking load, failure load, failure mode, crack sizes, and load-deflection curve peculiarities of the steel-fiber added sleepers improved significantly.

Çankaya and Akan experimentally determined that addition of steel fibers to their concrete mixtures by a dosage of 1% in absolute volume increased the flexural strength of reinforced concrete beams by about 10% [22].

Türker et al, as a result of four-point flexural experiments on beams of 150×250×2500 mm dimensions, experimentally determined that addition of commonly used hooked steel fibers to ultra-high-performance concrete mixtures improved the flexural strength of reinforced-concrete beams by about 15% with appreciably improved crack formations [23].

The objective of this note is to summarize the findings of the flexural experiments done on a total of 15 post-tensioned B58 type of RC sleepers produced with addition of 0, 20, 30, 40, 50 kg/m³ hooked steel fibers of diameters and lengths of 0.75 mm and 60 mm having a minimum tensile strength of 1050 N/mm² in their concrete batches [8] and to compare their results with those of similar studies. A total of 15 sleepers, three of which having the same steel fibers dosage, were tested and the average values were reported. According to the 2022 Annual Report by the General Directorate of Turkish State Railways, the total lengths of the conventional and the high speed railways under operation are 11688 km and 1460 km, respectively [24]. Up until ten years ago, mostly B58 type of sleepers were laid under the conventional railways. But, in recent years some of them have been replaced by higher-strength sleepers. Still, the experimental results obtained with B58 type of sleepers should be attributable to the B70 types because B70 are also prestressed RC units.

2. MATERIAL AND METHOD

2.1. Materials

The cement used in producing B58 type sleepers at TCDD’s Sivas Plant is CEM I 42.5 R by EN 197-1. The 7-day and 28-day compressive strengths by the standard Rilem tests of EN 196 are about 40 and 50 N/mm². The mix recipe of the concrete used for B58 sleepers is given in Table 1.

Table 1 - Mix recipe of the C40 class of concrete used in B58 sleepers by Sivas Plant.

Ingredient	Content (kg)
CEM I 42.5 R	450
Tap water	135
River sand (Dmax=8 mm) (SSD)*	940
Fine crushed aggregate (Dmax=16 mm) (SSD)*	400
Coarse crushed aggregate (Dmax=32 mm) (SSD)*	500

*: SSD means “saturated surface-dry”

Two steel bars, each having a diameter of 9.4 mm, are used for post-tensioning. There are four circular tunnels throughout each sleeper of sufficient diameter so as to allow free passage of the post-tensioning bars. Both tips of each bar are grooved to be bolted after post-tensioning, and it is passed through two of the tunnels in diagonal position. A cross-shaped canal exists at one end of the sleeper, and a total of 320 kN tension force is uniformly applied to all four tip points of these two bars, and finally such stretched bars are firmly fixed in by an appropriate nuts-and-lock mechanism.

The average values of yield and ultimate strengths of three randomly taken samples of the post-tensioning steel bars used in the sleepers turned out to be 1264 N/mm² and 1619 N/mm² after having been subjected to standard tests in a certified Universal Testing Machine [8].

Five different batches of the mixture given in Table 1 were produced with dosages of 0, 20, 30, 40, 50 kg/m³ of steel fibers. Three cylindrical samples of 15×30 cm dimensions were taken from the reference batch with no fibers and from the one with 40 kg/m³ fibers and they were subjected to standard compression tests in a certified Compression Machine with a compressometer ring attached to each sample after having stayed for 28 days in curing tank. For each sample, the modulus of elasticity was computed as the slope of the line on the stress-strain curve passing through the points of 5% and 45% of the ultimate strength [8]. The average 28-day strength and modulus of elasticity for each sample of the two batches are given in Table 2.

The sleepers are treated in steam curing at 60 °C for about 10 hours in vapor room where they stay for 24 hours. A few days later, 15 sleepers manufactured with different dosages of steel fibers were transported from Sivas to the Structural Mechanics Laboratory of Erciyes University in Kayseri.

Table 2 - Average 28-day strength and elasticity modulus of concrete batches.

Batch	Compressive strength (N/mm ²)	Elasticity modulus (N/mm ²)
Mixture in Table 1 with no steel fibers	48.8	32,000
Mixture in Table 1 with 40 kg/m ³ steel fibers	57.1	29,000

2.2. Experiments

Because the objective of this experimental study was to observe the effects of addition of the hooked steel fibers of 80/60 dimensions having an ultimate strength of 1050 N/mm² in the mixture of C40 class of concrete used in production of B58 type of railway sleepers on their flexural strength and flexural toughness, each sleeper was treated as a simply-supported beam and hence was tested in a certified beam-testing setup by two-point loading as shown in Figure 1. In TS EN 13230-2 a similar configuration of flexural loading is specified [25] where the span length between the supports is 150 cm, which is the same as that in our tests. In TS EN 13230-2 a three-point flexural test is specified where the single load in mid-span of the sleeper is exerted by a resilient pad of 10×30 cm dimensions. Our loading rate was 10 tons/minute which was very close to 120 kN/minute given in TS EN 13230-2. Figure 2 shows the instant of placing a sleeper in the loading machine, and Figure 3 shows the beginning of the flexural experiment. The mid-span deflections were read from a strain gauge of 0.01 mm precision having a maximum range of 50 mm at every 0.5 tons of loading.

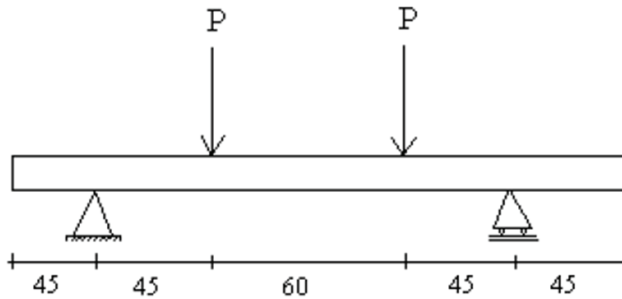


Figure 1 - Two-point loading configuration of a sleeper (dimensions are in cm).

These sleepers get slightly slender in height towards the mid-span, and the middle 30 cm part is approximately rectangular with a width of 185 mm and a height of 175 mm. The applied post-tensioning imposed a uniformly distributed compressive stress on the concrete part of each sleeper. The peculiarities and relevant quantities of the concrete and the reinforcing bars used in these sleepers were put in the appropriate steps of the analytical computations done in accordance with the ultimate-strength theory of prestressed RC section as articulated in Turkish Standard TS 3233 [26]. For example, the strain of the concrete (C40) at the outermost edge of the resisting cross-section was taken as 0.003, and the ultimate compressive strength of concrete was assumed to equal 85% of its characteristic strength. The details of these

computations are given in [8]. The result of the theoretical analyses indicated an ultimate load of $2P = 85 \text{ kN}$ for the loading configuration applied during the flexural experiments [8].



Figure 2 - A sleeper being carried to its position in the beam-loading machine (The other sleepers in stack waiting for their turns to be tested).



Figure 3 - A sleeper placed in the beam-loading machine in a two-point-loading position at the onset of the experiment.

3. RESULTS

The plots of 2P loads in metric tons against the mid-span deflections were drawn for each of the tested sleepers [8]. Here, Figure 4 shows the averaged such plots for all five combinations of sleepers. Table 3 presents: (1) the theoretical ultimate load computed by the ultimate-strength method treating a sleeper as a post-tensioned reinforced-concrete beam subjected to the two-point loading configuration in Figure 1, (2) the averaged observed loads to the first crack, (3) the averaged observed maximum resisted loads, and (4) the averaged flexural toughnesses. Flexural toughness of a reinforced concrete beam is a measure of its energy absorption capacity and is directly related to its ductility which characterizes its crack resistance. Experimentally, the flexural toughness is determined as the area under the load – midspan deflection curve. This area was computed numerically by the “trapezoidal integration”.

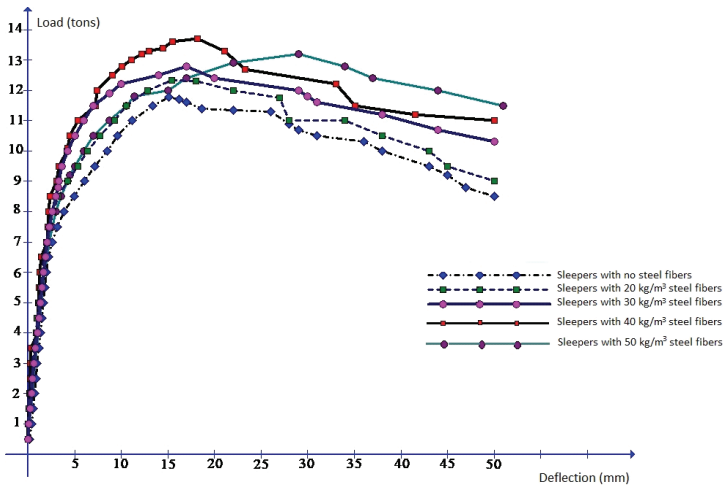


Figure 4 - The averaged plots of 2P loads against the mid-span deflections for all five combinations of sleepers.

Table 3 - Averages of the observed loads to the first crack, the maximum resisted loads, and the areas under the load-deflection curves of the experimented sleepers.

Sleeper Type	Theoretical ultimate load (kN)	Load to first crack (kN)	Experimental ultimate load (kN)	Flexural toughness (kN-mm)
Slprs with no SF*	85	80	114	4700
Slprs with 20 kg/m ³ SF	85	93	122	5200
Slprs with 30 kg/m ³ SF	85	94	123	5300
Slprs with 40 kg/m ³ SF	85	97	135	5800
Slprs with 50 kg/m ³ SF	85	95	131	5900

*: SF means “steel fibers”

We have contacted the responsible personnel both at the company producing the steel fibers and Sivas Plant of TCDD and we have obtained the information that recently the unit cost of the steel fibers is 1.5 Euro/kg and the cost of one standard sleeper is 55 Euro. Considering the fact that the concrete volume of a B58 sleeper is about 105 dm³, 4.2 kg of steel fibers are used in a sleeper with a fiber dosage of 40 kg/m³, bringing about an additional cost of 6.3 Euro per sleeper.

4. CONCLUSION AND DISCUSSION

Addition of steel fibers of 80/60 type which have an ultimate strength of 1050 N/mm² to the batch of C40 class of concrete used in production of B58 type RC railway sleepers with a dosage of 40 kg/m³ (0.5% by volume) increased their flexural strength 18% and flexural toughness 23%. These positive increases in mechanical peculiarities will be realized at an additional cost of a 12% increase in the production of these sleepers.

Having done a detailed experimental study on the effects of various parameters of steel-fiber added concrete such as water/cement ratio, binder content, and fiber dosage on its electrical resistivity, Cleven et al [27] determined that the global electric resistivity of concrete with a steel fiber dosage of 40 kg/m³ was about 30 Ωm while that of the reference concrete was around 60 Ωm in 185 days after pouring of concrete. Therefore, it is advisable to do in-situ tests to check whether any interference by such steel-fiber added sleepers laid down under railways will take place on signalization activities.

References

- [1] TSE (1992b) TS 10514 Concrete - Steel Fiber Reinforced - Rules for Mixing Concrete and Control. Turkish Standards Institute, Yüce-tepe, Ankara, Turkey.
- [2] ACI (2002) State-of-the-Art Report on Fiber Reinforced Concrete, ACI-544.R-96 (Reapproved 2002), ACI Committee 544, American Concrete Institute,
- [3] Yazıcı Ş, İnan G, Tabak V (2007) Effect of aspect ratio and volume fraction of steel fiber on the mechanical properties of SFRC. *Construction and Building Materials*, 21(6), 1250–1253. <https://doi.org/10.1016/j.conbuildmat.2006.05.025>
- [4] Altun F and Haktanır T (2004) A comparative experimental investigation of steel fiber added reinforced concrete beams. *Materials de Construcción*, 54(276), 5–15.
- [5] Altun F, Haktanır T, Arı K (2006) Experimental investigation of steel fiber reinforced concrete box beams under bending. *Materials and Structures*, 39(4), 491–499.
- [6] Haktanır T, Arı K, Altun F, Karahan O (2007) A comparative experimental investigation of concrete, reinforced-concrete, and steel-fiber added concrete pipes under three-edge-bearing test. *Construction and Building Materials*, 21(8), 1702–1708.
- [7] TSE (1992a) TS 10513 Steel Fibers for Concrete Reinforcement. Turkish Standards Institute, Yüce-tepe, Ankara, Turkey.

- [8] Kasapoğlu E (2010) Effect of Steel-Fiber Usage on Mechanical Properties of Concrete Railway Sleepers. M.Sc. Thesis, Erciyes University, Graduate School of Natural and Applied Sciences. <https://tez.yok.gov.tr/UlusalTezMerkezi/tezDetay.jsp?id=NGI5wS2idXLccoJNs3Qsnw&no=8HjWjwejK0AfIwmcs1QZPg>
- [9] Weisheit S and Metzler G (2014) Entwicklung einer rissfreien Bahnschwelle durch den Einsatz eines kombifaserbewehrten Hochfesten Betons - KOMBIFASERBETON -. Universität Innsbruck Fakultät für Technische Wissenschaften Institut für Konstruktion und Materialwissenschaften Arbeitsbereich Materialtechnologie, Wien, Österreich.
- [10] Sadeghi J, Kian A R T, Khabbazi A S (2016) Improvement of Mechanical Properties of Railway Track Concrete Sleepers Using Steel Fibers. *Journal of Materials Engineering, ASCE*, 28(11), [https://doi.org/10.1061/\(ASCE\)MT.1943-5533.0001646](https://doi.org/10.1061/(ASCE)MT.1943-5533.0001646)
- [11] Parvez A and Foster S J (2017) Fatigue of steel-fibre-reinforced concrete prestressed railway sleepers. *Engineering Structures*, 141, <https://doi.org/10.1016/j.engstruct.2017.03.025>
- [12] Bae Y and Pyo S (2020) Effect of steel fiber content on structural and electrical properties of ultrahigh performance concrete (UHPC) sleepers. *Engineering Structures*, 222, <https://doi.org/10.1016/j.engstruct.2020.111131>
- [13] Wang J, Siahkouhi M, Astaraki F, Uganbayar S, Jing G, Rad M M (2022) Modification of Concrete Railway Sleeper Mix Design, Using a Hybrid Application of Steel Fibers. *Acta Polytechnica Hungarica*, 19(3), 119–130.
- [14] Ahmed S, Atef H, Husain M (2023) Experimental and parametrical investigation of pre-stressed ultrahigh-performance fiber-reinforced concrete railway sleepers. *Frontiers of Structural and Civil Engineering*, 17(3): 411-428. DOI: 10.1007/s11709-023-0928-3
- [15] Çeçen F and Aktaş B (2021a) Modal and harmonic response analysis of new cfrp laminate reinforced concrete railway sleepers. *Engineering Failure Analysis*, 127, no 105471, <https://doi.org/10.1016/j.engfailanal.2021.105471>
- [16] Çeçen F and Aktaş B (2021b) Incremental LUR tests of new LCR concrete railway sleepers. *Engineering Failure Analysis*, 130, no 105793, <https://doi.org/10.1016/j.engfailanal.2021.105793>
- [17] Aktaş B, Çeçen F, Öztürk H, Navdar M B, Öztürk İ Ş (2022) Comparison of prestressed concrete railway sleepers and new LCR concrete sleepers with experimental modal analysis. *Engineering Failure Analysis*, 131, no 105821, <https://doi.org/10.1016/j.engfailanal.2021.105821>
- [18] Çeçen F, Aktaş B, Öztürk H, Navdar M B, Öztürk İ Ş (2022a) Behaviour of new LCR and ordinary prestressed concrete railway sleepers under repeated impact loads. *Construction and Building Materials*, 319, no. 126151, <https://doi.org/10.1016/j.conbuildmat.2021.126151>

- [19] Çeçen F, Aktaş B, Öztürk H, Öztürk İ Ş, Navdar M B (2022b) Comparison of new LCR and ordinary prestressed concrete railway sleepers with LUR tests. *Construction and Building Materials*, 321, no. 126414, <https://doi.org/10.1016/j.conbuildmat.2022.126414>
- [20] Çeçen F, Aktaş B, Öztürk H, Öztürk İ Ş, Navdar M B (2022c) Comparative modal analysis of B70 and LCR-6 type railway sleepers after repeated impact loads. *Construction and Building Materials*, 336, no. 127563, <https://doi.org/10.1016/j.conbuildmat.2022.127563>
- [21] Çeçen F, Aktaş B, Öztürk H, Öztürk İ Ş, Navdar M B (2022d) Comparative Investigation of Carbon-Fiber Laminate Reinforced Sleepers with B70-Type Prestressed Concrete Sleepers (In Turkish). *Railway Engineering*, 15, 97–110, doi: 10.47072/demiryolu.1028740
- [22] Çankaya M A and Akan Ç (2023) An Experimental and Numerical Investigation on the Bending Behavior of Fiber Reinforced Concrete Beams. *Turkish Journal of Civil Engineering*, Paper 717, 34(1), 59–78. <https://doi.org/10.18400/tjce.1209152>
- [23] Türker K, Birol T, Yavaş A, Hasgül U, Yazıcı H (2019) Flexural Behavior of Beams with Ultra High Performance Fiber Reinforced Concrete (In Turkish). *Teknik Dergi*, Paper 523, 30(1), 8777–8801,
- [24] TCDD (2023) 2022 Annual Report (Bilingual in Turkish and in English). General Directorate of Turkish State Railways, Directorate of Strategic Planning. Ankara, Türkiye.
- [25] TSE (2016) TS EN 13230-2 Railway applications; Track - Concrete sleepers and bearers – Part 2: Prestressed monoblock sleepers. Turkish Standards Institute, Yüce-tepe, Ankara, Türkiye.
- [26] TSE (1979) TS 3233 Building Code Requirements for Prestressed Concrete. Turkish Standards Institute, Yüce-tepe, Ankara, Turkey.
- [27] Cleven S, Roupach M, Matschei T (2021) Electrical Resistivity of Steel Fibre-Reinforced Concrete—Influencing Parameters. *Materials*, 14, 3408, <https://doi.org/10.3390/ma14123408>

Turkish Journal of Civil Engineering (formerly Teknik Dergi)

Manuscript Drafting Rules

1. The whole manuscript (text, charts, equations, drawings etc.) should be arranged in Word and submitted in ready to print format. The article should be typed on A4 (210 x 297 mm) size paper using 10 pt (main title 15 pt) Times New Roman font, single spacing. Margins should be 40 mm on the left and right sides and 52.5 mm at the top and bottom of the page.
2. Including drawings and tables, articles should not exceed 25 pages, technical notes 10 pages.
3. Your contributed manuscript must be sent over the DergiPark system. (<http://dergipark.gov.tr/tekderg>)
4. The text must be written in a clear and understandable language, conform to the grammar rules. Third singular person and passive tense must be used, and no inverted sentences should be contained.
5. Title must be short (10 words maximum) and clear, and reflect the content of the paper.
6. Sections should be arranged as: (i) abstract and keywords, (ii) title, abstract and keywords in the other language, (iii) main text, (iv) symbols, (v) acknowledgements (if required) and (vi) references.
7. Both abstracts should briefly describe the object, scope, method and conclusions of the work and should not exceed 100 words. If necessary, abstracts may be re-written without consulting the author. At least three keywords must be given. Titles, abstracts and keywords must be fitted in the first page leaving ten line space at the bottom of the first page and the main text must start in the second page.
8. Section and sub-section titles must be numbered complying with the standard TS1212.
9. Symbols must conform to the international rules; each symbol must be defined where it appears first, additionally, a list of symbols must be given in alphabetic order (first Latin, then Greek alphabets) at the end of the text (before References).
10. Equations must be numbered and these numbers must be shown in brackets at the end of the line.
11. Tables, drawings and photographs must be placed inside the text, each one should have a number and title and titles should be written above the tables and below the drawings and photographs.
12. Only SI units must be used in the manuscripts.
13. Quotes must be given in inverted commas and the source must be indicated with a reference number.
14. Acknowledgement must be short and mention the people/ institutions contributed or assisted the study.
15. References must be numbered (in brackets) in the text referring to the reference list arranged in the order of appearance in the text. References must include the following information:

If the reference is an article: Author's surname, his/her initials, other authors, full title of the article, name of the journal, volume, issue, starting and ending pages, year of publication.

Example : Naghdi, P. M., Kalnins, A., On Vibrations of Elastic Spherical Shells. J. Appl. Mech., 29, 65-72, 1962.

If the reference is a book: Author's surname, his/her initials, other authors, title of the book, volume number, editor if available, place of publication, year of publication.

Example : Kraus. H., Thin Elastic Shells, New York. Wiley, 1967.

If the reference is a conference paper: Author's surname, his/her initials, other authors, title of the paper, title of the conference, location and year.

If the source is a thesis: Author's surname, his/her initials, thesis title, level, university, year.

If the source is a report: Author's surname, his/her initials, other authors, title of the report, type, number, institution it is submitted to, publication place, year.
16. Discussions to an article published in Turkish Journal of Civil Engineering (formerly Teknik Dergi) should not exceed two pages, must briefly express the addressed points, must criticize the content, not the author and must be written in a polite language. Authors' closing remarks must also follow the above rules.
17. A separate note should accompany the manuscript. The note should include, (i) authors' names, business and home addresses and phone numbers, (ii) brief resumes of the authors and (iii) a statement "I declare in honesty that this article is the product of a genuinely original study and that a similar version of the article has not been previously published anywhere else" signed by all authors.
18. Copyright has to be transferred to UCTEA Turkish Chamber of Civil Engineers. The standard copyright form signed by the authorised author should therefore be submitted together with the manuscript.

CONTENTS

RESEARCH ARTICLE

Rainwater Harvesting System Analysis for Semi-Arid Climate: A Daily Linear Programming Model..... 1

Mustafa RUSO, Bertuğ AKINTUĞ, Elcin KENTEL

Spatial Prediction of Groundwater Potential of Upper Tigris Basin Mapping in Türkiye with GIS-Based Multicriteria Decision Making (MCDM) Method 29

Recep ÇELİK

Design and Tests of Structural Post-Tensioned Glass T-Beams..... 51

Emrullah KOCA, Ahmet TÜNER

6 Şubat 2023 Depremleri ve Saha Gözlemlerine Dayalı Bina Hasarları Hakkında Ön Değerlendirme 75

Cem YENİDOĞAN

A Receding Contact Problem of Two Layers one of Functionally Graded, Loaded by Circular Rigid Block and Resting on a Pasternak Foundation..... 115

Aleyna YAZICIOĞLU, Ahmet BİRİNCİ, Gökhan ADIYAMAN

TECHNICAL NOTE

Flexural Experiments on B58 Type Railway Sleepers with Different Dosages of Steel Fibers..... 133

Ercan KASAPÖĞLU, Tefaruk HAKTANIR



UCTEA Turkish Chamber of Civil Engineers

TMMOB İnşaat Mühendisleri Odası

Necatibey St. No: 57, Kızılay, Ankara / Türkiye

Tel: +90.312.294 30 00 - Faks: 294 30 88

www.imo.org.tr